

Studies on deformation of minerals applying computational science
including computer simulation and machine learning analyses
(コンピューターシミュレーションや機械学習分析を含む計算科学を応用した
鉱物の変形に関する研究)

UHMB Tae-hoon

(嚴 泰勳)

A dissertation for the degree of Doctor of Science
Department of Earth and Environmental Sciences,
Graduate School of Environmental Studies, Nagoya University
(名古屋大学大学院環境学研究科地球環境科学専攻学位論文 博士(理学))

2022

Contents

| | |
|--|----|
| Contents | i |
| OVERVIEW | 1 |
| Part 1 | |
| Abstract..... | 4 |
| 1. Introduction | 4 |
| 2. Deformation model..... | 6 |
| 2.1 Equation describing the diffusion process | 7 |
| 2.2 Equation for dislocation creep | 10 |
| 2.3 Whole equation | 10 |
| 2.4 Simple shear..... | 11 |
| 3. Application to K-feldspar inclusions within host quartz grains | 12 |
| 3.1 Geological setting and sample description | 12 |
| 3.2 Deformation conditions | 13 |
| 3.3 K-feldspar inclusions | 15 |
| 3.3.1 Shape analysis of K-feldspar inclusions | 15 |
| 3.3.2 $L-2R$ patterns of K-feldspar inclusions | 16 |
| 4. Results of the deformation model..... | 17 |
| 4.1 Parameters in the mathematical equation for the deformation model | 17 |
| 4.2 $L-2R$ patterns generated by the deformation model..... | 18 |
| 4.3 $L-2R$ patterns: comparison between deformation model results and K-feldspar inclusion data..... | 19 |
| 5. Discussion..... | 21 |
| 5.1 Effect of post-deformation annealing..... | 21 |
| 5.2 Evaluation of deformation duration and post-deformation annealing rate | 22 |
| 5.3 Natural shear strain | 23 |

| | |
|--|----|
| 5.4 Mismatch between modeled results and observed data | 24 |
| 6. Conclusion | 26 |
| Figures | 27 |
| Tables | 40 |
| | |
| Part 2 | |
| Abstract..... | 43 |
| 1. Introduction | 44 |
| 2. Characteristics of Cr-Al chemical zoning in spinel grains | 45 |
| 2.1 Sample description..... | 45 |
| 2.2 Cr-Al chemical zoning | 46 |
| 2.3 Intensity of Cr-Al chemical zoning..... | 47 |
| 2.4 Geometrical properties | 47 |
| 3. Methods of machine learning analysis | 48 |
| 3.1 Machine learning framework..... | 48 |
| 3.2 Pre-processing | 48 |
| 3.3 Mean-shift Clustering | 49 |
| 3.4 Data splitting..... | 50 |
| 3.5 Model assessment | 50 |
| 3.6 Criteria analysis using Decision tree..... | 51 |
| 3.7 Importance assessment using random forest..... | 52 |
| 3.8 Probability map constructed by logistic regression | 53 |
| 4. Result..... | 54 |
| 4.1 Scatterplot for the intensity of Cr-Al chemical zoning | 54 |
| 4.2 Criteria for clustering..... | 54 |
| 4.3 Feature importance..... | 56 |
| 4.4 Probability map..... | 56 |
| 5. Discussion..... | 57 |

| | |
|---|----|
| 5.1 Interpretation for the analyzed data | 57 |
| 5.2 Interpretation for relationships between grain size and the Cr-Al chemical zoning | 59 |
| 5.3 The R_{diff} and deformation temperature | 60 |
| 5.4 Interpretation for relationships between aspect ratio and the Cr-Al chemical zoning | 62 |
| 6. Conclusion | 63 |
| Figures | 65 |
| Tables | 78 |
| Epilogue | 82 |
| Acknowledgement | 83 |
| References | 84 |

OVERVIEW

Deformation of the solid earth has not only complex relationship for interactions between various geological factors including mineral chemistry, physics, material properties, dynamics of plates and so on, but also various temporal scales (from few milliseconds to billions of years) and spatial scales (from atomic to plate). Although understanding the deformation of the solid earth is fascinating and necessary subject in humanity, there are some problems in understanding the deformation due to the complexity and the various temporal and spatial scales. The needs to solve the problems derive various methods of studying the deformation. Computational science is one of the methods. The computational science, which is an area of science computing phenomena and processes of actual world by applying mathematics, observed data, and computer algorithms, have been used as good tools to understand and interpret the deformation of solid earth. The computational science involves computer sciences fields such as computer simulation, artificial intelligence (AI). Over the last few decades, the computational science has made incredible progress in the data processing speed and the data analyzing method with the development of computational hardware and software. The scales and details of the computational sciences drastically improved by the progress suggest great possibility to understand and interpret the deformation of solid earth.

In this PhD thesis, I studied deformations of minerals by using the computational sciences. The studies are divided into two parts, and the computational science was used in different ways for each part. In part I, the computational science is utilized as a computer simulation by computing a numerical model to simulate deformation of mineral for times of geological scales. The simulation makes it possible to calculate the deformation of minerals over millions of years. In part II, Machine learning analysis, which is a type of AI, is applied

to elucidate relationships between chemical characteristics and geometrical properties of minerals. The analysis helps to interpret complex relationships between factors of minerals that we do not know. Considering the analysis result, I interpret connections between the relationship and deformation mechanisms of mineral.

Python is used as a main programming language conducting the computer simulation and machine learning analysis in the studies. Although Python has a disadvantage including relatively slower execution speed than other programming language, I considered that Python is the most optimize programming language to perform the computer simulations and the machine learning analysis in these studies based on advantages including flexibility and diversity of library.

Part 1.

I present a numerical model representing shape change of isolated K-feldspar inclusions within deformed quartz host grains in a narrow shear zone developed in Teshima granite, Ryoke metamorphic belt, Japan. The shape-changes of the inclusions within the natural shear zone is calculated by using computer simulation which is built by applying time variations of geological scales to the numerical model constructed as non-linear differential equation for time factor. The other variations of the numerical model including temperature and paleo-stress are estimated from microstructures of the shear zone. Under the assumption that the estimated conditions are end members of deformation conditions from the simulation, I simulate the shape-changes and visualize shape change patterns during not only deformation but also post-deformational annealing according to various deformation duration. The patterns of post-deformational annealing are calculated by applying zero of a differential stress to the numerical model. Deformation duration in the shear zone is calculated by finding out the best-

matched shape change pattern with the patterns observed from the shear zone.

Part 2.

I present relationships between chemical characteristics and geometrical properties of spinel grains collected from a dunite sample within the Transition Zone in the Horoman peridotite complex in Hokkaido, Japan, by using machine learning analysis. For applying analyzed data for the spinel grains to the machine learning algorithms, the following sequence is applied: 1) analyzing chemical characteristics, 2) data pre-processing, 3) data clustering, 4) data splitting, 5) classification and node analysis, 6) estimating feature importance. To accelerate calculation speed and improve accuracy of machine learning analysis, data standardization is essential process. In stage of the data pre-processing, the analyzed data is standardized as format getting specific scale. The standardized data are presented as a scatterplot. To identify clusters of the data, Mean-shift Clustering (MCA) method is conducted to the scatterplot. By considering the type of clusters, the machine learning analysis including classification and estimating feature importance are carried out. Given the results of the machine learning analysis, I interpret connections between the relationships and deformation mechanisms.

Part 1:

A shape-change model for isolated K-feldspar inclusions within a micro-shear zone developed in the Teshima granite, Ryoke metamorphic belt, Japan: Estimation of the duration of deformation in a natural shear zone

Abstract

A micro-shear zone developed in the Teshima granite in the Ryoke metamorphic belt of Japan contains isolated K-feldspar inclusions showing various shapes within deformed host quartz grains. I present a shape-change model for isolated K-feldspar inclusions based on mathematical equations introduced by Toriumi (1987) and Okamoto and Michibayashi (2005). The shape-change model is a non-linear differential equation that considers stress, inclusion size, temperature, and the duration of deformation. To calculate the shape-change pattern (i.e., the aspect ratio and size of inclusions) with respect to deformation duration using the model, I used values for deformation temperature ($\sim 500\text{--}600\text{ }^{\circ}\text{C}$) and paleo-stress ($90 \pm 10\text{ MPa}$) estimated from deformed quartz microstructures within the micro-shear zone. Shape-change patterns were obtained by calculating the model at the estimated range of temperatures with an interval of $25\text{ }^{\circ}\text{C}$ and at the estimated paleo-stress. Shape-change patterns were subsequently corrected by compensating for the effect of post-deformation annealing during exhumation of the micro-shear zone. Deformation duration was estimated by identifying the shape-change pattern calculated by the model that most closely corresponded to the observed shape-change pattern for the micro-shear zone and considering the cooling rate of the Ryoke belt proposed by Okudaira et al. (2001). The resultant deformation duration of the micro-shear zone is estimated as $16500\text{--}8400\text{ yr}$ under conditions of $T = 550\text{ }^{\circ}\text{C}$ and $\sigma = 90 \pm 10\text{ MPa}$. Shear strain in the micro-shear zone is calculated as $50\text{--}260$ by multiplying the shear strain rate by the deformation duration.

1. Introduction

Naturally deformed rocks usually contain many types of isolated mineral inclusion within deformed host grains, and the textures and sizes of the inclusions can be observed using an optical microscope. Isolated mineral inclusions have two main characteristics that can better reflect deformation conditions compared with normal mineral grains. First, in isolated inclusions the effect of grain boundary migration is likely to be negligible because the inclusions are pinned by the surrounding host grain. This first characteristic allows an assumption to be made that the volume of the inclusion is conserved regardless of the changing shape of the inclusion and deformation conditions. Second, isolated inclusions commonly consist of a single crystal and therefore do not include complicated boundary networks such as triple junctions. Therefore, it is valid to ignore the effects of the boundary network in studying the textural evolution of such inclusions.

Some previous studies have examined the relationship between the shape change (aspect ratio change) of isolated mineral inclusions and deformation conditions by mathematical modeling based on the two above-mentioned characteristics of such inclusions that differ from those of normal mineral grains (Toriumi, 1981, 1987; Okamoto and Michibayashi, 2005). Toriumi (1981, 1987) first proposed mathematical equations describing the shape-change of isolated mineral inclusions with changing deformation conditions, implying a possible application of the numerical model to observed data. Okamoto and Michibayashi (2005) used the textures of garnet inclusions to estimate the uniaxial deformation conditions of granulite-facies quartzite in the Lutzow–Holm Complex of Antarctica by modeling the shape-change of garnet inclusions based on the mathematical equations proposed by Toriumi (1987). However, there are no studies have used numerical models to calculate the shape change of isolated mineral inclusions in natural shear zones and estimated the duration of deformation in natural shear zones by comparing model results and observed data.

In this paper, I introduce a numerical model describing the shape change of isolated mineral inclusions in a natural shear zone with respect to varied simple-shear conditions. I present shape-change patterns of isolated inclusions with respect to changing deformation temperature, stress, deformation duration, and cooling rate. I identify the calculated shape-change patterns that best match the shape-change pattern of K-feldspar inclusions observed from a natural shear zone in Teshima granite by

comparing the model output with these data. On the basis of the results, I discuss the deformation duration and shear strain of the natural shear zone.

2. Deformation model

The deformation model developed in this study represents the change in shape (aspect ratio) of single crystalline inclusions embedded in host mineral grains with respect to various deformation conditions including inclusion size, temperature of deformation, differential stress, and deformation duration. I consider that an inclusion is deformed by pure shear in two dimensions with stresses of maximum principal stress (σ_1) > minimum principal stress (σ_2). The principal stresses are orientated parallel to the principal stretch axes of the inclusion, with the long axis of the inclusion (a) being parallel to σ_2 (Fig. 1). The deformation model is modified from the equations of Okamoto and Michibayashi (2005) and explains the shape change of an inclusion as uniaxial extension in three dimensions to enable application of the deformation model to simple shear in three dimensions.

The shape change of an inclusion in the deformation model is explained by three mechanisms: diffusion creep, rounding process, and dislocation creep. Diffusion creep that is involved in the shape change of an inclusion originates from a concentration of vacancies generating diffusive flow along the interface boundary between the inclusion and its host grain under differential stress (Coble, 1963; Poirier, 1985). However, the inclusion tends to a spherical shape to minimize surface energy during and after deformation. The mechanism that gives rise to the spherical shape is affected by interfacial tension between the inclusion and the host grain, which is achieved by interface diffusion, also known as the rounding process (Kingery et al., 1976; Toriumi, 1987; Okamoto and Michibayashi, 2005). Diffusion creep and the rounding process influence the shape change of an inclusion by interface diffusion. Therefore, I refer to this mechanism as the diffusion process (diffusion creep + rounding process). I do not consider volume diffusion in diffusion creep and rounding process, but only interface boundary diffusion, as volume diffusion is 10^4 times slower than interface boundary diffusion under natural deformation conditions (Shewmon, 1963; Joesten, 1991; Lasaga, 1998). Dislocation creep also influences the shape change of an inclusion, and I applied this to the deformation model by modifying

a power-law flow law equation for dislocation creep. Then, I deduced an equation describing the shape change of an inclusion in pure-shear condition via the three mechanisms, based on the equation proposed by Okamoto and Michibayashi (2005). (Equation 16 of Okamoto and Michibayashi [2005])

2.1. Equation describing the diffusion process

I deduced an equation representing the shape change of an inclusion by the diffusion process in two dimensions (Toriumi, 1987; Okamoto and Michibayashi, 2005). The equation is based on the concentration of vacancies and on the vacancy flux controlled by differential stress and interfacial tension in inclusions. I assumed five preconditions to derive the simplest equation. First, interfacial tension is not related to the crystallographic orientation of minerals. Second, the total volume of an inclusion does not change with the shape of inclusion and deformation conditions. Third, all inclusions are single crystals. Fourth, the shape of an inclusion before deformation is always a perfect sphere. Fifth, the viscosity contrast between an inclusion and its host grain is negligible.

On the basis of the fact that both the long (a) and short (b) axes of an inclusion change with time under differential stress as $a + da$ and $b + db$, respectively, I defined equations for the volume (V) and radius of curvature at the crest of an inclusion (Fig. 1):

$$V = ab\pi = (a + da)(b + db)\pi \quad (1)$$

$$r_1 = \frac{a^2}{b}, r_2 = \frac{b^2}{a} \quad (2)$$

where r_1 and r_2 are the radius of curvature at the crest of the short and long axes of the inclusion, respectively. The aspect ratio (L) and size (R) of an inclusion are expressed as

$$L = \frac{b}{a} \quad (3)$$

$$R = \sqrt{ab} \quad (4)$$

Therefore, L decreases when the inclusion has a more elongated shape (Fig. 1a), and $L = 1$ for a perfectly spherical inclusion. Equations (1) to (4) express all states of shape of an inclusion. The concentration of vacancies at the crests of long ($C_{v,a}$) and short ($C_{v,b}$) axes is defined by

$$C_{v,a} = C_{v,0} \exp \left[\frac{\Omega \left(-\frac{Y_s}{r_2} - \sigma_2 \right)}{kT} \right] \quad (5)$$

$$C_{v,b} = C_{v,0} \exp \left[\frac{\Omega \left(-\frac{Y_s}{r_1} - \sigma_1 \right)}{kT} \right] \quad (6)$$

The equations mean that concentrations of where $C_{v,0}$ is the concentration of vacancies on a flat surface under stress-free conditions, k is Boltzmann's constant, Ω is the volume of a vacancy, and T is temperature in Kelvin. The equation (5) and (6) mean that the number of vacancies in the vacancy concentrations at crests increases with decreasing curvature and principal stress. The mean distance between the crests of long and short axes is l . Regarding $|\Omega(-Y_s/r_i - \sigma_i)| \ll kT$, the mean gradient of the concentration of vacancies can thus be written as

$$\begin{aligned} \text{grad } C_v &= (C_{v,b} - C_{v,a})/l \\ &= -\frac{C_{v,0}\Omega \left[Y_s \left(\frac{1}{r_1} - \frac{1}{r_2} \right) + (\sigma_1 - \sigma_2) \right]}{kT} \end{aligned} \quad (7)$$

The mean distance between the crests (l) is expressed by $h\sqrt{a^2 + b^2}$, where h is the geometrical constant of an ellipse, which has a range of 1 to $\pi/2\sqrt{2}$. Based on the equation (7) for $\text{grad } C_v$ and Fick's first law, I derived the equation for vacancy flux (J_v) as

$$\begin{aligned} J_v &= -D_v \text{grad } C_v = -\frac{D_v(C_{v,b} - C_{v,a})}{l} = -\frac{D_v(C_{v,b} - C_{v,a})}{h\sqrt{a^2 + b^2}} \\ &= -\frac{D_v(C_{v,b} - C_{v,a})}{hkT\sqrt{a^2 + b^2}} = \frac{D_v C_{v,0} \Omega}{hkT\sqrt{a^2 + b^2}} \left[Y_s \left(\frac{1}{r_1} - \frac{1}{r_2} \right) + (\sigma_1 - \sigma_2) \right] \end{aligned} \quad (8)$$

The D_v is the interface boundary diffusion coefficient of vacancies. The flux of material (J_m) is the inverse of the flux of vacancy (J_v). Therefore, the flux of material is defined by

$$\begin{aligned} J_m &= -J_v \\ J_m &= \frac{-D_v C_{v,0} \Omega}{hkT\sqrt{a^2 + b^2}} \left[Y_s \left(\frac{1}{r_1} - \frac{1}{r_2} \right) + (\sigma_1 - \sigma_2) \right] \end{aligned} \quad (9)$$

Due to the given the relationship $D_{gb} = D_v C_{v,0} \Omega$ and the equation for the radius of curvature, the

equation for material flux (J_m) can be rewritten as

$$J_m = \frac{-D_{gb}}{hkT\sqrt{a^2 + b^2}} \left[\gamma_s \left(\frac{1}{r_1} - \frac{1}{r_2} \right) + (\sigma_1 - \sigma_2) \right]$$

$$J_m = \frac{D_{gb}}{hkT\sqrt{1 + L^2}} \left[\gamma_s \left(\frac{1 - L^3}{b^2} \right) + \left(\frac{\sigma_1 - \sigma_2}{a} \right) \right] \quad (10)$$

The volume of material moved by interface diffusion (dV) during dt is proportionally related to J_m (Fig. 1b). I express the volume of material moved by interface diffusion as

$$dV = J_m \Omega S dt \quad (11)$$

The where S is the total area over which material flows along the interface boundary. Thus, S is defined by 2δ , where δ is the thickness of the interface boundary. The reason for multiplying δ by 2 is that flow of material occurs on both the upper and lower boundaries of an inclusion. The volume change can also be expressed as an equation for volume change (dV) with respect to change in the length of the short axis (da):

$$dV = \frac{V}{4a} da \quad (12)$$

The change in aspect ratio (dL) with da is derived by

$$dL = -\frac{2b}{a^2} da \quad (13)$$

By combining Equations (13) and (12), the equation representing aspect ratio change with volume change is

$$dL = -\frac{8L}{V} dV \quad (14)$$

The volume change component (dV) in Equation (14) was defined as Equation (11), and J_m in Equation (11) was expressed as Equation (10). Therefore, Equation (14) can be re-expressed as

$$dL = -\frac{8L}{V} J_m \Omega S dt$$

$$dL = -\frac{8L}{V} \frac{D_{gb} \Omega S}{hkT\sqrt{1 + L^2}} \left[\gamma_s \left(\frac{1 - L^3}{b^2} \right) + \left(\frac{\sigma_1 - \sigma_2}{a} \right) \right] dt \quad (15)$$

Then, I deduced the equation describing the shape-change rate of an inclusion by rearranging each

parameter:

$$dL = C \frac{D_{gb}\Omega\delta}{R^3kT} \frac{L}{\sqrt{1+L^2}} \left[\frac{(1-L^3)\gamma_s}{RL} - \sigma\sqrt{L} \right] dt \quad (16)$$

The where C is a geometrical constant computed as $16/h\pi$, and σ is differential stress defined by $\sigma_1 - \sigma_2$.

2.2. Equation for dislocation creep

The equation representing the shape change rate of an inclusion for dislocation creep is derived by modifying the power-law flow law for dislocation creep. The basic structure of the power-law flow law is

$$\frac{d\varepsilon}{dt} = A\sigma^n \exp\left(-\frac{Q}{RT}\right) \quad (17)$$

The where $d\varepsilon/dt$ is strain rate, A is a constant, σ is differential stress, n is the stress exponent, Q is the activation energy, R is the gas constant, and T is temperature in Kelvin. The change in axial strain ($d\varepsilon$) is defined by $d\varepsilon = da/a$. The equation (18) for the change of axial strain can be re-written by combining with Equation (13) as Equation (19), which represents the change in aspect ratio with change in the long axis:

$$da = a d\varepsilon \quad (18)$$

$$dL = -\frac{2ab}{a^2} d\varepsilon \quad (19)$$

And the equation (19) can be rewritten by multiplying both sides by $1/dt$ as

$$\frac{dL}{dt} = -\frac{2b}{a} \frac{d\varepsilon}{dt} \quad (20)$$

$$\frac{d\varepsilon}{dt} = -\frac{1}{2} \left(\frac{1}{L}\right) \left(\frac{dL}{dt}\right) \quad (21)$$

Thus, the traditional flow law of dislocation creep is rewritten as

$$\frac{dL}{dt} = -2LA\sigma^n \exp\left(-\frac{Q}{RT}\right) \quad (22)$$

2.3. Whole equation

I deduced the whole equation describing the shape-change rate of an inclusion by combining Equation (16) describing the shape change resulting from the diffusion process and Equation (22) representing the shape change resulting from dislocation creep:

$$\frac{dL}{dt} = C \frac{D_{gb}\Omega\delta}{R^3kT} \frac{L}{\sqrt{1+L^2}} \left[\frac{(1-L^3)\Upsilon_s}{RL} - \sigma\sqrt{L} \right] - 2LA\sigma^n \exp\left(-\frac{Q}{RT}\right) \quad (23)$$

2.4. Simple shear

Equation (23) of the deformation model represents the shape change (aspect ratio change) of an inclusion by pure shear in two dimensions. However, the deformation model can be applied to simple shear of an inclusion in three dimensions because of the specific characteristics of simple shear. For homogeneous deformation, a deformation matrix of simple shear in two dimensions is written as

$$D_{simple\ shear} = \begin{bmatrix} 1 & \alpha \\ 0 & 1 \end{bmatrix}$$

where α is shear strain (Ramsay and Huber, 1983; Fossen and Tikoff, 1993). This simple shear deformation matrix can be expressed as a Mohr circle (Fig. 2a). The Mohr circle has a particular shape that is bordered with a D_{ii} axis. In this circle, a line can be drawn that passes through the center point of the circle and the (0, 0) point. The principal stretch axes (S_1 and S_2) are the points where the line and the circle intersect. The angle between the line and the D_{ii} axis is the rotation angle of simple shear. If I rotate the circle by this angle, I should observe a new circle representing pure shear, which intersects the D_{ii} axis at two points (Fig. 2b). The two points of the new circle are the new principal stretch axes corresponding to pure shear (S'_1 and S'_2). In these two circles, the aspect ratio of the principal stretch axes of simple shear (S_1 and S_2) is the same as that of pure shear (S'_1 and S'_2) because the circle size corresponding to simple shear does not change with rotation. This means that the deformation model showing the shape-change of an inclusion by pure shear can be applied to simple shear because the aspect ratio of the inclusion is not changed by pure or simple shear.

The shape change of an inclusion under perfect simple shear in three dimensions does not occur on the Y-axis but occurs on the X- and Z-axes. Therefore, if I observe the X-Z plane (or b-plane) in simple shear in three dimensions, I can analyze the entire shape-change of an inclusion. This means

that simple shear in three dimensions can be explained by a two-dimensional deformation model because the X–Z plane is two-dimensional (Fig. 2c).

The characteristics of simple shear in three dimensions mean that the change in aspect ratio of an inclusion under simple shear can be explained by the change in aspect ratio of an inclusion under pure shear and that simple shear in three dimensions can be represented by deformation in two dimensions by the X–Z plane of a shear zone. Then, the shape change of an inclusion in three dimensions under simple shear can be described by Equation (23), which describes the shape change of an inclusion in two dimensions of pure shear.

3. Application to K-feldspar inclusions within host quartz grains

3.1. Geological setting and sample description

I applied Equation (23) to estimate the duration of deformation in a natural shear zone by investigating K-feldspar inclusion within the shear zone. The sample was collected from Teshima Island in the Shiwaku Islands within the Ryoke high-temperature–low-pressure metamorphic belt, Japan (Fig. 3a). The southern part of Teshima Island is composed of coarse-grained gneissic hornblende biotite granite, and the northern part comprises hornfels and medium-grained weakly gneissic biotite granite (Michibayashi and Murakami, 2007). The sample was taken from a sinistral micro-shear zone measuring 1–2 cm in width within biotite granite on the northern part of the island (Fig. 3b). Foliation is defined by the preferred orientation of minerals, including quartz and biotite. The foliation gradually changes orientation from high angle to low angle to the shear zone boundary with decreasing distance from the micro-shear zone (Fig. 3b–c). A mineral elongation lineation is observed on the foliation. Thin sections cut perpendicular to the foliation and parallel to the lineation on the foliation surface were used to analyze microstructures and textures of K-feldspar inclusions (Fig 3c).

The sample is composed mainly of quartz, K-feldspar, and biotite, with minor muscovite and plagioclase. The grain size of individual minerals in the micro-shear zone is much finer than that in the wall rock. Quartz in the micro-shear zone consists mainly of dynamically recrystallized grains with some relict grains. Locally relict grains show sweeping undulose extinction and deformation bands.

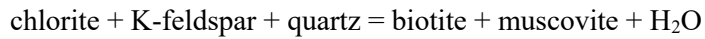
Some of the relict grains show a core-and-mantle structure consisting of subgrains and recrystallized grains surrounding relict grains (Fig. 4a–b). Other quartz grains exhibit lobate grain boundaries and migration microstructures (Fig. 4c–d). The relict and recrystallized quartz grains have a shape preferred orientation that defines the foliation. Figure 5 presents crystallographic preferred orientations (CPOs) of quartz grains from both the micro-shear zone and wall rock. CPOs of quartz grains were analyzed by using a scanning electron microscope (SEM) with an electron backscatter diffraction (EBSD) (HITACHI S-3400N Type II at the Petrology and Mineralogy Laboratory of Nagoya University). The structural framework of CPOs is defined by the foliation normal (Z) and the lineation (X). CPO patterns reveal that maxima of $\langle c \rangle$ and $\langle a \rangle$ axes for quartz aggregates in the micro-shear zone are clearly stronger than those of quartz aggregates in the wall rock (Fig. 5). These microstructures indicate that quartz grains in the micro-shear zone were deformed by plastic deformation accommodated by dislocation creep with mixed subgrain rotation (SGR) and grain boundary migration (GBM) recrystallization as the dominant dynamic recrystallization processes (Hirth and Tullis, 1992; Stipp et al., 2002). K-feldspar grains within the micro-shear zone show a shape preferred orientation that defines the foliation. However, the deformation structures of K-feldspar grains cannot be identified because of overgrown strain-free muscovite and biotite grains (Fig. 4e–f). Locally remnant K-feldspar grains display vague deformation structures, including sweeping undulose extinction and deformation twinning. K-feldspar inclusions are observed as isolated single crystals within quartz grains through all parts of the thin section. The inclusions exhibit mostly ellipsoidal shapes with a range of aspect ratios.

Although most of the deformation in the micro-shear zone is not perfect simple shear but sub-simple shear, I assumed the deformation as simple shear to apply the deformation model to the micro-shear zone.

3.2. Deformation conditions

The Deformation conditions, including temperature and paleo-stress, were inferred from microstructures in the studied sample. First, the deformation temperature was estimated based on the relationship between temperature and microstructures, including K-feldspar breakdown structures, CPO

patterns of deformed quartz, and quartz recrystallization mechanisms. The breakdown of K-feldspar occurred at 400–500 °C and 0.3–0.45 GPa, as inferred from the following reaction (Wang et al., 1986; Tokada, 1998):



I observed that deformed K-feldspar grains are overprinted by strain-free euhedral biotite and muscovite grains within both the micro-shear zone and wall rock (Fig. 4e–f). This structural pattern implies that the micro-shear zone was formed before K-feldspar breakdown. In other words, the shearing within the shear zone occurred at a temperature of 400–500 °C or higher. The pattern of CPOs of quartz aggregates from the micro-shear zone shows that the maxima of <a> axes are sub-parallel to the lineation and that the maxima of <c> axes are not only concentrated normal to the lineation but are also along the Z-axis (Fig. 5b). These patterns of maxima of <a> and <c> axes of quartz aggregates suggest that a mixed rhomb + prism <a> slip system, dominated by prism <a> slip, was active in the shear zone. Slip systems involving the <a> direction are usually active on prism, rhomb, and basal planes at temperatures of 280 to 650 °C (Schmid and Casey, 1986; Passchier and Trouw, 2005). Furthermore, the mixed rhomb + prism <a> slip system is usually dominant at temperatures of 400–500 °C, which is much higher than the temperature conditions under which the basal <a> slip system operates (Lister and Dornsiepen, 1982; Mainprice et al., 1986; Mancktelow, 1987; Stipp et al., 2002). However, here I considered the temperature conditions of deformation as 500–600 °C because the CPO pattern for the micro-shear zone show that prism <a> slip is dominant over rhomb <a> slip; i.e., I considered that the quartz grains within the micro-shear zone were deformed at a range of temperatures between that of mixed rhomb + prism <a> slip and solely prism <a> slip. The adopted temperature range of micro-shear zone deformation of 500–600 °C also corresponds to the temperature conditions under which mixed SGR and GBM recrystallization mechanisms of quartz are activated (Mainprice et al., 1986, Stipp et al., 2002, 2016).

To estimate the paleo-stress of the micro-shear zone, I measured the sizes of recrystallized quartz grains within the shear zone by using EBSD data with AZTEC software (Fig. 6). Raw data were obtained using a data collection rate of 49 patterns per second and a step size of 1 µm. Grain construction from the raw data was achieved by using CHANNEL 5 software and defining high-angle grain

boundaries using a critical misorientation angle of 10° . Dauphin twin boundaries were removed by extracting a 60° angle of rotation from the $\langle 0001 \rangle$ axis of the quartz grains. Recrystallized grains were extracted from the raw data by removing highly distorted grains from the entire dataset (Wright et al., 2011; Cross et al., 2017). Figure 6 shows populations of whole grains and recrystallized grains. The mean recrystallized grain size was measured by calculating the root mean square (RMS) of the grains to correspond with the regime 2–3 piezometer of Stipp and Tullis (2003). The mean grain size of whole grains is $16 \mu\text{m}$ (Fig. 6a), and the mean recrystallized grain size is $12.5 \mu\text{m}$ (Fig. 6b). Then, I estimated a flow stress value for the micro-shear zone of $90 \pm 10 \text{ MPa}$ by applying the mean recrystallized grain size (D) to the piezometer of Stipp and Tullis (2003) whereby $D = 3631\sigma^{-1.26}$.

3.3. K-feldspar inclusions

3.3.1. Shape analysis of K-feldspar inclusions

K-feldspar inclusions occur as isolated inclusions within the quartz matrix (Fig. 7). Observations under an optical microscope show that the inclusions do not display marked differences in optical characteristics compared with the quartz matrix under cross-polarized light (XPL), but display a pinkish color and distinct inclusion boundaries with elongated shapes under plane-polarized light (PPL) (Fig. 7a–d).

To clearly identify the mineral species of inclusions isolated within the quartz matrix, I analyzed inclusions using a Thermo Scientific Nicolet Almega XR Raman spectrometer at the Petrology and Mineralogy Laboratory of Nagoya University. Raman spectra of the measured inclusions display strong Raman bands from 0 to 550 cm^{-1} of Raman shift, with the strongest Raman band at around 513.1 cm^{-1} (Fig 7e). The characteristics of Raman spectra of the inclusions are similar to those of K-rich alkali-feldspar, such as sanidine, orthoclase, and microcline (Freeman et al., 2008). In particular, a single peak at 282.7 cm^{-1} in the spectra of the inclusions corresponds to a peak in orthoclase spectra. Therefore, I considered that the elongated pinkish inclusions are K-feldspar inclusions. I measured the size and aspect ratio of the K-feldspar inclusions by using an optical microscope.

Three criteria were applied in selecting K-feldspar inclusions for shape analysis. The first

criterion is the size of inclusions. For inclusions that are suspended or cut on the edge of the thin section, I cannot measure their true size and aspect ratio. Therefore, I identified inclusions that were smaller than the width of the thin section (50 μm) to avoid the cutting effect. The second criterion is the orientation of inclusions. I identified inclusions whose long-axis orientations were parallel or sub-parallel to the orientation of the foliation, to analyze those inclusions influenced by shear strain. The third criterion was the location of inclusions. Inclusions that are larger than the size of quartz grains should be affected by the grain boundaries of quartz grains. Therefore, I identified inclusions that were much smaller than the host quartz grains. After selecting inclusions that fulfilled the three criteria ($n = 1128$) within the sample of micro-shear zone, I traced their outlines from photomicrographs and analyzed their size and aspect ratio using Image J Software.

3.3.2. L - $2R$ patterns of K-feldspar inclusions

The aspect ratio (L) and diameter ($2R$) of the selected inclusions were measured in a thin section cut along the X-Z plane (or b-plane). The resultant data are presented as a scatterplot of L versus $2R$ (Fig. 8a). To identify the pattern of data in the scatterplot, I simplified the plot by calculating the mean aspect ratio with respect to 21 bins of inclusion diameter (Table 1), the results of which are presented in Figure 8b. The diameters of the inclusions are distributed from 1 to 40 μm , and the highest frequency of inclusion diameter is 7–8 μm . The aspect ratio of inclusions varies with diameter (Fig. 8b). Inclusions that are smaller than 4 μm commonly show a relatively spherical shape, as indicated by mean aspect ratios of 0.5 to 0.7. Mean aspect ratio decreases with increasing diameter of inclusions, meaning that inclusions show increasing elongation with increasing diameter until a diameter of 13–14 μm , for which the mean aspect ratio is 0.27. The mean aspect ratio of inclusions that are larger than 13–14 μm gradually increases with increasing diameter to reach 0.4 at a diameter of 36–40 μm .

4. Results of the deformation model

4.1. Parameters in the mathematical equation for the deformation model

Equation (23) describes the shape-change of inclusions within host grains in two dimensions under pure shear, and the equation can be applied to simple shear in three dimensions, as explained above. Each parameter in Equation (23) needs to be defined to apply the deformation model to K-feldspar inclusions within quartz host grains in the micro-shear zone. The assigned parameter values are given Table 2. L is the aspect ratio of K-feldspar inclusions and is defined by Equation (3). R , the size of inclusions, is given by Equation (4), and is the radius of a inclusion (circle with equivalent area to the inclusion); I used $2R$ in the aspect ratio–size patterns because inclusion size was measured as the diameter.

D_{gb} is the interface diffusion coefficient of the slowest atom in the interface between inclusions and host grains, as the slowest atom controls the diffusion rate in minerals. Although the slowest atom varies with mineral species, Si is the slowest atom within minerals of the feldspar series (Cherniak, 2003; Brady and Cherniak, 2010; Cherniak, 2010). I derived the Si interface diffusion coefficient by referring to previous studies, although there has been no direct estimation of the Si interface diffusion coefficient between K-feldspar and quartz grains. Cherniak (2003) measured the volume diffusion coefficient of Si and K in plagioclase feldspars. Using data from that study, I calculated that the volume diffusion of Si in feldspar is 2×10^6 times slower than the volume diffusion of K under the adopted deformation temperature range (500–650 °C) by extrapolation. In addition, Farver and Yund (1995) estimated the interface diffusion coefficient of K at the interface boundary between K-feldspar and quartz grains. By multiplying the difference between the volume diffusion coefficients of the two atoms, I derived the Si interface diffusion coefficient between K-feldspar inclusions and quartz grains. t is deformation duration in seconds, σ is differential stress, and Ω is the volume of a vacancy (Table 3). In this study, the volume of a vacancy was considered to be the volume of a Si atom.

I calculated the value of interfacial tension between inclusions and host grains, γ_s , based on the equation of Hiraga et al. (2002), who suggested the relationship between interfacial tension and dihedral angle at a quartz–albite–quartz triple junction is $\gamma_{al-qtz} = \gamma_{qtz-qtz}/2\cos(\theta/2)$. Thus, the interfacial

tension between a K-feldspar inclusion and quartz host grain can be estimated by adopting previously published values, which are $\gamma_{\text{qtz-qtz}} = 270 \pm 110 \text{ mJ/m}^2$ and dihedral angle at a quartz-K-feldspar-quartz triple junction = 105° (Holness and Clemens, 1999). Then, I calculated the interfacial tension between K-feldspar and quartz ($\gamma_{\text{K-fd-qtz}}$) as $220 \pm 90 \text{ mJ/m}^2$. k is Boltzmann's constant, and T is temperature in Kelvin. The constant C ranges from 4.58 at $L = 1.0$, to 5.08 at $L = 0$. To specify C , I set the constant as 4.83 (i.e., the mean value). The values of parameters for dislocation, including the stress exponent (n) and constants (Q and A) were taken from the flow law for albite. I utilized the flow law for albite because there are insufficient data for K-feldspar (Table 1). The parameters in Equation (23) are those under hydrous conditions because deformation of the sample material took place under moderate-temperature and wet conditions.

4.2. L - $2R$ patterns generated by the deformation model

Having established the estimated deformation conditions, as above, the deformation temperature and differential stress in the model were set as 500–600 °C (773.15–873.15 K) and 50–200 MPa, respectively. Deformation duration was assumed to range from 100 to 10,000 yr, since there are no geochronological data. Figure 9 shows the change in aspect ratio of inclusions with varying deformation conditions and deformation durations. The shape-changes revealed in L - $2R$ patterns were modeled as 15 cases with respect to various deformation conditions and deformation durations within $T = 500$ – 600 °C (773.15–873.15 K), $\sigma = 50$ – 200 MPa, and duration (t) = 100–10,000 yr. The Y-axis of the L - $2R$ patterns in Figure 9 represents aspect ratios of the inclusions, as calculated using Equation (3). The value of 1.0 on the Y-axis corresponds to a perfect circular shape of an inclusion. The X-axis is inclusion size, defined as the diameter of the inclusions, which is denoted as $2R$ because R defined by Equation (4) is the radius of an inclusion. I calculated inclusion sizes of 0.1 to 40 μm in the model. To effectively explain the effects of deformation conditions and deformation duration on the relationship between inclusion aspect ratio and diameter, I chose two points and three domains that help to explain the patterns (Fig. 9). Point I corresponds to the minimum aspect ratio, and point II marks the

greatest change in the slope of the $L-2R$ relationship while maintaining a positive slope. Domain 1 is defined by an inclusion size range smaller than that corresponding to point I, domain 2 is defined by an inclusion size corresponding to between points I and II, and domain 3 is defined by an inclusion size larger than that corresponding to point II.

For the data presented in Figure 9, the aspect ratio change of inclusions depends on four factors: inclusion size, deformation temperature, differential stress, and deformation duration. First, inclusion size clearly affects the change in aspect ratio in domains 1 and 2 for all 15 presented cases. In domain 1, aspect ratio decreases with increasing inclusion size; i.e., smaller inclusions are less deformed than larger inclusions. From the Y-axis, aspect ratio increases with increasing size of inclusions until point II (i.e., in domains 2), whereas domain 3 shows grain-size-insensitive behavior. In the 15 cases, aspect ratio is essentially constant through domain 3 regardless of changing inclusion size, meaning that there is no variation in the amount of deformation. Second, the effect of temperature extends to all domains, whereby aspect ratios of inclusions decrease with increasing temperature, indicating that inclusions become more deformed with increasing temperature. Inclusion sizes corresponding to point 1 also increase with increasing temperature. The coverage of domains also changes with varying temperature, whereby the ranges of domains 1 and 2 become wider with rising temperature but that of domain 3 becomes narrower. Third, $L-2R$ patterns in all domains show differential-stress-sensitive behavior. An increase in differential stress is associated with decreasing aspect ratio in all domains. However, the range of each domain does not show substantial change in spite of altering differential stress. Fourth, deformation duration controls shape-change patterns in all domains, whereby aspect ratios of inclusions typically decrease with increasing deformation duration, and the aspect ratio corresponding to point 1 decreases markedly with increasing deformation duration, but there is no such pronounced change in the inclusion size corresponding to point 1.

4.3. $L-2R$ patterns: comparison between deformation model results and K-feldspar inclusion data

Deformation conditions of the micro-shear zone (temperature and differential stress) were

evaluated by investigating microstructures. Here, the deformation conditions were applied to the deformation model to estimate shape-change patterns of K-feldspar inclusions. The deformation model generates aspect ratio change with varying inclusion size with respect to the deformation conditions and deformation duration. In this section, I identify the $L-2R$ patterns generated by the deformation model that best fit the observed inclusion $L-2R$ data, through which process the corresponding modeled deformation conditions and deformation duration of the micro-shear zone are also identified. The best-fitting $L-2R$ pattern generated by the deformation model is calculated by the simple least squares method of residuals of values of the difference between the aspect ratios of the model and those of the observed inclusions ($L_i^{model} - L_i^{obs}$):

$$\Delta L^2 = \frac{1}{21} \sum_i^{21} (L_i^{model} - L_i^{obs})$$

The where L_i^{model} and L_i^{obs} are the values of aspect ratios calculated by the deformation model and the values of aspect ratios observed for K-feldspar inclusions, respectively. A small value of ΔL^2 means that the $L-2R$ pattern of the deformation model is well matched with the $L-2R$ pattern of the observed inclusions.

Figure 10 shows best-fitting $L-2R$ patterns generated by the deformation model and $L-2R$ patterns for the observed K-feldspar inclusions for each of five cases. Differential stress is constant because the value was estimated as 90 ± 10 MPa. Deformation temperature and deformation_duration differ between cases to achieve the best-fitting $L-2R$ pattern. Deformation duration decreases markedly with increasing deformation temperature (375000–195000yr at 500 °C or 773.15 K; 75000–38500 yr at 525 °C or 798.15 K; 16500–8400 yr at 550 °C or 823.15 K; 3900–2000 yr at 575 °C or 848.15 K; 1020–540 yr at 600 °C or 873.15 K), and the shape of the best-fitting patterns becomes flatter. The results also show that the values of ΔL^2 are altered with changing temperature or deformation duration, meaning that the best-matching $L-2R$ pattern generated by the deformation model can be specifically defined for each condition. However, in all five cases there is a marked difference between modeled and observed aspect ratios for grain sizes between 0.1 and 7 μm . Although the disparity is

smaller for the highest deformation temperature (600 °C) and shortest deformation duration (1020–540 yr), it is too large to ignore. The reason for the disparity is a lack of post-deformation annealing, as discussed in sections 5.1 and 5.2.

5. Discussion

5.1. Effect of post-deformation annealing

Post-deformation annealing can affect the evolution of microstructures in naturally deformed rocks. I argue that the disparity between modeled and observed data in Figure 10 could be caused by the effect of post-deformation annealing. In this section, I discuss how the effect of annealing can be applied to the deformation model and show modeling results considering the effect.

During the post-deformation annealing stage, the size of normal mineral grains should increase and the number of grains per unit volume should decrease by consuming neighbor grains through GMB to minimize their surface energy. In the case of isolated inclusions, however, there is no way to minimize surface energy except to become spherical, because inclusion boundaries pinned by surrounding host grains are unable to migrate. I referred to this process as the “rounding process” above and consider that it is the only mechanism actively operating on isolated inclusions within host grains during annealing.

Basically, the effect of annealing, which causes a deformed ellipsoidal inclusion to change towards a spherical shape, becomes more marked with increasing deformation temperature, decreasing size of inclusion, and increasing duration of annealing (Fig. 11). In particular, the shapes of inclusions smaller than 10 μm change dramatically and become close to spherical. The effects are gradually enhanced in larger inclusions with decreasing cooling rate and increasing cooling duration. I calculated the effect of post-deformation annealing, considering only the rounding process, by using a differential stress of zero in Equation (23). The degree of change in aspect ratio generated by the effect of annealing is estimated as 0.025 of the aspect ratio interval, as variances of aspect ratio change differ with respect to the aspect ratio of inclusions. The degree of change in aspect ratio is related to temperature decreasing at specific rates from the deformation temperature to 350 °C, as I assumed that deformed rock is

exhumed from the deformation temperature after deformation. A temperature of 350 °C was established as the lower limit because the change in the shape of inclusions at temperatures lower than 350 °C is very small. In this model, there are two main controls on the effect of post-deformation annealing: cooling rate (in °C/Myr here) and cooling duration (yr). Cooling rate is inversely related to the duration of annealing, meaning that a high cooling rate is associated with a short duration of annealing. The effect of post-deformation annealing increases with longer cooling duration.

5.2. Evaluation of deformation duration and post-deformation annealing rate

Deformation duration was estimated by identifying the best-fitting $L-2R$ patterns of the deformation model, considering the effect of post-deformation annealing, with respect to the $L-2R$ pattern of the observed inclusions. I used two methods to evaluate the degree of similarity between the $L-2R$ patterns generated by the model and those observed from the natural micro-shear zone sample. I used the simple least squares method as utilized in section 4.3, and I also used the cooling rate of the Ryoke metamorphic belt as proposed by Okudaira et al. (2001) to assess the annealing rate.

Figure 12 shows the modeled $L-2R$ patterns for each deformation condition that best matches the observed $L-2R$ patterns by using the simple least squares method. The deformation duration is estimated as 10 yr of minimum spacing for deformation temperatures of 600 and 575 °C, and 50 yr of minimum spacing for deformation temperatures of 550, 525, and 500 °C.

Deformation The calculated deformation duration changes after applying the effect of post-deformation annealing, on account of the changed $L-2R$ patterns generated by the model (Fig. 12). In all cases, the calculated deformation duration when considering the annealing effect is longer than that without the effect. The difference in deformation duration increases with decreasing deformation temperature, as changing the $L-2R$ pattern takes longer under lower-temperature conditions. Cooling duration also increases with decreasing deformation temperature: for a deformation temperature of 600 °C, it takes 0.83–0.42 Myr of cooling to reach 350 °C, and it takes 70 times longer than this duration to reach 350 °C from a deformation temperature of 500 °C. The cooling rate becomes lower as

deformation temperature decreases because the rate is inversely related to cooling duration. Under all deformation conditions, values of ΔL^2 considering the effect of post-deformation annealing are about 10 times smaller than values of ΔL^2 without considering the effect. In other words, the modeled $L-2R$ patterns considering the effect of post-deformation annealing are about 10 times more similar to the patterns of observed K-feldspar inclusion data relative to those lacking the effect. Values of ΔL^2 gradually increase with increasing deformation temperature. As a result, the value of ΔL^2 considering the effect at 600 °C is the smallest, meaning that the $L-2R$ pattern for 600 °C most closely matches the observed $L-2R$ pattern.

However, there is no significant difference among the values of ΔL^2 for 550, 575, and 600 °C (0.006, 0.004, and 0.003, respectively), and these small differences lie within the margins of statistical error of the observed $L-2R$ pattern. Therefore, I applied the cooling rate data of the Ryoke metamorphic belt proposed by Okudaira et al. (2001), who suggested the Ryoke belt underwent two cooling stages: a first stage of rapid cooling in the temperature range from intrusion temperature to 300 °C, and a second stage of slow cooling in the temperature range from 300 to 100 °C. The exhumation rate is inferred to be 2–3 mm/yr during the first cooling stage and 0.1–0.2 mm/yr during the second. The exhumation rate can be converted to a cooling rate of 60–90 °C/Myr for the first cooling stage and 3–6 °C/Myr for the second, based on a mean geothermal gradient of 30 °C/km for an active continental margin or island arc (Sugimura and Uyeda, 1973).

In this study, I considered only the first rapid cooling stage to establish a reasonable case among the calculated $L-2R$ patterns for deformation temperatures of 550, 575, and 600 °C because the effect of post-deformation annealing is calculated for a temperature range extending from the deformation temperature to 350 °C. As a result, the best-matching shape-change pattern is that for 550 °C, because the cooling rate for this pattern is calculated as 40–70 °C/Myr, which is the closest range with the range of possible cooling rate (60–90 °C/Myr) of Okudaira et al. (2001).

5.3. Natural shear strain

Strain markers such as deformed fossils and veins have typically been used to estimate the shear strain of natural shear zones. However, there are still many problems in analyzing shear strain because strain markers are not common in natural shear zones. Although shear strain has been estimated from the orientation of foliation (e.g., Ramsay, 1980), this method is not suitable because the orientation of foliation does not reflect shear strain (Means, 1981; Ree, 1991). However, the shear strain of a natural shear zone can be analyzed using the following approach. Shear strain (γ) can be calculated from the shear strain rate multiplied by time (t). In the previous section, the deformation duration of the studied natural shear zone was estimated as 16500–8400 yr. Thus, the shear strain of the natural shear zone could be estimated if I knew the shear strain rate. To estimate the shear strain rate, I constructed a deformation mechanism map of deformed quartz within the micro-shear zone based on the flow law of dislocation creep (Hirth et al., 2001) and the flow law of diffusion creep (Brodie and Rutter, 2000) together with a paleo-piezometer (Stipp and Tullis, 2003) (Fig. 13).

Figure 13 shows a deformation mechanism map of quartz for deformation temperatures of 550 °C. In both cases, shearing in quartz grains within the shear zone is accommodated by dislocation creep as the dominant deformation mechanism. The strong CPOs of the quartz grains support the proposal that dislocation creep was active during shearing. Moreover, microstructures of recrystallization, which developed with dislocation creep, are observed in the quartz grains. The shear strain rate at a flow stress of 90 ± 10 MPa is estimated as 1.16×10^{-10} to $2.84 \times 10^{-10}/s$. Considering the deformation of the natural shear zone is not pure shear but simple shear, the calculated strain rate needs to convert to shear strain rate by considering the relationship between shear strain rate ($\dot{\gamma}$) and axial strain rate ($\dot{\epsilon}$).

$$\dot{\gamma} = \sqrt{3}\dot{\epsilon}$$

The converted strain rate range is 4.92×10^{-10} to $2.01 \times 10^{-10}/s$. As the estimated range of deformation duration is 16500–8400 yr, the shear strain range is calculated as 50–260 by multiplying the shear strain rate by deformation duration.

5.4. Mismatch between modeled results and observed data

The shape-change pattern of K-feldspar inclusions observed from the micro-shear zone shows some dissimilarity with the modeled pattern for some inclusion sizes. The dissimilarity may arise from two sources. The first is the statistical properties of the observed shape-change pattern of the K-feldspar inclusions. Some of the inclusions may not exactly reflect deformation calculated by the model owing to the heterogeneity of deformation. Although I measured as many inclusions as possible (>1000 inclusions) to obtain statistically meaningful data, the observed shape-change pattern may not capture the entire inclusion population. The second potential source of dissimilarity is the assumptions made in the model. As mentioned in sections 2.1 and 3, assumptions were made regarding the properties of inclusions and deformation. The dissimilarity between the modeled and observed shape-change patterns may be caused by differences between the model assumptions and natural conditions. In particular, the fourth assumption, that the shape of an inclusion before deformation is in all cases a perfect circle, and the fifth assumption, that the viscosity contrast between an inclusion and a host grain is negligible, may explain the dissimilarity, as inclusion shape and inclusion–grain viscosity contrast are strongly correlated with inclusion deformation. (Mancktelow and Pennacchioni, 2010; Mancktelow, 2011) However, I assumed that the shape of an inclusion before deformation is a perfect circle, but the aspect ratios of inclusions in wall rock of the micro-shear zone were measured as about 0.8. In the case of viscosity contrast, I assumed that the contrast is negligible on the basis of microstructures of the K-feldspar inclusions and end-member types of polyphase aggregates proposed by Handy (1990). K-feldspar inclusions in the studied micro-shear zone show elongated boudin shapes oriented parallel to the foliation, like the strong phase minerals of domain 2 of Handy (1990). Handy (1990) suggested that the strength contrast between strong and weak phases is low and that both phases are rheologically active. However, I cannot obtain the exact viscosity contrast between inclusions and host grains in the present study by reference solely to Handy (1990). A further assumption made in this study is that deformation is simple shear, even though most of the studied natural shear zone is not perfect simple shear but sub-simple shear, which could lead to a difference in inferred deformation conditions in the shear zone, such as differential stress and vorticity. Overall, it is considered that the differences between model assumptions and natural conditions explain the discrepancy between modeled and observed

inclusion shape data.

6. Conclusion

I applied a model based on mathematical equations describing the shape-change of inclusions by diffusion creep, rounding process, and dislocation creep to isolated K-feldspar inclusions in a micro-shear zone within Teshima granite in the Ryoke metamorphic belt, Japan, to evaluate the shape-change patterns of the inclusions with changing deformation duration. Deformation temperature and paleo-stress, which are utilized as parameters in the model, were estimated as 500–600 °C and 90 ± 10 MPa, respectively, from analysis of microstructures of quartz grains within the shear zone. In addition, I analyzed the properties of isolated K-feldspar inclusions, including diameter and aspect ratio, to compare with the modeled shape-change pattern of inclusions. I found that the modeled shape-change patterns of inclusions considering only the effect of deformation do not fully correspond to the shape-change pattern observed for natural shear zone K-feldspar inclusions because of the effect of post-deformation annealing. To correct for this dissimilarity, I applied the effect of post-deformation annealing to the modeled shape-change patterns and compared the resultant patterns with the observed pattern by using the simple least squares method and using the cooling rate data for the Ryoke belt proposed by Okudaira et al. (2001). The comparison between modeled and observed data suggests that the studied micro-shear zone was deformed for 16500–8400 yr under a deformation temperature of 550 °C and a differential stress of 90 ± 10 MPa, followed by post-deformation cooling at a rate of 40–70 °C/Myr. The shear strain of the shear zone was calculated by multiplying the deformation duration by the shear strain rate estimated from the dislocation-creep flow law of quartz, yielding a value of 50–260.

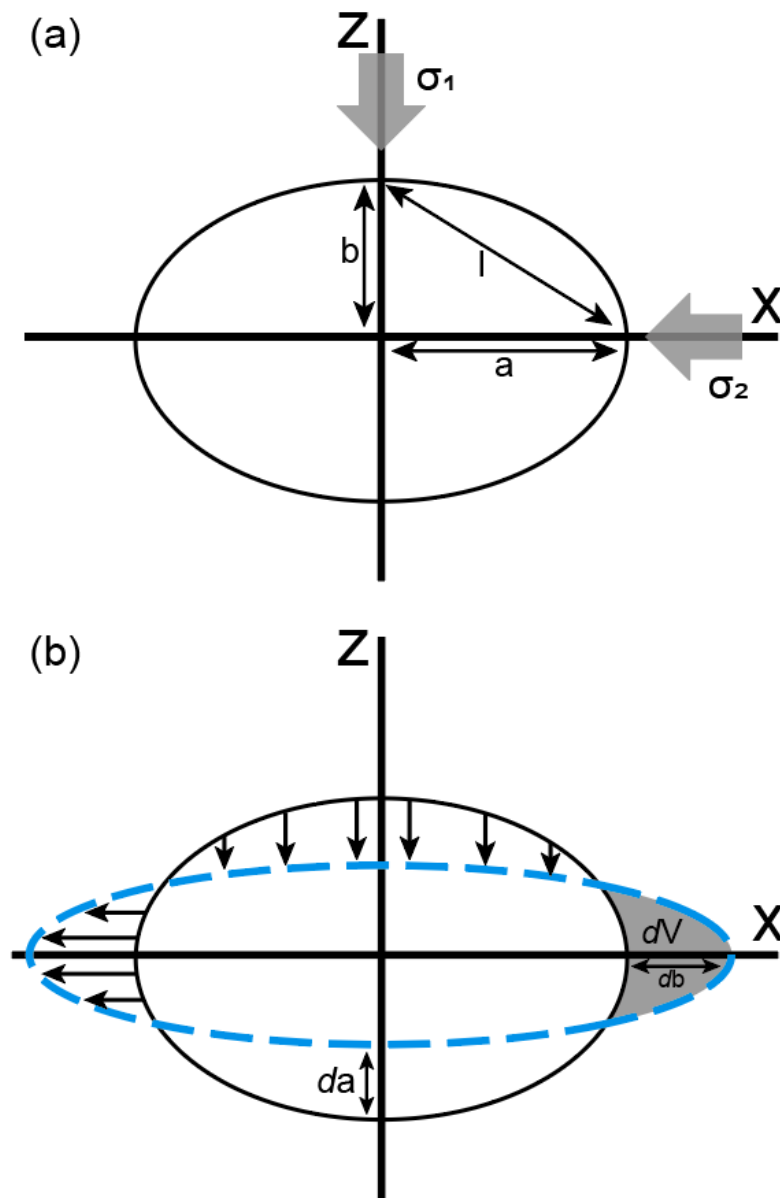


Figure 1. (a) Shape of an inclusion under a stress condition of $\sigma_1 > \sigma_2$. The long axis of the inclusion is denoted by “ a ” and the short axis by “ b ”, and the mean distance between the two axes is denoted by “ l ”. (b) Shape of an inclusion after deformation (dashed blue line). The volume of material transported by diffusion is depicted by the shaded area.

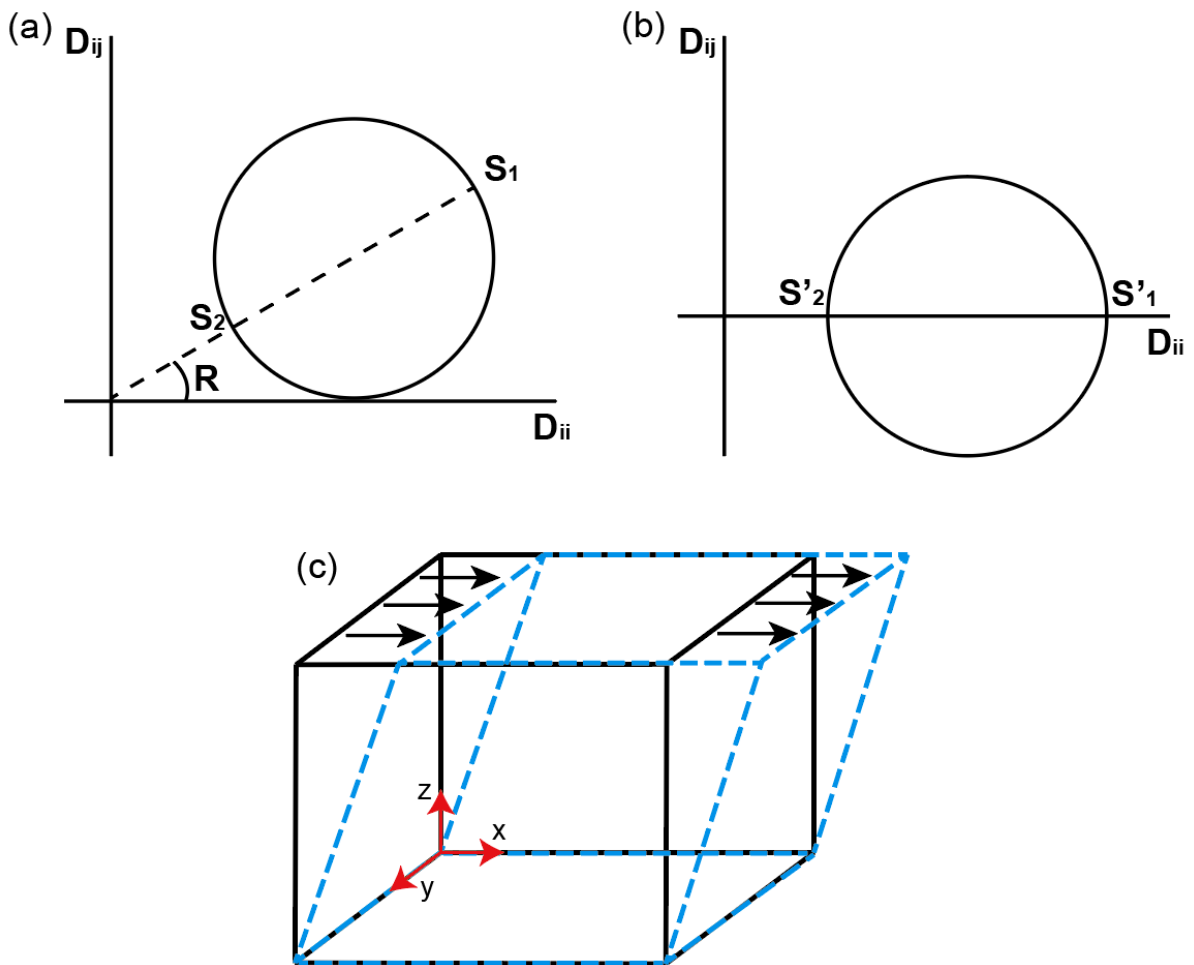


Figure 2. (a) Mohr circle for the deformation gradient tensor of 2D simple shear. S_1 and S_2 are principal stretch axes. (b) Mohr circle formed by removing the rotation component from the Mohr circle of (a) by rotating clockwise by an angle R . The shape of the Mohr circle in (b) is the same as that of the Mohr circle of pure shear. S'_1 and S'_2 are the principal stretch axes of the Mohr circle in (b). (c) Schematic figure showing simple shear in three dimensions. Deformation occurs only on the X-Z plane (b-plane).

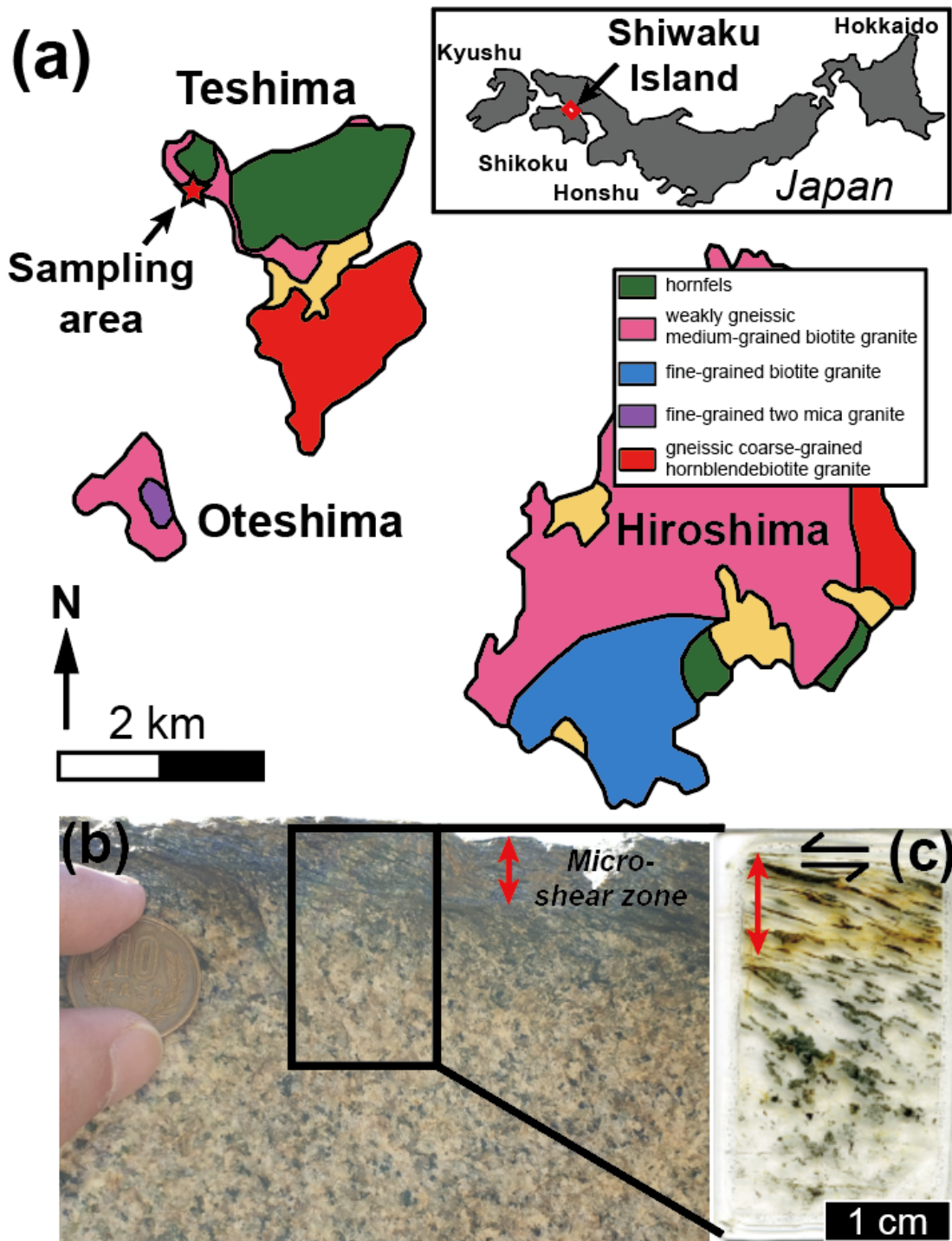


Figure 3. (a) Geological map of the Shiwaku Islands, including Teshima Island, modified from Michibayashi and Murakami (2007). Teshima Island is composed of weakly gneissic biotite granite and hornfels in the northern part, and gneissic hornblende biotite granite in the southern part. The sampling area is a micro-shear zone within weakly gneissic biotite granite in the northwestern part of the island. (b) Outcrop photograph of the micro-shear zone, which is developed as a 1–2 cm wide layer at the top of the outcrop. The black line represents the position of the thin section shown in (c). (c) Photomicrograph of the obtained thin section in plane-polarized light. The foliation is gradually rotated toward the micro-shear plane with decreasing distance from it. The rotation of foliation represents a sinistral sense of shear.

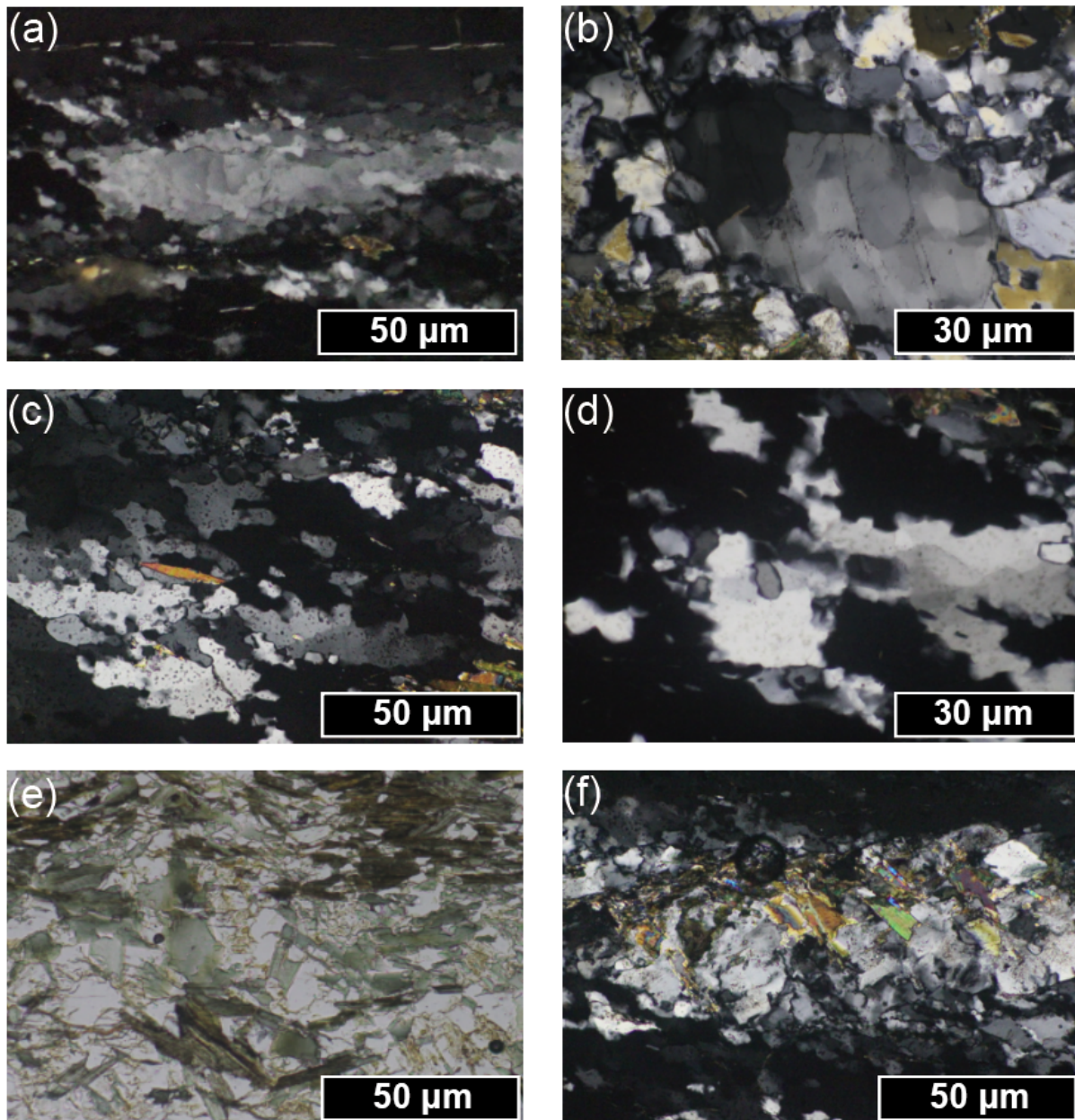


Figure 4. Microstructures of the micro-shear zone sample. (a) and (b) Optical photomicrographs (XPL) showing subgrain rotation (SGR) recrystallization structures of quartz grains. Relict quartz grains are surrounded by recrystallized grains exhibiting similar size with subgrains. (c) and (d) Optical photomicrographs (XPL) representing grain boundary migration (GBM) recrystallization structures of quartz grains. Grain boundaries are lobate and show migration structures. (e) and (f) Optical photomicrographs (e, PPL; f, XPL) showing deformed K-feldspars overprinted by relatively strain-free muscovite and biotite grains formed during the breakdown of K-feldspar. Deformation structures of K-feldspar cannot be clearly identified owing to the presence of overprinting grains.

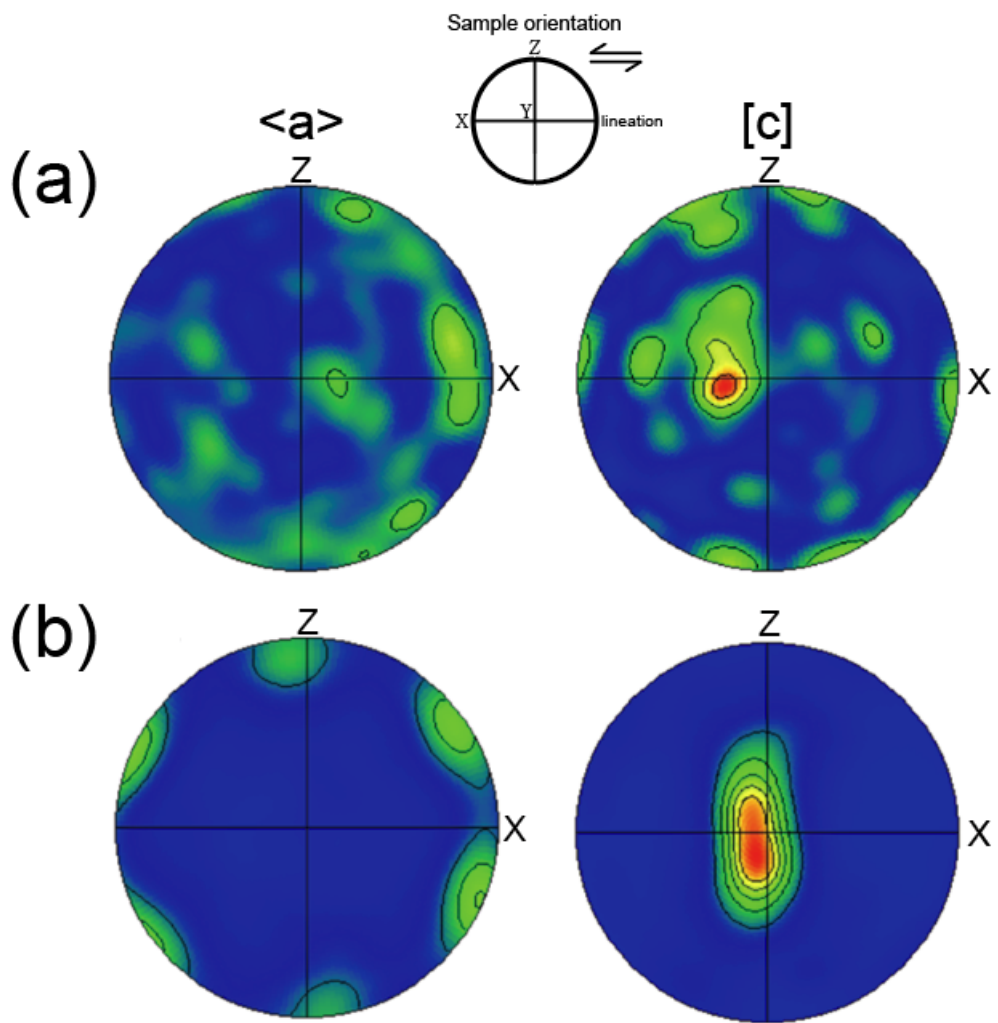


Figure 5. CPOs of quartz grains in the sample. Equal-area lower hemisphere projection. (a) Projections for the wall rock within the sample. (b) Projections for the micro-shear zone within the sample. Foliation is the X-Z plane, and the lineation is a solid line (X) on the foliation.

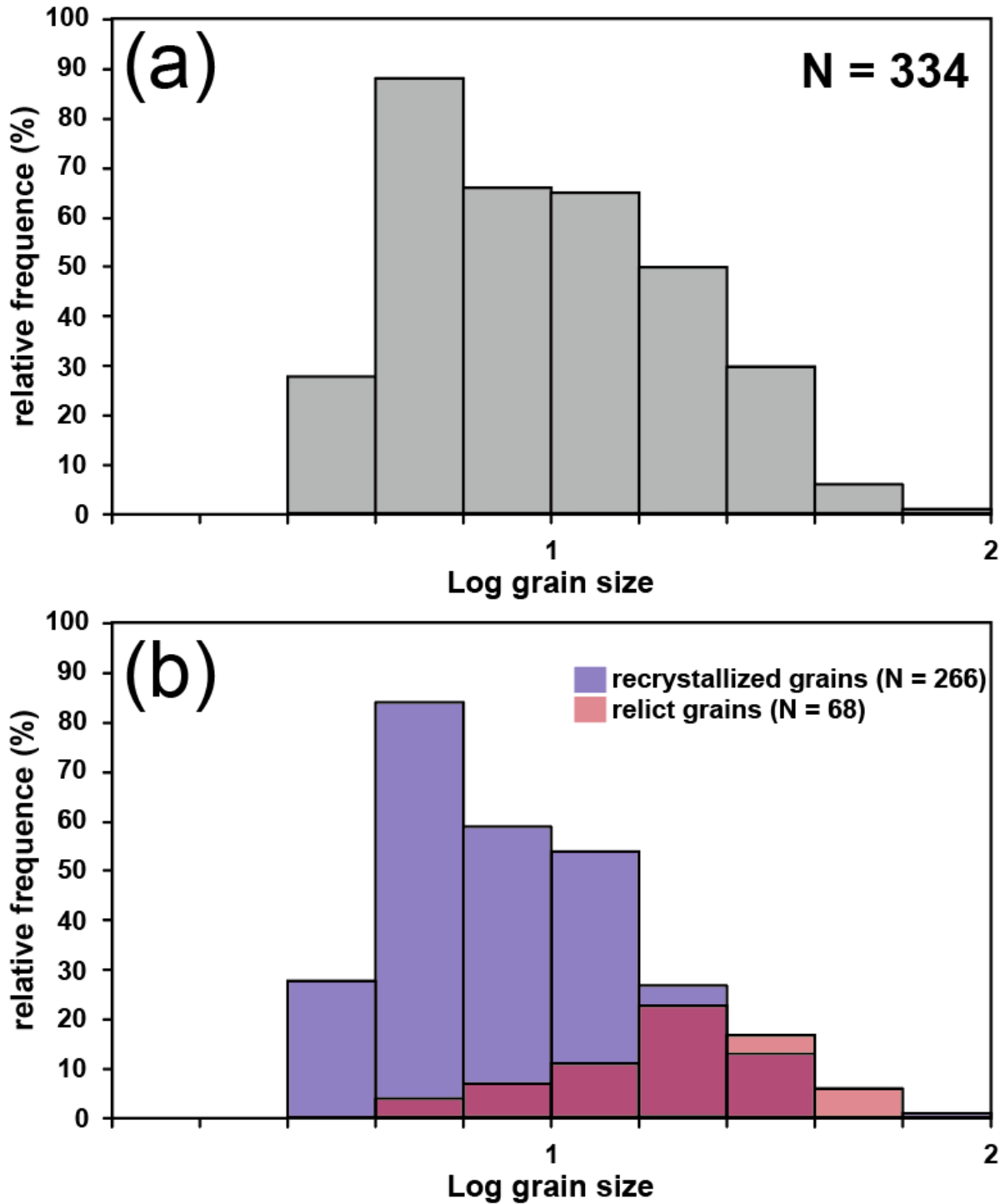


Figure 6. Logarithmic grain size distributions for quartz grains in the micro-shear zone. (a) Grain size distribution for whole grains including both recrystallized and relict grains. (b) Grain size distribution separated into recrystallized and relict grains.

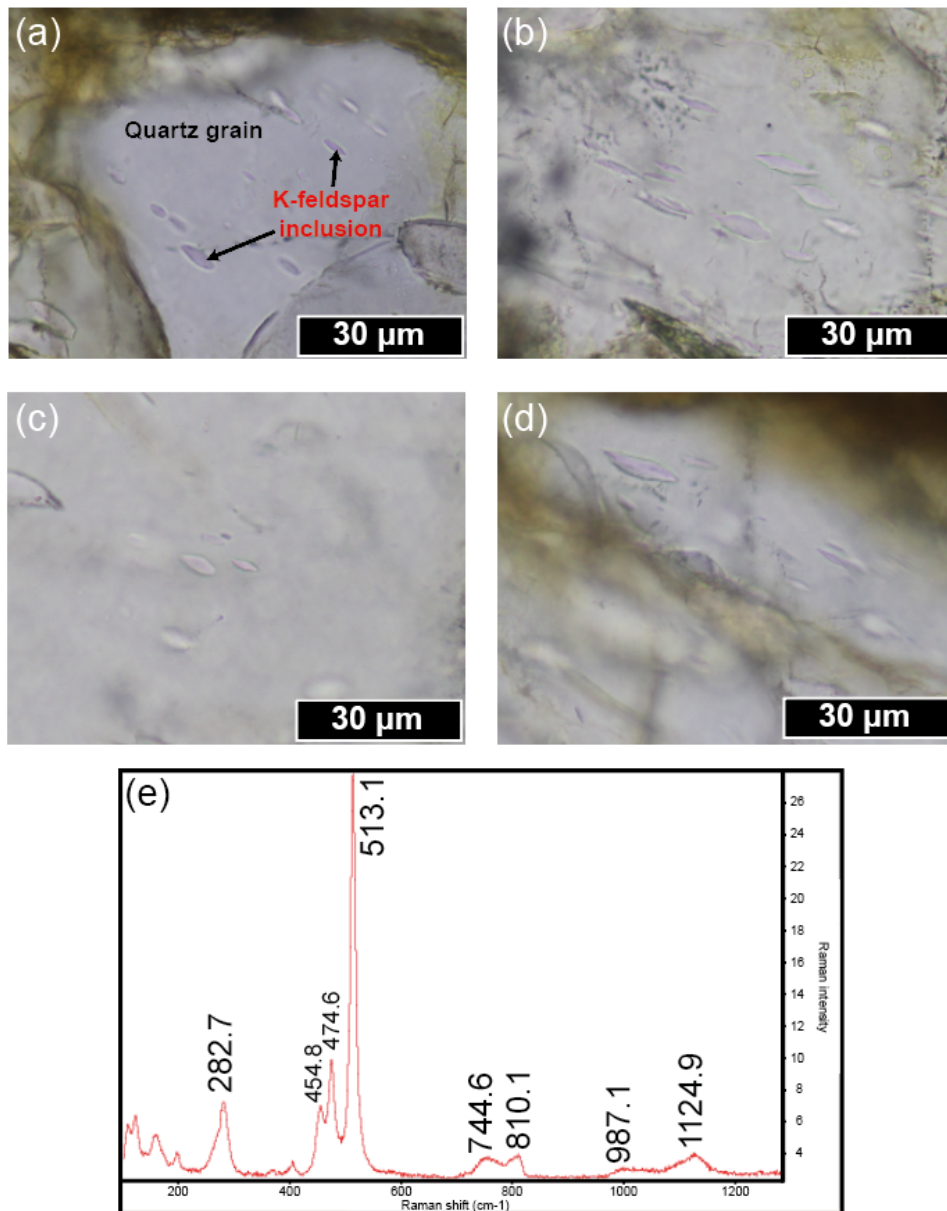


Figure 7. (a–d) Photomicrographs (PPL) showing K-feldspar inclusions within host quartz grains in the micro-shear zone. Pinkish, elongated grains are K-feldspar inclusions, and the background is the host quartz grain. (e) Raman spectra of K-feldspar inclusions. The values of the Raman shift at various peaks are consistent with those of K-rich alkali feldspar as estimated by Freeman et al. (2008).

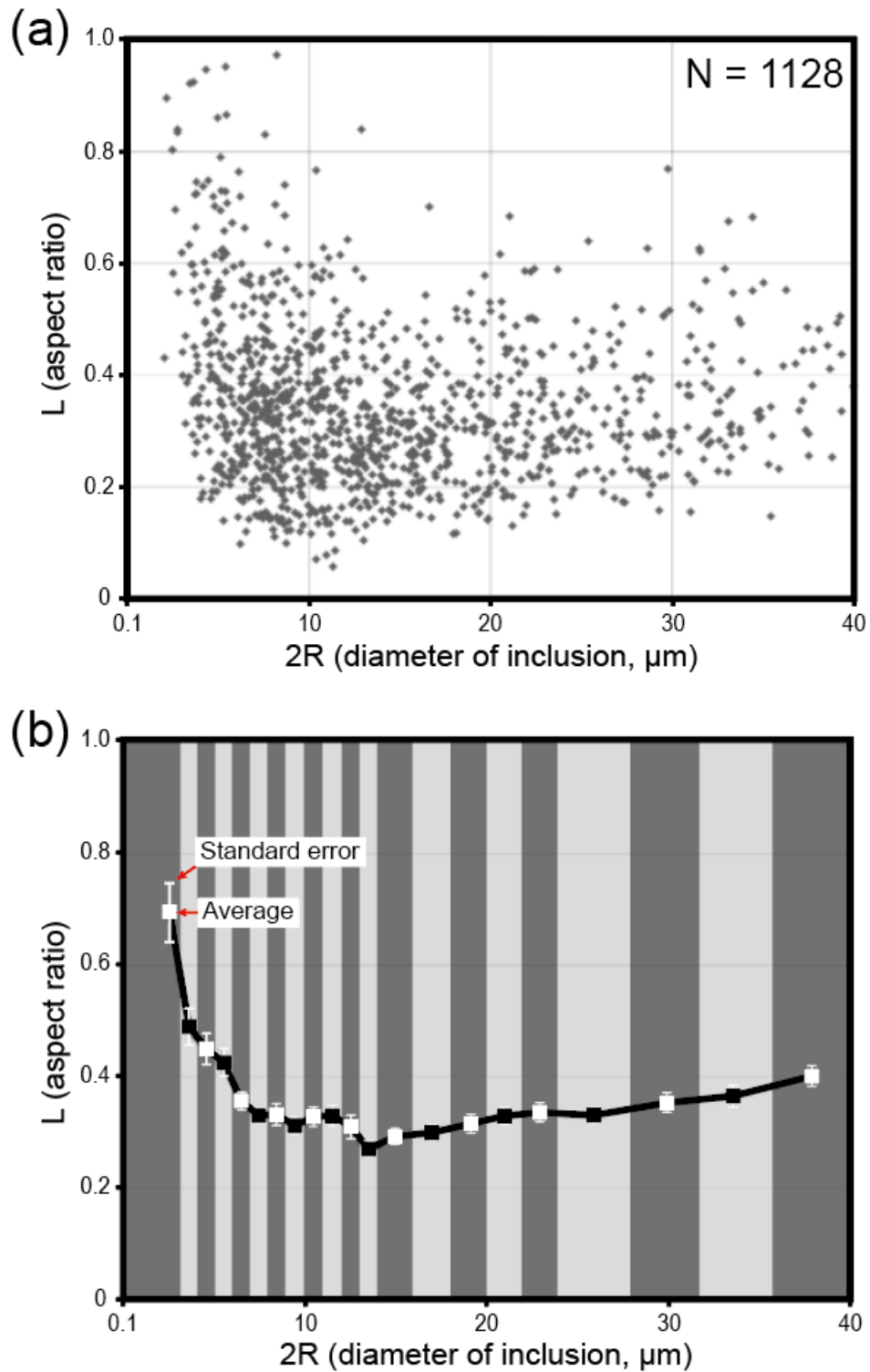


Figure 8. (a) Scatterplot of aspect ratio (L) versus inclusion diameter ($2R$) for the studied K-feldspar inclusions. (b) Mean aspect ratio of K-feldspar inclusions for 21 bins of diameter ($2R = 0.1-3, 3-4, 4-5, 5-6, 6-7, 7-8, 8-9, 9-10, 10-11, 11-12, 12-13, 13-14, 14-16, 16-18, 18-20, 20-22, 22-24, 24-28, 28-32, 32-36, \text{ and } 36-40 \mu\text{m}$). Each bar is the standard error of the mean aspect ratio calculated for each bin.

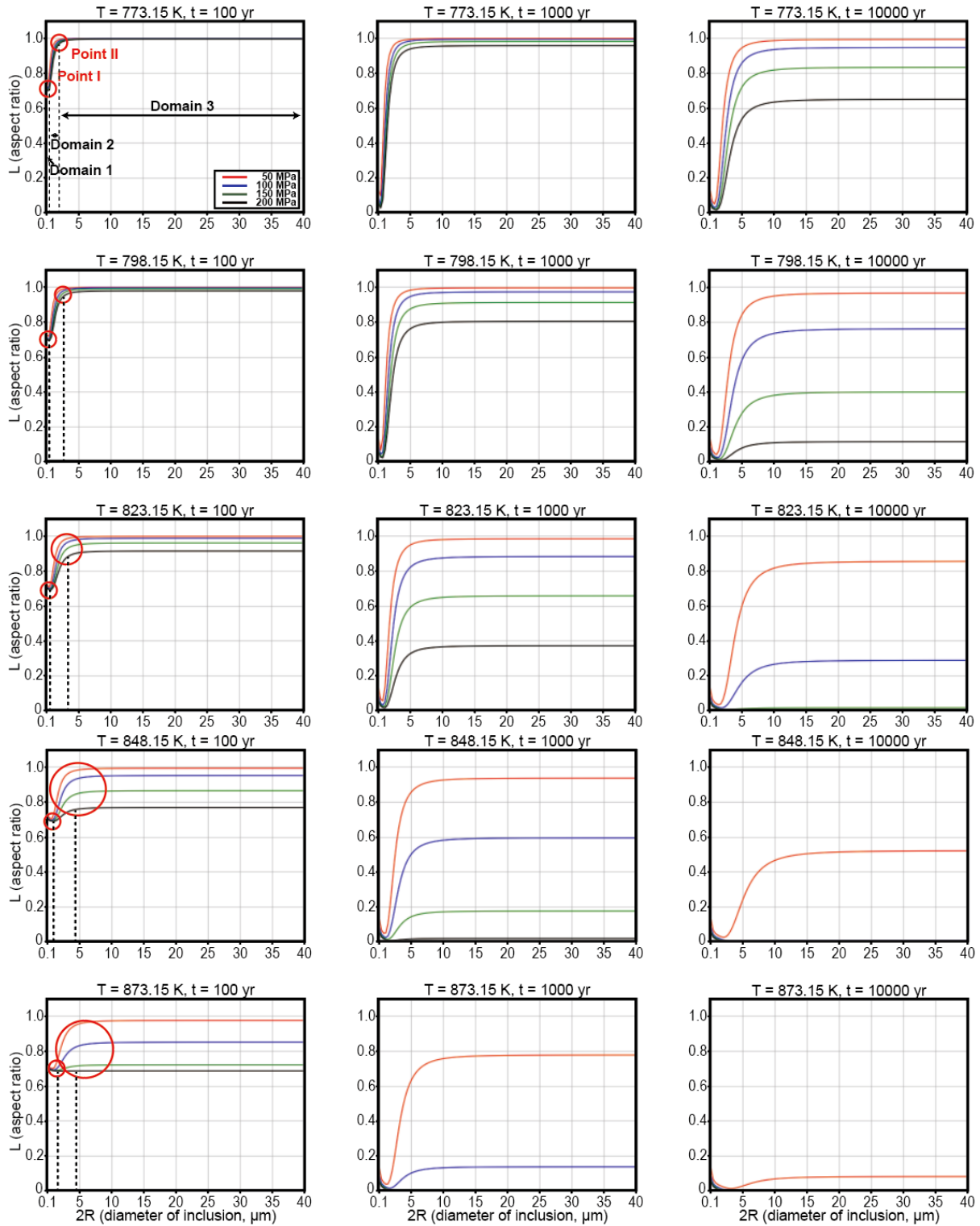


Figure 9. Shape-change patterns of K-feldspar inclusions for various deformation conditions; i.e., differential stress (σ), temperature (T), and deformation duration (t). L is aspect ratio, and $2R$ is the diameter of inclusions. The red, blue, green, and black lines show the cases for differential stress values of 50, 100, 150, and 200 MPa, respectively. Points I and II are marked as red circles. Domains 1, 2, and 3 are separated by dotted black lines.

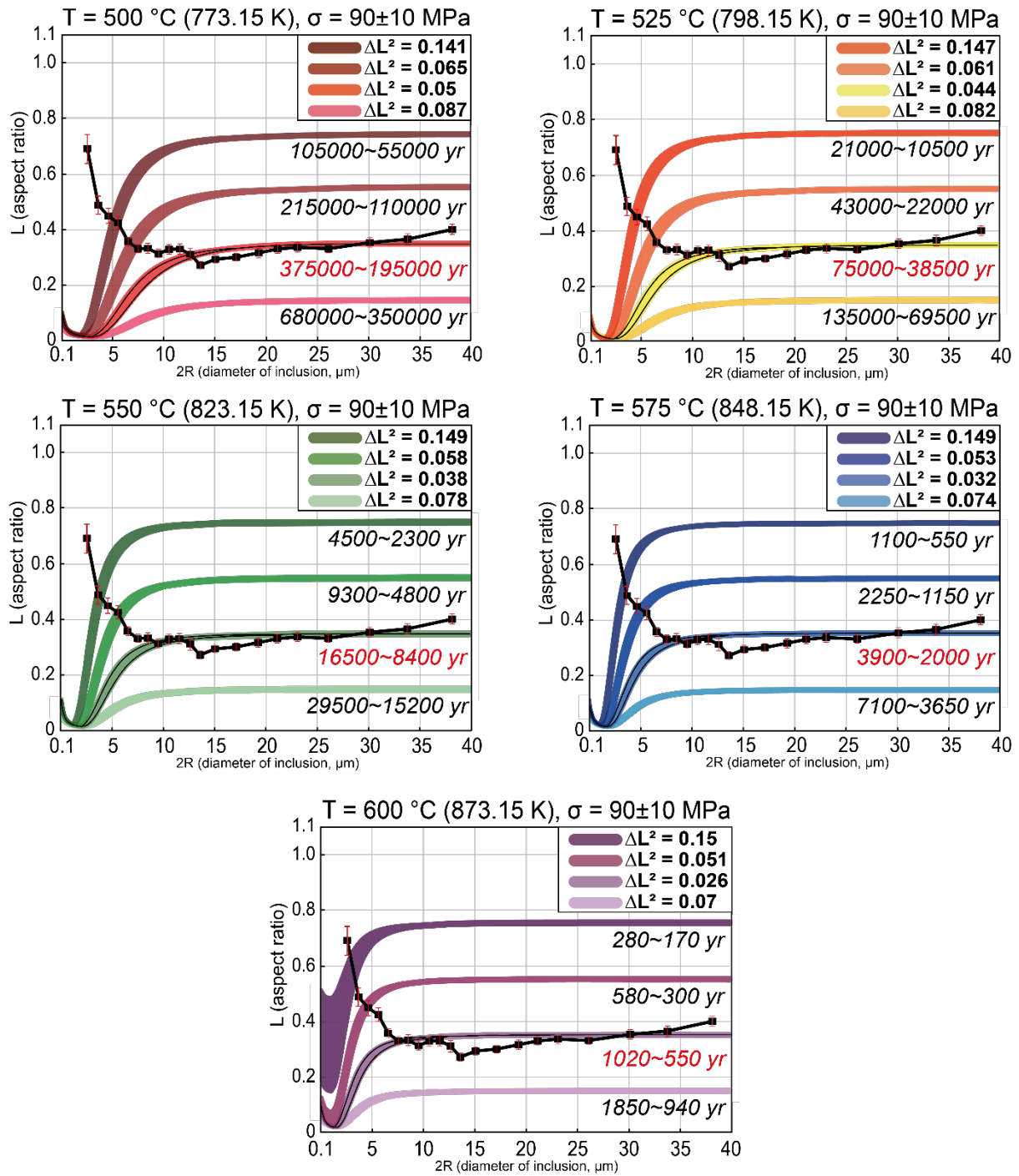


Figure 10. Progressive shape-change patterns calculated from the deformation model compared with the shape-change patterns (bold black lines) of the observed K-feldspar inclusions for different deformation conditions. The values of ΔL^2 are shown. Colored patterns represent the modeled $L-2R$ patterns that best match the observed shape-change patterns. The ranges of deformation duration are shown below each line. Deformation durations marked in red represent the deformation duration of the best-matching $L-2R$ pattern for each case.

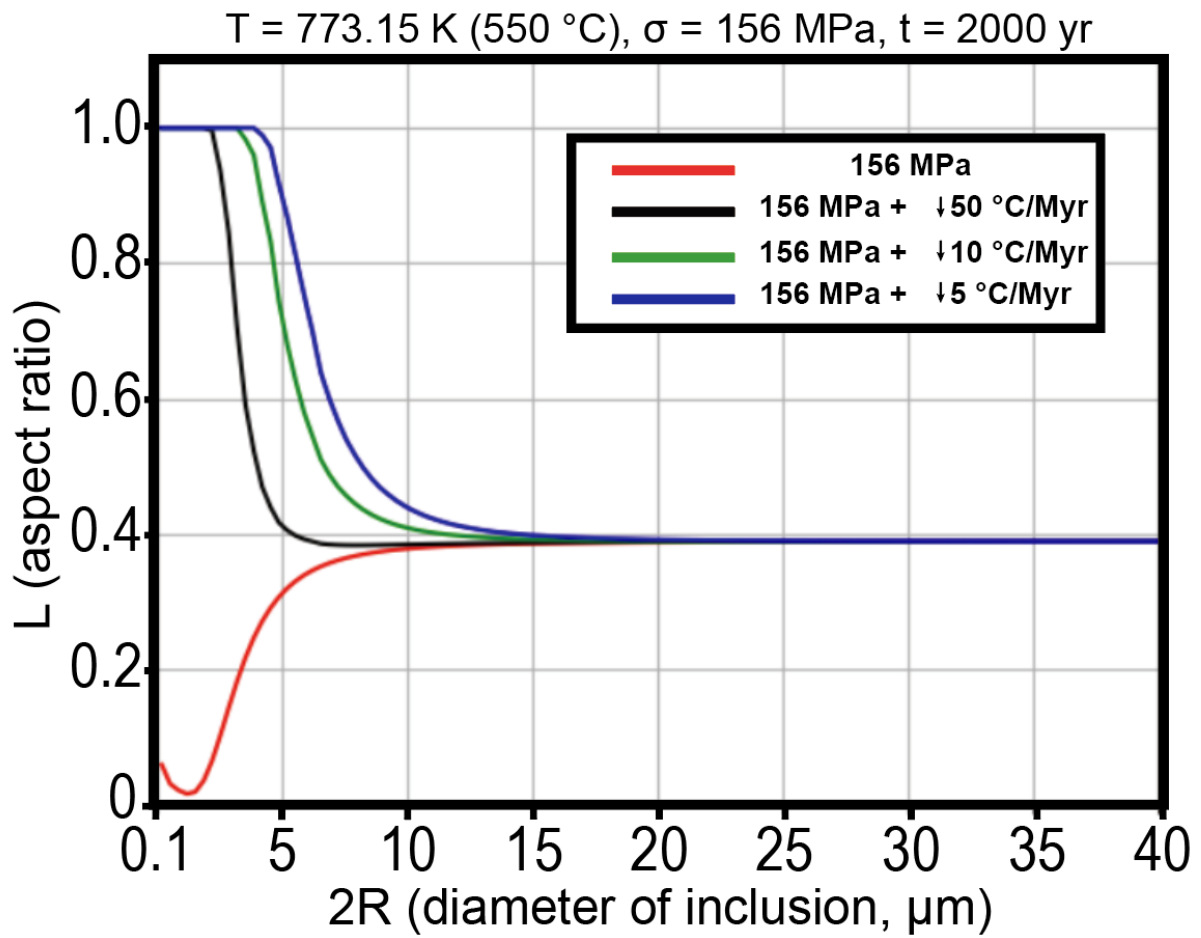


Figure 11. Representative data showing the effects of post-deformation annealing on inclusion aspect ratio and diameter. The red line is the shape-change pattern considering only deformation. Black, green, and blue lines are shape-change patterns considering the effects of post-deformation annealing with different cooling rates.

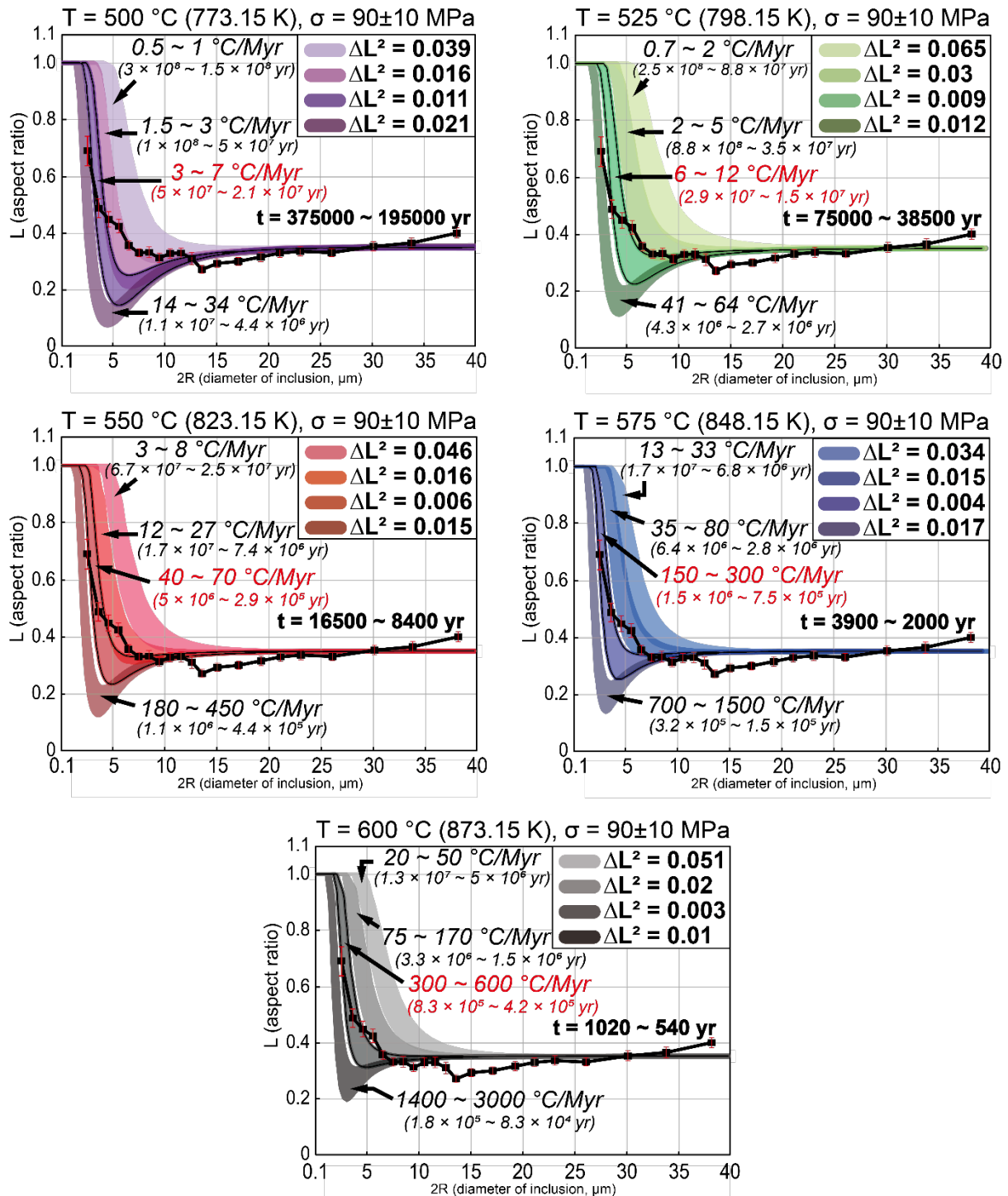


Figure 12. Shape-change patterns considering the effects of post-deformation annealing for different deformation conditions and cooling rate. Bold black lines represent the shape-change pattern of the observed K-feldspar inclusions for each sample. Colored patterns outlined by narrow lines represent the modeled $L-2R$ patterns that best match the observed shape-change patterns. The calculated values of ΔL^2 are shown. The ranges of cooling rate and cooling duration are shown next to the patterns. Cooling rates and durations of the best-matching patterns are marked in red. The ranges of deformation duration are displayed as t for each case.

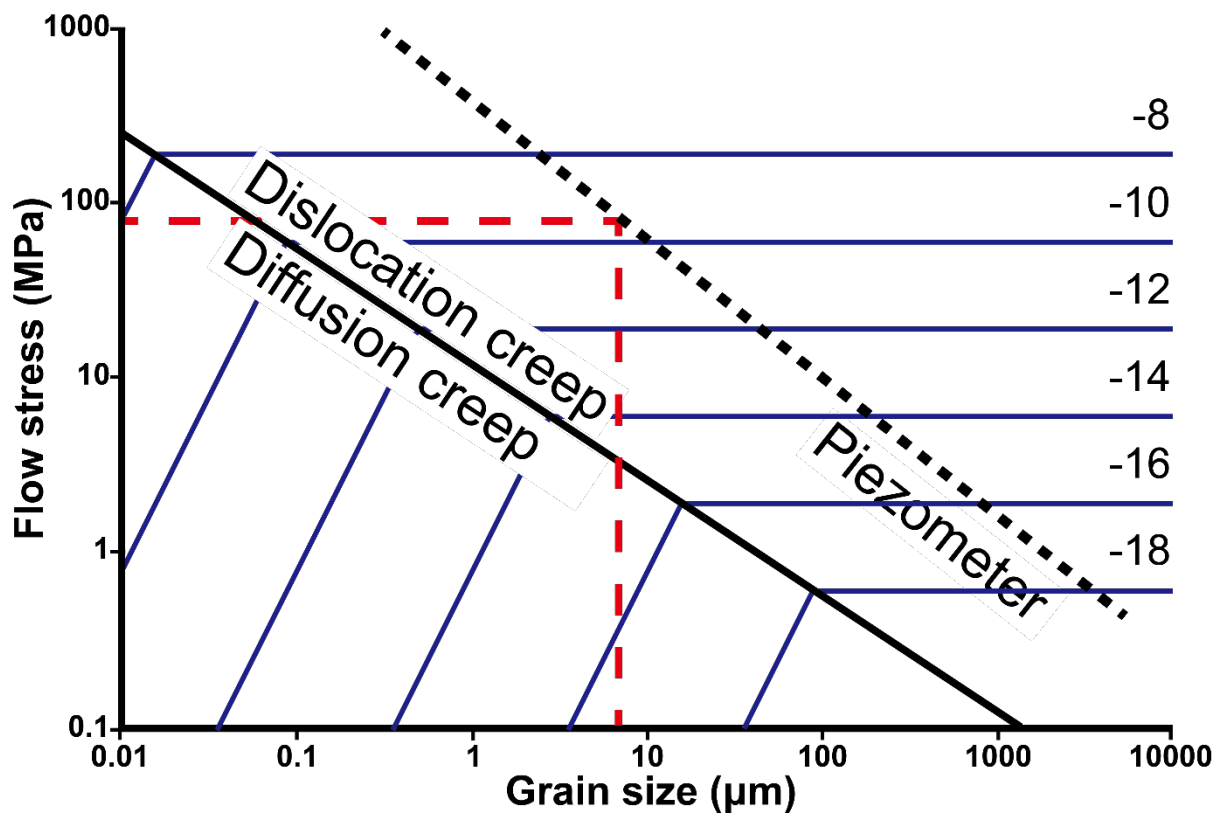


Figure 13. Deformation mechanism map of quartz within the micro-shear zone for temperatures of 550 °C. Boundaries of deformation mechanisms are defined by the dislocation-creep flow law of Hirth et al. (2001) and the diffusion-creep flow law of Brodie and Rutter (2000). Green and blue lines are contours of log shear strain rate. Paleo-stress (dashed red line) was estimated using the piezometer (dashed black line) of Stipp and Tullis (2003).

Table 1. Average aspect ratio of the K-feldspar inclusions in 21 ranges of diameter

| 2R (μm) | N | R _a (μm) | L _a | SD | SE |
|----------------------|----|----------------------------------|----------------|------|-------|
| 0.1 ~ 3 | 9 | 2.55 | 0.7 | 0.16 | 0.053 |
| 3 ~ 4 | 31 | 3.6 | 0.49 | 0.18 | 0.033 |
| 4 ~ 5 | 47 | 4.56 | 0.45 | 0.19 | 0.027 |
| 5 ~ 6 | 61 | 5.39 | 0.43 | 0.19 | 0.024 |
| 6 ~ 7 | 77 | 6.52 | 0.36 | 0.14 | 0.016 |
| 7 ~ 8 | 83 | 7.53 | 0.33 | 0.13 | 0.014 |
| 8 ~ 9 | 78 | 8.46 | 0.33 | 0.16 | 0.019 |
| 9 ~ 10 | 54 | 9.47 | 0.31 | 0.12 | 0.016 |
| 10 ~ 11 | 73 | 10.5 | 0.33 | 0.15 | 0.017 |
| 11 ~ 12 | 48 | 11.52 | 0.33 | 0.13 | 0.018 |
| 12 ~ 13 | 49 | 12.54 | 0.31 | 0.15 | 0.021 |
| 13 ~ 14 | 48 | 13.49 | 0.27 | 0.08 | 0.012 |
| 14 ~ 16 | 73 | 14.96 | 0.29 | 0.09 | 0.01 |
| 16 ~ 18 | 66 | 16.84 | 0.3 | 0.1 | 0.013 |
| 18 ~ 20 | 57 | 19.15 | 0.32 | 0.12 | 0.016 |
| 20 ~ 22 | 57 | 21.02 | 0.33 | 0.12 | 0.016 |
| 22 ~ 24 | 42 | 22.97 | 0.34 | 0.11 | 0.017 |
| 24 ~ 28 | 58 | 25.97 | 0.33 | 0.1 | 0.013 |
| 28 ~ 32 | 56 | 29.97 | 0.36 | 0.14 | 0.018 |
| 32 ~ 36 | 40 | 33.64 | 0.37 | 0.12 | 0.02 |
| 36 ~ 40 | 21 | 37.95 | 0.4 | 0.08 | 0.018 |

2R = diameter of inclusions, N = number of inclusions, R_a = average diameter of inclusions, L_a = average aspect ratio of inclusions, SD = standard deviation of aspect ratio, SE = standard error of aspect ratio

Table 2. Parameters of the deformation model

| | | |
|----------|---|-------------------------------|
| L | Aspect ratio of inclusion | |
| R | Inclusion size (radii of inclusion, m) | |
| D_{gb} | Interface diffusion coefficient (m^2/s) | |
| T | Time (s) | |
| σ | Differential stress ($\sigma_1 - \sigma_2$, Pa) | |
| δ | Width of inclusion boundary (m) | $2.0 \sim 3.0 \times 10^{-9}$ |
| Ω | Volume of a vacancy (m^3) | 3.8×10^{-29} |
| γ | Interfacial tension (N/m) | 0.22 |
| k | Boltzman' constant (J/K) | 1.38×10^{-23} |
| T | Temperature (K) | |
| C | Constant | 4.83 |
| n | Stress exponent ^a | 3 |
| Q | Constant (kJ/mol) ^a | 332 ± 23 |
| A | Constant (Mpa^{-n}/s) ^a | $10^{3.4 \pm 1.0}$ |

^aValue from Offerhaus et al. (2002)

Table 3. Interphase diffusion rate ($D_{gb}\delta$) of potassium and silicon in K-feldpsar/Quartz aggregates. Silicon interphase diffusion rate is the value of potassium interphase diffusion multiplied by 2×10^{-6} .

| T (°C) | ^b Interphase diffusion rate of potassium (K) in K-feldpsar/Quartz aggregates ($D_{gb}\delta$, m ³ /s) | Interphase diffusion rate of silicon (Si) in K-feldpsar/Quartz aggregates ($D_{gb}\delta$, m ³ /s) |
|--------|---|---|
| 500 | 2.1318×10^{-24} | 4.2636×10^{-30} |
| 525 | 6.1633×10^{-24} | 1.2327×10^{-29} |
| 550 | 1.6710×10^{-23} | 3.3420×10^{-29} |
| 575 | 4.2721×10^{-23} | 8.5442×10^{-29} |
| 600 | 1.0350×10^{-22} | 2.0700×10^{-28} |

^bExtrapolated data from Farver and Yund (1995)

Part 2:

Relationships between intensity of deformation induced Cr-Al chemical zoning and geometrical properties of spinel: An approach applying machine learning analysis

Abstract

Chemical zoning of mineral, which commonly used as evidences for interpreting cooling processes of magma, and reaction path of metamorphic rocks, results from incomplete chemical reaction or slow diffusion kinetics. However, Ozawa [1989] firstly reported Cr-Al chemical zoning of elongated spinel derived by deformation (lattice diffusion) from natural deformed peridotites. More recently, Suzuki et al. [2008] elucidated the processes of lattice diffusion induced Cr-Al chemical zoning of spinel by estimating self-diffusion coefficients of Cr and Al. In this study, I present relationships between intensity of the Cr-Al chemical zoning and geometrical properties of spinel grains within a dunite sample in the Transition Zone in the Horoman peridotite complex in Hokkaido, northern Japan, by using machine learning analysis. Given the analyzed result, I discuss connections between the relationships and deformation mechanisms of spinel and estimate deformation temperature. To analyze intensity of the Cr-Al chemical distributions within each spinel grain, I estimate chemical distribution of Cr for 87 spinel grains within the dunite sample by using SEM-EDS line scanning. For applying the estimated data to the machine learning algorithms, the following sequence is applied: 1) analyzing chemical zoning, 2) data pre-processing, 3) data clustering, 4) data splitting, 5) classification and node analysis, 6) estimating feature importance. As analyzing result, the spinel grains are clustered as three groups in accordance with intensity of the chemical zoning. The intensity is more importantly affected by grain size than aspect ratio of the spinel grain and is much greater with increasing grain size. Given diffusion flux ratio (R_{diff}) of the spinel grains, these results reflect that lattice diffusion is much actively contributed to total diffusion creep of spinel than grain boundary diffusion with increasing grain size.

Deformation temperature of spinel is estimated by comparing the R_{diff} suggested by Swaroop et al. (2005) and Shibutani et al. (1998) and the R_{diff} of the spinel grains as 1250-1100 °C.

1. Introduction

Chemical zoning is chemical disequilibrium feature that observed from various mineral species within igneous and metamorphic rocks (Hollister, 1970; Loomis, 1976; Tracy and McClellan, 1985; Hickmott and Shimizu, 1990; Allaby, 2013). Chemical zoning is commonly originated by incomplete chemical reaction to keep their chemical equilibrium with magma or slow diffusion kinetics of cation inhibiting chemical homogenization during metamorphism or change in the chemical reaction environment (Vance, 1965; Nakamura, 1973; Loomis, 1983; Hickmott et al., 1987; Chakraborty and Ganguly, 1991; Hoskin and Schaltegger, 2003). Given the characteristics of chemical zoning, the chemical zoning generally used as evidences for interpreting reaction history of metamorphic rocks and cooling processes of magma, etc (Vance, 1965; Nakamura, 1973; Loomis, 1983; Hickmott et al., 1987; Chakraborty and Ganguly, 1991; Hoskin and Schaltegger, 2003).

Ozawa (1989) firstly reported that the chemical zoning can be derived by deformation (lattice diffusion) from Cr-Al chemical zoning of elongated spinel grains in natural deformed peridotites, suggesting a model that the chemical zoning induced by diffusion creep is derived by a difference of diffusivity between Cr and Al during deformation. Suzuki et al. (2008) introduced that detailed processes of lattice diffusion induced the Cr-Al chemical zoning of spinel grains by measuring self-diffusion coefficients of Cr and Al from Cr-Al interdiffusion experiment. However, no studies have analyzed and interpreted chemical characteristics of the Cr-Al chemical zoning in accordance with geometrical properties (size and aspect ratio) of spinel grains.

In this study, I firstly investigate diverse chemical features of the Cr-Al chemical zoning observed from spinel grains within a dunite sample by using EPMA analysis. I then analyze relationships between the Cr-Al chemical zoning and geometrical properties of spinel grains by using machine learning algorithms. Considering the analyzed data, I interpret connections between the

analyzed relationships and deformation mechanisms of spinel grains and estimate deformation temperature of the dunite sample.

2. Characteristics of Cr-Al chemical zoning in spinel grains

2.1 Sample description

The analyzed spinel grains were collected from a dunite sample located in the dunite layer within the Transition Zone between the Upper and Lower Zone in the Horoman peridotite complex in Hokkaido, northern Japan (Niida, 1974; Ozawa and Takahashi, 1995; Takazawa et al., 1999; Ozawa, 2004; Takahashi, 2004; Sawaguchi, 2004; Malaviarachchi et al., 2008; Malaviarachchi et al., 2010; Yoshikawa et al., 2019) (Fig. 1a-b). The dunite sample involved a lineation characterized by a linear arrangement of elongated spinel grains on a foliation defined by grain shape preferred orientation of olivine and diopside. A thin section cuts perpendicular to the foliation and parallel to the lineation since the chemical zoning is expected to develop along elongated orientation of spinel grains. The thin section is analyzed by using a scanning electron microscope (SEM) equipped with electron backscatter diffraction (EBSD) equipment (HITACHI S-3400N Type II with HKL Channel5) at Nagoya University, Nagoya, Japan. Analyzing conditions are an accelerating voltage of 20 kV, working distance of 28 mm, sample tilt of 70°, and low-vacuum mode of 30 Pa. EBSD data are collected by large area mapping with a step size of 10 μm that is about 10 times smaller than the average grain size. The sample consists mainly of olivine with minor spinel and diopside (Fig. 1c-d). Grain size of olivine is coarse in a range about 100-2000 μm . Grain boundaries are interlobate and locally straight. Olivine grains show grain shape preferred orientation with sweeping undulose extinction and deformation band. Spinel grains exhibit various grain size range from 20 to 2200 μm . Spinel grains are elongated parallel to the preferred orientation of olivine grains with various aspect ratio. Figure 2 presents CPOs of olivine grains from the thin section. The structural framework of CPOs is characterized by the lineation (X) and the foliation normal (Z). The CPOs are plotted by using one point per grain onto lower-hemisphere equal-area projection. The CPO patterns show that the [100] axes are parallel to the X, and the [010] axes are

normal to the foliation, suggesting A-type of olivine crystal-fabric. These microstructures indicate that olivine grains were deformed by plastic deformation with spinel grain.

2.2 Cr-Al chemical zoning

The Cr and Al chemical distribution in spinel grains is investigated by both area mapping and point analysis of an electron-probe microanalyzer (EPMA, JEOL JXA-8800R) at the Nagoya University for representative spinel grains with 100 nA and 12 nA beam current and 20 kV and 15 kV of accelerating voltage, respectively. Area mapping is operated with a 1 μm of step size for spinel grains. In area mapping data for spinel grains showing Cr-Al chemical zoning, distributions of Cr are identified by greatest concentration at both of tip areas of short axis of spinel and lowest concentration at both of tip areas of long axis of spinel (Fig. 3a). Distributions of Al are characterized by reverse relationship with the distributions of Cr. At center area of spinel, distributions of Cr and Al are distinguished as intermediate concentration. These characteristics are identical with the features of multipolar Cr-Al chemical zoning reported by Ozawa (1989) (Fig. 4). Although most of spinel grains exhibit ellipsoidal shape with preferred orientation of long axes, spinel grain shows each different concentrations of Cr and Al between at center area and both of tip areas (Fig. 3). In this study, I nominated degree of the difference for Cr and Al concentrations as intensity of Cr-Al chemical zoning. Figure 3 and Table 1 display representative three spinel samples exhibiting different intensity of Cr-Al chemical zoning. S1 is a spinel grain having strong intensity of Cr-Al zoning and the gaps of compositions between P1 and P2 are 4.038 wt% for Cr and 3.773 wt% for Al. S2 shows relatively weak intensity of Cr-Al zoning and the differences of compositions between P4 and P5 are smaller than the gaps of S1 as 1.16 wt% for Cr and 1.308 wt% for Al. Some spinel grains even have homogeneous chemical distribution like S3. The differences of compositions of Cr and Al between P7 and P8 of S3 are 0.263 wt% and 0.064 wt%, respectively. Spinel grains showing high intensity of Cr-Al zoning exhibit high differences of wt% for Cr and Al at between center area and both of tip areas. There are no typical differences for other grains having homogenous chemical distribution. These chemical distributions of Cr and Al suggest that the gap of Cr and Al distributions at between center area and both of tip areas reflects intensity of Cr-Al

chemical zoning and there are differences in the intensity of Cr-Al chemical zoning for each spinel grain.

2.3 Intensity of Cr-Al chemical zoning

To assess the intensity of Cr-Al chemical zoning for each spinel grain, I estimated chemical distributions of Cr and Al for each spinel grain by using EDS. EDS data are collected by using line scanning with an accelerating voltage of 20 kV, working distance of 28 mm, and low-vacuum mode of 30 Pa. Given the inverse relationship of chemical distribution between Cr and Al, I measured EDS data for only Cr to simplify analyzing data. The line scanning is conducted along the long axis of each spinel grain from its margin to the other margin (Fig. 5). To determine the intensity of Cr-Al zoning as numerical values, I analyzed 87 spinel grains showing various geometrical properties. The analyzed data are exported by files in CSV format for each spinel grain. Each data consists of 200 values reflecting chemical distribution of Cr. The values are listed in the order from the starting point to the end point of a line scanning with outliers. To correct the values by sorting outliers, static outlier identification method is applied by using Interquartile range (IQR) (Yang et al., 2019). IQR is defined by the difference between the values of 75% (Q_3) and 25% (Q_1) of data.

$$IQR = Q_3 - Q_1$$

Outliers are the values above $Q_3 + 1.5 \times IQR$ (maximum) or under $Q_1 - 1.5 \times IQR$ (minimum). The method is applied to the values of each spinel grain and the sorted outliers are replaced by the average for each spinel data. The corrected values are divided into five equal parts from A to E and calculated average values for each of the part. The average values for A, E, and C parts indicate average values of Cr at the margin (starting point) area, the other margin (end point) area, and the center area, respectively. The intensity of Cr-Al zoning is expressed by calculating differences of the average values between C and A (ΔCA), and C and E parts (ΔCE) (Fig. 5). The intensity is much higher as the differences is higher.

2.4 Geometrical properties

Geometrical properties (grain size and aspect ratio) of spinel grains are analyzed by utilizing

image analysis software ImageJ. Grain boundaries of spinel grains are traced from optical photomicrographs. The geometrical properties are estimated from best-fit ellipses of the tracing grain boundaries computed by ImageJ software.

3. Methods of machine learning analysis

3.1 Machine learning framework

Given a way to using data, machine learning method is divided into unsupervised machine learning method that learns patterns in feature data without label data, and supervised machine learning method that learns functions or relationships between feature and label data considering examples of feature and label data. To estimate relationship between the intensity of Cr-Al chemical zoning and geometrical properties of spinel grains, I used Mean-shift clustering (MCA), that is unsupervised machine learning method, and Decision Tree and Random Forest, that are supervised machine learning method. I converted the values representing the intensity of Cr-Al zoning (ΔCA , ΔCE) to standardized values. The standardized values for each spinel grain are projected as data points in a scatterplot. The MCA is utilized to define clustering patterns of the data points. The data points are set as featuring data for applying to the machine learning method and the defined types of clusters are established as label data for the feature data. The Decision Tree and Random Forest are used to recognize the relationship on the basis of the label and feature data. The detailed workflow to run machine learning is as follows: data pre-processing → data clustering → data splitting → classification and node analysis → estimating feature importance → constructing probability map.

3.2 Pre-processing

As a stage of pre-processing before machine learning analysis, data standardization is necessary to not only accelerate calculation of machine learning but also improve model accuracy (Hsu et al., 2003). The analyzed raw data show diversity in scale. The data standardization is used to transform the analyzed raw data into the format showing particular scale by normalizing the raw data. In this study, the data standardization is applied by using a “StandardScaler” algorithm (from Scikit-

learn in a Python library). The algorithm transforms original data showing variable scales into normalized data showing that mean value is zero and standard deviation is one. The normalized data are obtained by removing mean value to each original value and dividing by their standard deviation.

$$z = \frac{x - u}{s}$$

Where x , u and s are value, mean and standard deviation of original data and z is value of the normalized data.

3.3 Mean-shift Clustering

The Mean-shift Clustering (MCA) is a method that clusters data points considering locations of a maximum density of data points (Cheng, 1995; Tuzel, 2009; Zhang et al., 2018). The MCA is basically built on the principle of kernel density estimation (KDE) that is a method to calculate the probability density function of data. The KDE can be written as

$$f(x) = \frac{1}{nh} \sum_{i=1}^n K\left(\frac{x - x_i}{h}\right)$$

where $f(x)$ is density function for given point, x_i is the point for input data, K is Kernel function (Gaussian kernel), h is bandwidth. Since h is only variable parameter in the equation, the density function significantly depends on h .

The MCA is worked by shifting a point toward much denser point from random location as a starting point to find out a center point of the densest cluster of data points upon the density function, repeatedly calculating the mean coordinate of data points. Given the calculated the center points, the data points are clustered. Number of clusters for the data points can be changed with the predefined value of h since the MCA works on the density function. An advantage of the MCA is that unlike other clustering algorithms that need subjective decision of user to cluster data points or set up number of clusters, it can calculate the most optimal number of clusters by estimating the most suitable bandwidth for the data points. Therefore, I used a “MeanShift” algorithm to cluster points of the data and a “estimate bandwidth” to estimate the most optimal number of clusters.

3.4 Data splitting

Data splitting is one of stages that randomly divides data into train data sets and test data sets to estimate a performance of the model. The train data sets are used to train a model and a performance of the model is estimated by the test data sets. By using a “train test split” algorithm, all of the data in this study are split into train data sets and test data sets as 90% and 10% of volume size, respectively. Proportions of the label data are maintained while splitting the data sets.

3.5 Model assessment

To assess performances of the models, I evaluated accuracy, recall, precision, f1 score, and ROC-AUC score for each model. The accuracy is ratio of data sets correctly predicted from the trained model to test data sets. The accuracy is expressed by

$$Accuracy = \frac{TP + TN}{TP + FP + FN + TN}$$

where TP and FP are cases predicted positive and it is really true and false, respectively. TN and FN is cases predicted negative and it is actually true and false, respectively. The accuracy is maximum as 1.0 when number of correctly predicted data sets is equal with number of the test data sets. The recall and precision are defined by

$$recall = \frac{TP}{(FN + TP)}$$

$$precision = \frac{TP}{(FP + TP)}$$

$(FN + TP)$ means numbers of actual positive cases, and $(FP + TP)$ means numbers of cases predicted positive regardless of both true and false. The recall and precision show trade-off relationship. If score of the recall increase, score of the precision is decrease. To define the trade-off relationship, I also calculated $f1$ score. The $f1$ score, which indicates how much the recall and precision are skewed, is a harmonic mean combining the recall and precision and expressed by

$$f1 = 2 \times \frac{\textit{precision} \times \textit{recall}}{\textit{precision} + \textit{recall}}$$

The *f1* score has a relatively high value when the recall and precision is not biased to either side. Finally, the ROC-AUC score is calculated to estimate prediction performance of models. The ROC is curve that visualizes the tradeoff relationships between true positive rate (TPR) and false positive rate (FPR) with changing threshold. And AUC means area under the ROC curve. So, the ROC-AUC score means the area under the ROC curve and the closer to 1, the more reliable model is.

The recall, precision, *f1* score, and ROC-AUC score not appropriate to assess performances of the multiclass models, which consist of more than two species of label data, but suitable to assess those of the binary models, which consist of only two species of label data. Then, to assess performances of the models in this study, I utilized the accuracy, recall, precision, *f1* score, and ROC-AUC score in cases of binary models and utilized only the accuracy in cases of multiclass model. By using “cross val score” algorithm, the assessments are evaluated calculating average of each score from cross-validation (cv=10), which means resampling 10 times and calculating the performances for the each resample.

3.6 Criteria analysis using Decision tree

Decision tree is one of machine learning algorithms that finds a model predicting value of label data on the basis of training feature and label data by constructing tree structures (Myles et al., 2004; Cho and Kurup, 2011). The tree structures basically consist of nodes and branches (Fig. 6). The nodes are divided into root node that is starting node, decision nodes that can be divided into nodes, and terminal node that cannot be split anymore. Each node contains information for criterion of the node, gini score (gini), number of data contained in the node (samples), number of data belonged to each label data (value), type of label data (class). The gini score is score assessing a purity of the node. The gini score increases with increasing species of label data included in the node. The gini score is zero when the node only contains a single label data. Thus, the gini scores of all terminal nodes are zero. The nodes are classified by the branches. The branch on left and right sides means true and false for criterion of each node, respectively. The algorithm of Decision tree works downward from top (root node) to bottom

(decision node or terminal node) by partitioning off nodes on the basis of decision rules of each node. By repeating this process, the classification is achieved with growing the tree structure. In this study, I used a “graphviz” algorithm to visualize the tree structure as figure and “DecisionTreeClassifier” algorithm to mathematically interpret criteria of the classification for the data sets by analyzing the criterion of each node in the visualized tree structure.

3.7 Importance assessment using random forest

Importance assessment in machine learning is a method calculating which feature data more importantly influences on label data as scores for each feature by using a specific machine learning algorithm (Sung and Mukkamala, 2003; Hu et al., 2009; Park and Kim, 2019). The scores are called by feature importance. Given the method, I can interpret relationships between feature and label data by referring the feature importance. Although there are various ways to estimate the feature importance according to machine learning algorithms, I used a method utilizing Gini importance on the basis of Random Forest algorithm. Random Forest is ensemble machine learning algorithm operated by assembling a great number of specific Decision trees. A prediction of Random Forest is achieved by voting majority for the prediction results of each specific Decision tree. Gini importance, which is defined by a function describing homogeneity of label data (impurity function) in Random Forest algorithm, is utilized to calculate node importance. Assuming a decision tree with two terminal nodes split from one decision node, the node importance is expressed by

$$ni_j = w_j C_j - w_{left(j)} C_{left(j)} - w_{right(j)} C_{right(j)}$$

where ni_j is importance of node j , w_j is weighted number of samples on node j , and C_j is Gini importance of node j . $left(j)$ and $right(j)$ are left and right terminal node of node j , respectively. The importance of node j is increase with decreasing impurity of node j . The feature importance of feature i (fi_i) is estimated by dividing sum of importance of nodes split by feature i by sum of importance of all nodes.

$$fi_i = \frac{\sum_{j=\text{node } j \text{ split by feature } i} ni_j}{\sum_{k \in \text{all nodes}} ni_k}$$

To express f_i as value suited to Random Forest level, the feature importance is transformed to normalized value by dividing f_i by the sum of all importance of features and the normalized feature importance on each tree is divided by number of all Decision trees.

$$normfi_i = \frac{f_i}{\sum_{l \in \text{all features}} f_{il}}$$

$$RFfi_i = \frac{\sum_{t \in \text{all trees}} normfi_{it}}{T}$$

The $normfi_i$ and $RFfi_i$ are normalized feature importance and final feature importance fitted to Random Forest for feature i , respectively. To estimate the importance of features classified from Random Forest model, I used a “feature importances” algorithm with a “RandomForestClassifier” algorithm.

3.8 Probability map constructed by logistic regression

Logistic regression is also one of popular machine learning algorithms, which conducts classification by calculating probability for each event via a non-linear transformation of ordinary least squares for linear regression using a logistic or sigmoid function. The logistic function is a big difference between the logistic regression and linear regression models. The logistic function is expressed by

$$y = \frac{1}{1 + e^{-x}}$$

y is the probability and x is a weighted linear combination of feature data. The probability is assumed to limit between 0 and 1, as a binary system. x is defined as

$$x = b_0 + b_1z_1 + b_2z_2 + \dots + b_nz_n$$

where b_0 is the intercept, n is number of variable, b_i ($i = 1, 2, 3, \dots, n$) is the corresponding coefficients, and z_i is the independent variables for feature data. Considering the model, I can identify probability of each feature data for label data showing binary system as statistical value. Relationships between feature and label data can be expressed as a probability map by projecting the probabilities against feature parameters. In this study, I used a “LogisticRegression” algorithm to find out appropriate model representing relationships between feature data and label data. The verified model is visualized

by constructing probability map for each feature data to interpret the importance of features classified from Random Forest model.

4. Result

4.1 Scatterplot for the intensity of Cr-Al chemical zoning

Figure 7 exhibits the scatterplot for the ΔCA and ΔCE representing the intensity of Cr-Al zoning. Each data point is standardized from the pre-processing stage. The more the ΔCA and ΔCE are close to 0, Cr are more homogeneously distributed within the spinel grains. The intensity of Cr-Al zoning is intense with increasing the ΔCA and ΔCE to a positive value. The data points are distributed from -2 to 3 for the ΔCA and from -3 to 3 from the ΔCE . Although the ΔCA is diversely distributed with the ΔCE , distribution of the data points indicate proportional relationship between the ΔCA and ΔCE . Data points that ΔCA is less than 0 present ΔCE less than 1. Data points that ΔCE is more than 1 show ΔCA more than 0. This relationship is originally derived by characteristics of Cr-Al chemical zoning. Considering the features of Cr-Al chemical zoning, Cr is symmetrically distributed along long axis and minimally concentrated at both of tip areas. The ΔCA and ΔCE proportionally change in accordance with the intensity of Cr-Al zoning.

4.2 Criteria for clustering

The data points are clustered by using MCA with 0.942 of bandwidth calculated by 'estimate bandwidth' algorithm (Fig. 8). The data points are divided into 5 clusters as cluster 1 to 5 based on locations of a maximum density of the data points. Numbers of the data points included in the cluster 1, 2, 3, 4, and 5 are 53, 17, 14, 2, and 1, respectively. I considered only cluster 1, 2, and 3 as main clusters since cluster 4 and 5 contain too few data points to reflect meaning into the clusters. To interpret criteria for the clustering, the ΔCA and ΔCE data (feature data) and types of the clusters (label data) for each spinel grain are split into train data set containing 75 spinel data and test data set including 9 spinel data, and classified the data by applying to the Decision Tree algorithm. I estimated only accuracy

to assess performance of this model, because this is multiclass model as mentioned in section 3.5. The estimated average accuracy for the classification is 0.9167. Figure 9 is the visualized tree structure trained by train data set. There are 11 nodes containing a root node, 4 decision nodes, and 6 terminal nodes. Each cluster is classified by the 6 terminal nodes. Important nodes are root or decision nodes containing criterion that generates decision or terminal nodes consisting of a large number of samples and low gini score. Important nodes for cluster 1 are the root node 1 and decision node 2 deriving the terminal node 4. The root node 1 and decision node 3 and 6 are important nodes for cluster 2 characterized by the terminal node 11. Important nodes for cluster 3 are the root node 1 and decision node 3 defining the terminal node 7. The criteria of the important nodes for each of the cluster are expressed by

$$cluster\ 1 = \{\Delta CA \leq 0.176, \Delta CE \leq 0.284\}$$

$$cluster\ 2 = \{\Delta CA > 0.176, -0.527 < \Delta CE \leq 0.826\}$$

$$cluster\ 3 = \{\Delta CA > 0.176, \Delta CE > 0.826\}$$

Since both the ΔCA and ΔCE represent the difference of Cr and Al distributions at between tip and center area, the criteria can be simplified by considering intersection of the criteria for each cluster.

$$cluster\ 1 = \{\Delta \leq 0.176\}$$

$$cluster\ 2 = \{0.176 < \Delta \leq 0.826\}$$

$$cluster\ 3 = \{\Delta > 0.826\}$$

Δ is the intersection of the criteria of the ΔCA and ΔCE . The simplified criteria numerically explain that spinel grains are systemically clustered into three clusters regarding to the difference of Cr and Al distributions at between tip and center area and the difference is high in an order of the cluster 3, cluster 2, and cluster 1. Since the difference represents the intensity of the Cr-Al chemical zoning, each cluster can be interpreted by spinel grains having homogeneous chemical distribution for cluster 1, weak intensity of Cr-Al chemical zoning for cluster 2, and strong intensity of Cr-Al chemical zoning for cluster 3.

4.3 Feature importance

To estimate which geometrical factor controls the intensity of Cr-Al zoning more importantly, the feature importance is estimated from the feature data including information for the ΔCA and ΔCE , grain sizes (R), and aspect ratios (L) of spinel grains and label data composed by types of clusters. Figure 10 displays feature importance for each feature data. Since this model is also multiclass model, I calculated only accuracy to assess performance of this model. The calculated average accuracy is 0.9278. The ΔCA and ΔCE are the feature data displaying the first and second highest scores of feature importance, which mean that the ΔCA and ΔCE have the greatest impact on determining types of the clusters. The feature importance of grain size is the third highest and at the same time the highest among the geometrical properties. The score of grain size represents that grain size is closely related with types of the clusters. Aspect ratio is the feature data showing the lowest score of feature importance. The score of aspect ratio reflects that there are relatively low relationships between aspect ratio and the intensity of Cr-Al chemical zoning.

4.4 Probability map

To identify relative relationships between each feature and the Cr-Al chemical zoning in more detail, I inspect probability maps by using the Logistic regression method. Figure 11 displays the probability maps for features including the ΔCA and ΔCE , grain size (R), and aspect ratio (L). To represent the ΔCA and ΔCE data as a unified value, the ΔCA and ΔCE is simplified by calculating average. The average of the ΔCA and ΔCE is $aver\Delta$. The probability is expressed as values between 1 to 0 and the closer it is to 1, the more likely it is to be included in the cluster 2 and 3. Conversely, the closer the value is to 0, the higher the possibility of being included in the cluster 1. Given the criteria for the cluster 1, 2, and 3 in section 4.2, high values of the probability implies that possibility that the Cr-Al chemical zoning can be observed from the spinel grains is high. The probability maps are constructed by considering species of features as three cases; the $aver\Delta$ and grain size, the $aver\Delta$ and aspect ratio, and aspect ratio and grain size. Performances of these models are estimated by

evaluating scores for accuracy, recall, precision, $f1$, and ROC-AUC, because this is binary model as mentioned in section 3.5. Scores representing performances for each probability map are described in Table 2

In the probability map for the $aver\Delta$ and grain size, the probability is increase with increasing $aver\Delta$ and grain size. Variances of the probability with changing grain size are smaller than those with changing the $aver\Delta$. Intervals between each of contour line are relatively narrow, suggesting that criteria for distinction are relatively clear. The scatter plot for the $aver\Delta$ and grain size also represent the meaning for the narrow intervals of the contour lines. In the probability map for the $aver\Delta$ and aspect ratio, although changes of the probability for the $aver\Delta$ display a similar trend with those in the probability map for the $aver\Delta$ and grain size, there are no relationship for aspect ratio. The gaps between the contour lines are also similar with those for the probability map for the $aver\Delta$ and grain size. In the probability map for the aspect ratio and grain size, the probability is increase with increasing aspect ratio and grain size. Variances of the probability with changing grain size are bigger that those with changing aspect ratio. The intervals are much wider than the intervals of the probability maps for the $aver\Delta$ and grain size, and the $aver\Delta$ and aspect ratio.

5. Discussion

5.1 Interpretation for the analyzed data

In section 4.3 and 4.4, the machine learning analysis exhibits the feature importance representing much important factors for the intensity of Cr-Al zoning and the probability maps showing relative relationships between the factors and the intensity of Cr-Al zoning. In this section, I interpret the analyzed data and the relative relationships.

In Figure 10, the ΔCA and ΔCE show the first and second highest scores for feature importance representing the greatest influence to identifying the types of the clusters. It is obvious that the ΔCA and ΔCE is most important factors to the intensity of Cr-Al zoning, since the data points are originally clustered on the basis of the ΔCA and ΔCE . The probability maps for the ΔCA and ΔCE

also represent the connection (Fig. 11a-b). Feature importance indicates grain size is the third most important factor to the intensity of Cr-Al zoning. The importance score of grain size is smaller than those of the ΔCA and ΔCE and greater than that of the aspect ratio. This importance of grain size can be also certified from the probability maps (Fig. 11a, c). Although the variances of the probability with varying grain size are much smaller than those with varying $aver\Delta$ in the probability map for the $aver\Delta$ and grain size (Fig. 11a), the variances of the probability with altering grain size are much bigger than those with altering aspect ratio in the probability map for the aspect ratio and grain size (Fig. 11c). The both of the probability maps for grain size represent that the probability increases with increasing grain size, suggesting that the Cr-Al chemical zoning is observed more easily with increasing grain size. Figure 12a shows grain size distribution for each type of the clusters. The trend of increasing grain size in the order of the cluster 1, 2, and 3 reflects the relationships between grain size and the Cr-Al zoning. An importance score of aspect ratio is the lowest, about 10 times lower than those of the ΔCA and ΔCE and 5 times lower than that of grain size. The probability maps for aspect ratio also present the gaps of importance scores for aspect ratio (Fig. 11b-c). In the probability map for the $aver\Delta$ and aspect ratio (Fig. 11b), even if variances of the probability is relatively large with changing the $aver\Delta$, there are no variances for the probability with changing aspect ratio because the $aver\Delta$ much affect to the Cr-Al zoning compared to aspect ratio as about 10 times enormously. However, the probability map for aspect ratio and grain size displays effects for aspect ratio due to relative low difference of importance scores (Fig. 11c). The probability increases with increasing aspect ratio, implying that possibility, that the Cr-Al chemical zoning can be observed, increase with increasing aspect ratio. The intervals of contour lines are wider than those of the other maps because criteria for aspect ratio constructing the probability map is relatively unclearness. These relationships are displayed in the scatter plot for aspect ratio and grain size, and Figure 12b. Figure 12b shows aspect ratios of spinel grains for each type of the clusters. Although aspect ratio for each type of the clusters exhibits variation and aspect ratio for the cluster 1 is the lowest, there are no critical difference of aspect ratio between the cluster 1, 2, and 3.

5.2 Interpretation for relationships between grain size and the Cr-Al chemical zoning

As mentioned in section 5.1, grain size shows proportional relationship with the intensity of Cr-Al chemical zoning. To interpret the relationship, I assumed that the spinel grains having the Cr-Al chemical zoning are deformed by lattice diffusion on the basis of the Ozawa's model. Considering the assumption, the relationship between grain size and the intensity of Cr-Al chemical zoning can be interpreted as lattice diffusion becomes significant with increasing grain size of spinel. This interpretation can be explained by the ratio for grain boundary diffusion flux and lattice diffusion flux. The ratio (r_{diff}) is expressed by

$$r_{diff} = \frac{D_b \delta_b}{D_l R}$$

D_b and D_l is grain boundary diffusion coefficient and lattice diffusion coefficient, respectively. δ_b is grain boundary width and R is grain size. The r_{diff} , which is in inverse proportional to grain size, is related to dominant types of diffusion creep mechanisms. Lattice diffusion becomes important with decreasing the r_{diff} , and grain boundary diffusion become dominant with increasing the r_{diff} . Considering the ratio, D_b , D_l , and δ_b are relatively constant between minerals of same species within same rock sample and the only variable for the r_{diff} becomes R . On the basis of the relations, lattice diffusion is more active with increasing grain size. Considering the Ozawa's model that the Cr-Al chemical zoning in spinel grain is kinetic demixing caused by difference of diffusivity between Cr and Al during cation transport through lattice, lattice diffusion in spinel grain is associated with flux of Cr and Al. This means that the more lattice diffusion is active, the more cation is transported through lattice and the high flux of cation derives the high intensity of Cr-Al zoning. Then, the relationship between grain size and the intensity of Cr-Al chemical zoning suggests that the intensity is increase with increasing grain size because lattice diffusion is much active in coarser spinel grains. For types of the clusters, lattice diffusion is most intensely activated in cluster 3, intermediately in cluster 2, and relatively not activated in cluster1.

5.3 The R_{diff} and deformation temperature

The ratio for diffusion flux (r_{diff}) is controlled by grain boundary diffusion coefficient (D_b) and lattice diffusion coefficient (D_l), grain boundary width (δ_b), and grain size (R). And the D_b and D_l are changed with varying temperature. Thus, I can calculate variations of the r_{diff} in accordance with changing of temperature and the R . There were studies investigating specific values of the r_{diff} representing transition of diffusion creep mechanisms from grain boundary diffusion to lattice diffusion. Considering the specific values of the r_{diff} , critical grain size (R_c), which is grain size deriving the transition of diffusion creep mechanisms, can be determined according to each temperature condition. By comparing the calculated R_c and grain size distribution for each type of the clusters, I estimated deformation temperature of spinel grain.

The D_b is grain boundary diffusion coefficient for the slowest atom on grain boundary of spinel grain and the D_l is lattice diffusion coefficient for the slowest atom within lattice of spinel grain, since the slowest atoms controls diffusion creep of mineral. To calculate the r_{diff} , I supposed that O and Cr are the slowest atom in grain boundary and lattice of spinel grain, respectively (Joesten, 1991; Suzuki et al., 2008; Nakakoji and Hiraga, 2018). The δ_b is assumed as 1 nm. Since there has been no direct estimation of the O grain boundary diffusion coefficient for spinel grain, the O grain boundary diffusion coefficient is derived by referring results of previous studies (Oishi and Ando, 1975; Reddy and Cooper, 1981; Ando and Oishi, 1983), in which O self-diffusion coefficient of polycrystalline spinel is approximately 4 orders faster than that of single spinel crystal due to diffusion of O improved along grain boundaries. Given the result, I calculated approximate O grain boundary diffusion coefficient by multiplying 4 orders to O self-diffusion coefficient estimated by the result. As mentioned from Suzuki et al. (2008), the approximately calculated O grain boundary diffusion coefficient is about 5 orders greater than the O self-diffusion coefficient estimated from Reddy and Cooper (1981) and Ando and Oishi (1983). The Cr lattice diffusivity is computed by extrapolating Cr self-diffusion coefficients data from Suzuki et al. (2008). By applying the calculated D_b and D_l to the r_{diff} , I evaluated the r_{diff} for various temperatures and grain sizes (Table3).

Swaroop et al. (2005) reported that the R_c deriving a transition from grain boundary diffusion to lattice diffusion is determined by

$$R_c \approx \frac{1.2D_b\delta}{D_l}$$

The specific value of the r_{diff} can be calculated by modifying the equation.

$$0.83 \approx \frac{D_b\delta}{D_lR} = r_{diff}$$

Shibutani et al. (1998) reviewed that there are three types of diffusion processes controlling cavity growth derived by diffusion, depending on the r_{diff} . The r_{diff} for the types of processes is introduced as

- (a) $r_{diff} > 1$: Grain boundary diffusion dominant
- (b) $0.1 < r_{diff} < 1$: Grain boundary diffusion + Lattice diffusion
- (c) $r_{diff} < 0.1$: Lattice diffusion dominant

Since this model indicates that the transition is occurred from the (b) range of the r_{diff} , the transition may be occurred from a grain size achieving $r_{diff} = 1$.

I estimated the r_{diff} (Table 3) and the R_c (Table 4) with various temperature and grain size based on the two models. Both of the model represents that the r_{diff} is decrease with increasing grain size and temperature, and the R_c decrease with increasing temperature, suggesting that relative significance of lattice diffusion to total diffusion creep increases with increasing temperature (Fig. 13).

The activity of lattice diffusion for types of the clusters discussed in section 4.3 show that lattice diffusion begins to active from the cluster 2. Deformation temperature can be estimated by comparing the grain sizes of Q1 (73.5 μm) and minimum (22 μm) of the cluster 2, and the critical grain sizes in Table 4. By considering difference between the Q1 and minimum grain sizes, deformation temperature is expressed as ranges. For the equation of Swaroop et al. (2005), the temperature representing the critical grain size closest to the grain size of Q1 is 1100°C and the temperature for the grain size of minimum is 1250°C. Then, the deformation temperature range is estimated as 1250-1100°C. The estimated deformation temperature calculated by supposing the equations of Shibutani et

al. (1998) is also 1250-1100°C.

The CPO patterns of the olivine grains and the P-T trajectory of the Horoman Peridotite Complex based on chemical compositional zoning of pyroxenes and whole rock compositions (Ozawa and Takahashi, 1995 and Takahashi, 2004) support the proposal that the estimated deformation temperature range is 1250-1100 °C. The A-type CPO of the olivine grains represent that the olivine grains are deformed in high temperature condition (approximately > 1100 °C). Since I supposed the deformation of the olivine grains forming A-type CPO coincides with the deformation of the spinel grains in section 2.1 based on their microstructures, the range of the estimated temperature is consistent. On the basis of the P-T trajectory of the Horoman Peridotite Complex, the equilibrium temperature of spinel peridotite for the Transition Zone including the dunite sample is estimated to be intermediate temperature between the equilibrium temperature of spinel peridotite of the Upper (1150-1100 °C) and Lower Zone (950-900 °C). Takahashi (2004) reported that the temperature difference from the Upper to the Lower Zone is gradual. By considering the sampling area that is located very near to the Upper zone, the equilibrium temperature for the dunite sample may be closer to that of the Upper Zone than the Lower Zone, implying that the range of the estimated temperature is consistent.

5.4 Interpretation for relationships between aspect ratio and the Cr-Al chemical zoning

Although aspect ratio is less correlated with the intensity of Cr-Al chemical zoning than grain size, aspect ratio also represents relationship with the intensity (Fig. 11c). The probability map and scatter plot in Fig. 11c describes two of characteristics for aspect ratio, which are that the probability decrease with decreasing aspect ratio and aspect ratio for spinel grains smaller than about 100 µm is relatively low, representing that spinel grains having homogeneous chemical distribution show relatively fine grain size and low aspect ratio. The characteristics suggest that the relationship between aspect ratio and the chemical zoning is correlated with grain size. I considered that the relationship between the chemical zoning, aspect ratio, and grainsize is derived by the effect of the rounding process introduced by Toriumi (1987), Okamoto and Michibayashi (2005), and Uhmb and Michibayashi (2022). Isolated mineral inclusions have a tendency to a spherical shape to minimize their surface energy, which

is referred as the rounding process, during post-deformational annealing stage, and effects of the rounding process are related with grain size and temperature because the rounding process is controlled by diffusion creep. The effects of the rounding process increase with decreasing grain size, increasing deformation temperature, and increasing annealing time. Since deformation temperature and annealing time is identical along the dunite sample, the effect of the rounding process on the sample is only activated in accordance with variable of grain size. Given the effect of the rounding process, I thought that the fine spinel grains became more round shape than coarse grains during annealing stage and the trend of decreasing the probability with decreasing aspect ratio is derived by the relationship between grain size and the chemical zoning, that the chemical zoning is less observable in finer grains.

6. Conclusion

I used unsupervised (MCA) and supervised (Decision tree and Random Forest) machine learning method to inspect relationship between the intensity of Cr-Al chemical zoning and the geometrical properties of spinel grains collected from a dunite sample within the dunite layer in the Transition Zone in the Horoman peridotite complex, northern Japan. The intensity of Cr-Al chemical zoning for each spinel grain was estimated by calculating differences of Cr distributions analyzed from EDS line scanning data at between center area and both of tip areas along long axis of each spinel grain (ΔCA and ΔCE). By utilizing MCA, the ΔCA and ΔCE data were mainly clustered into three kinds of clusters (cluster 1, 2, and 3). The tree structure of Decision tree classification, which was conducted by setting the ΔCA and ΔCE data as feature data and types of the clusters as label data, revealed that the spinel grains are systematically clustered based on degree of the intensity of Cr-Al chemical zoning. The intensity is relatively strong in cluster 3 and weak in cluster 2, respectively. The spinel grains for cluster 1 exhibited homogeneous chemical distribution. Feature importance analysis of Random Forest method, that was performed by adding geometrical properties (grain size and aspect ratio) of the spinel grains to the existing feature data, represented that grain size is one of factor closely related with the intensity of Cr-Al chemical zoning. The trend of grain size distribution for each type of the clusters

displayed grain size increase with increasing the intensity of Cr-Al chemical zoning. On the basis of the model of Ozawa (1989) and the ratio of diffusion flux (R_{diff}), this relationship is interpreted as lattice diffusion is most strongly activated in cluster 1, intermediately in cluster 2, and not activated in cluster 1, suggesting that lattice diffusion is much active in coarser spinel grains. By considering the two models for the R_{diff} proposed by Swaroop et al. (2005) and Shibutani et al. (1998), I estimated the critical grain size (d_c) for the spinel grains with various temperature conditions (Fig. 13). The deformation temperatures of the spinel grains were estimated by comparing the grain sizes of Q1 and minimum of cluster 2, and the d_c . The estimated deformation temperature is consistent with the deformation temperature for the CPO patterns of the olivine grains and the equilibrium temperature the P-T trajectory of the Horoman Peridotite Complex reported by Ozawa and Takahashi (1995) and Takahashi (2004) as 1250-1100°C.

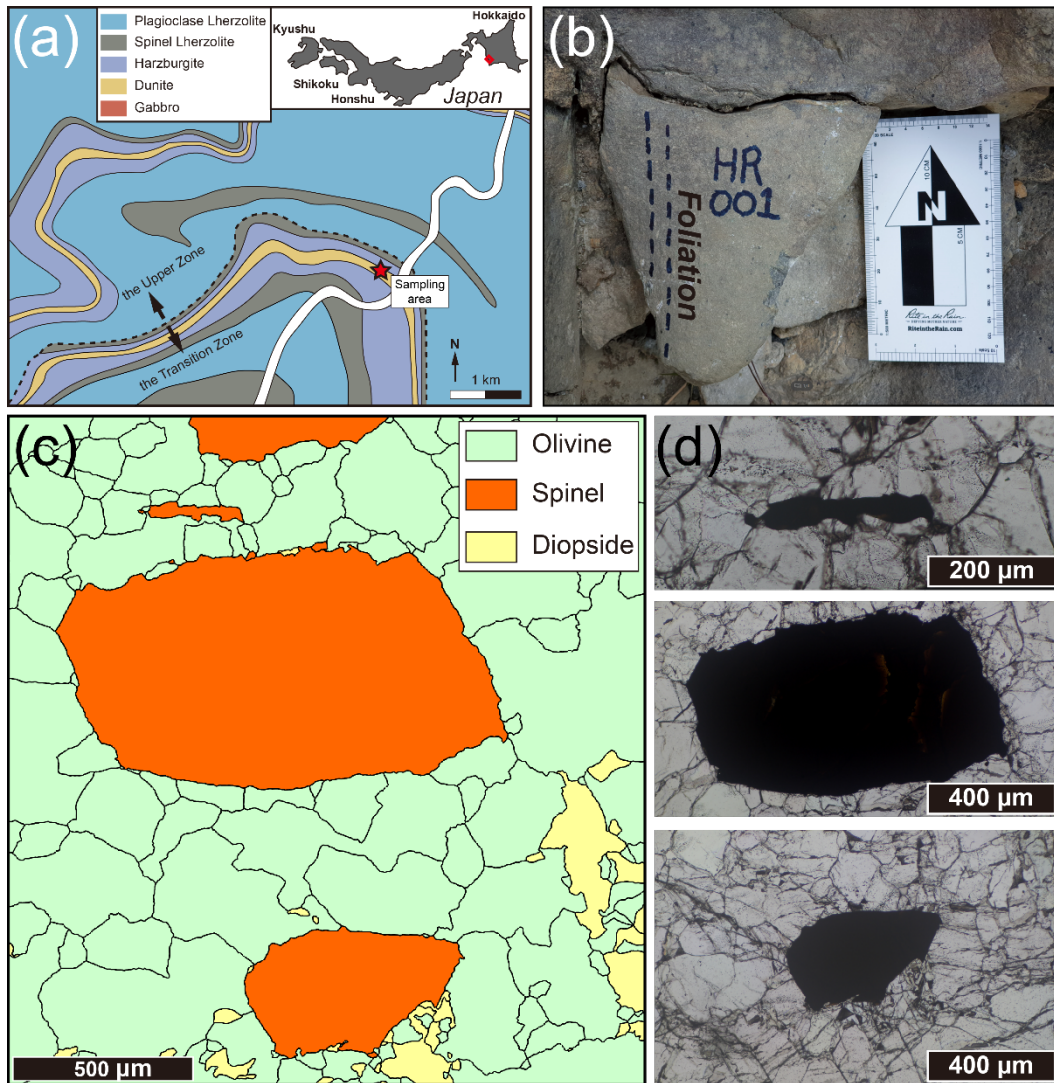


Figure 1. (a) Geological map of the Horoman Peridotite Complex in Hokkaido, Japan, modified from Ozawa and Takahashi (1995). The sampling area is the dunite layer near to the Upper Zone within the Transition Zone. (b) Outcrop photograph of the dunite sample. The foliation is marked by dash lines. (c) Representative phase map for the dunite sample were obtained by SEM-EBSD. (d) Optical photomicrographs (PPL) of the spinel grains within the phase map of (c). The elongated spinel grains show various grain size and aspect ratio.

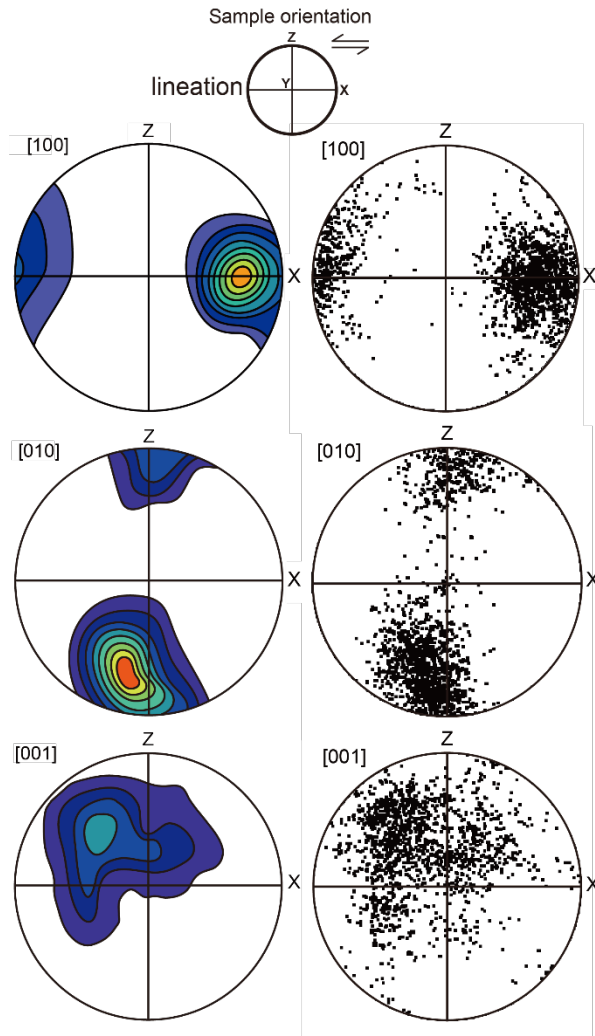


Figure 2. CPOs of olivine grains in the dunite sample. Equal-area lower-hemisphere projection. Right projections are point plot for all olivine data onto each axis and left projections are contour plot for the same data.

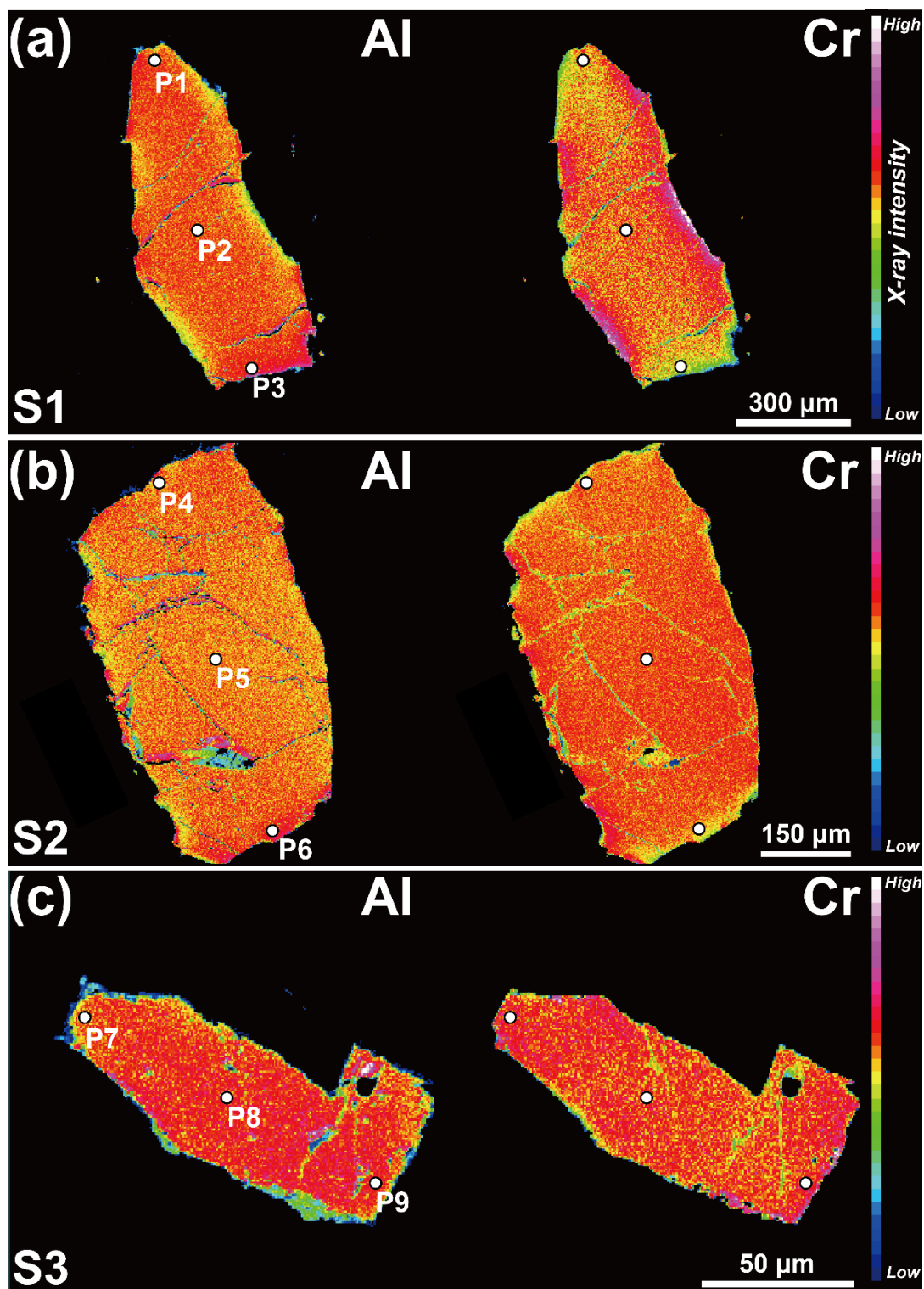


Figure 3. EPMA-WDS mapping data for representative three spinel samples (S1, S2, S3) showing each different Cr and Al chemical distribution. Spinel samples exhibiting relatively (a) strong (S1), (b) weak (S2) intensity of Cr-Al chemical zonation, and (c) homogenous chemical distribution (S3). White circles nominated from P1 to P9 within each spinel sample are location conducting point analysis. Detailed point analysis data are set out in Table 1.

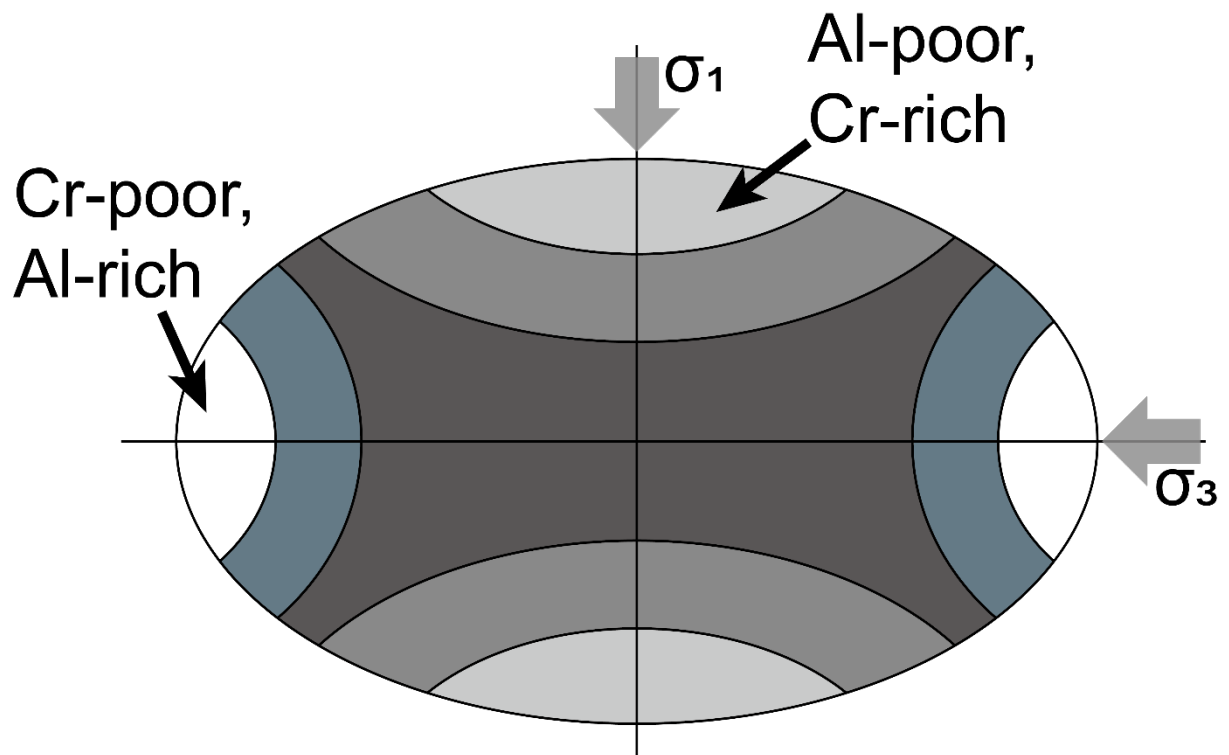


Figure 4. Schematic figure of multipolar Cr-Al chemical zoning in two dimensions reported by Ozawa (1989), modified from Suzuki et al. (2008).

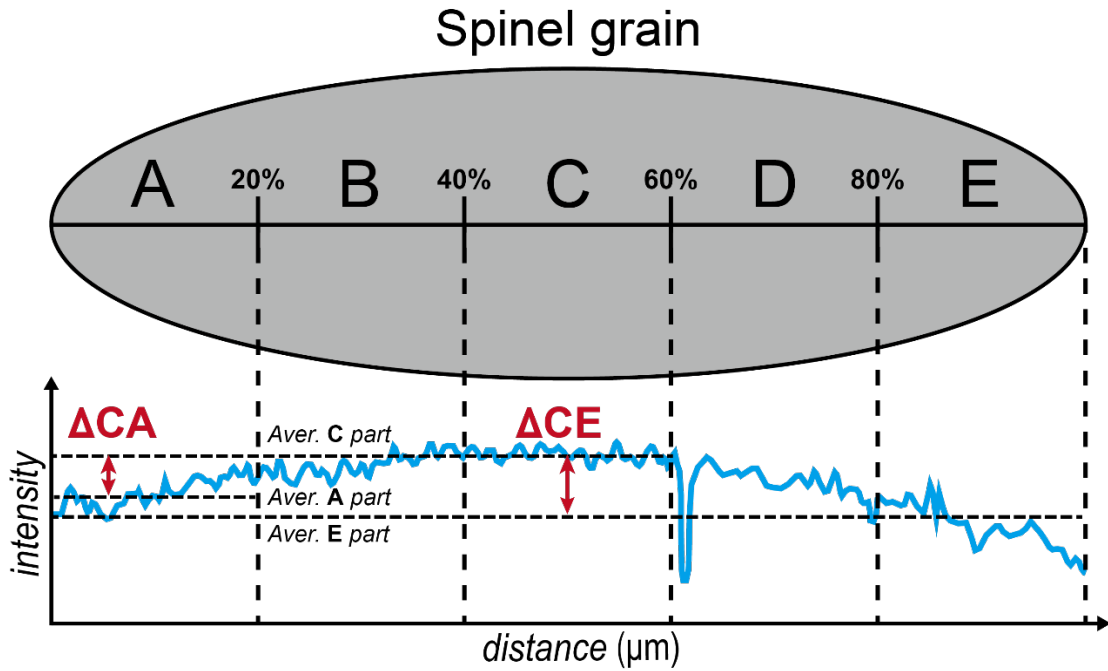


Figure 5. Representative EDS line scanning data for Cr. The EDS data observed along long axis of the elongated spinel from tip to opposite tip is divided into five equal parts from A to E. ΔCA and ΔCE are differences between the average intensity of E part (Aver. C part) and the average intensity of each tip part (Aver. C part and Aver. E part).

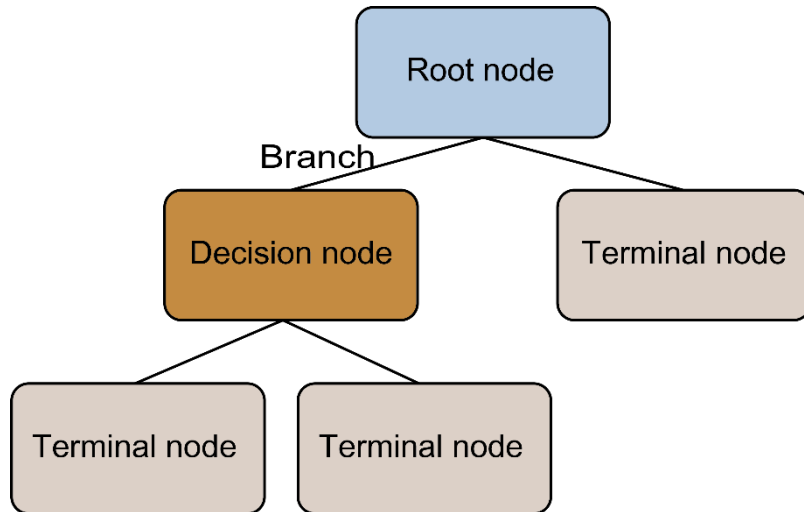


Figure 6. Schematic illustration explaining the tree structure of Decision tree.

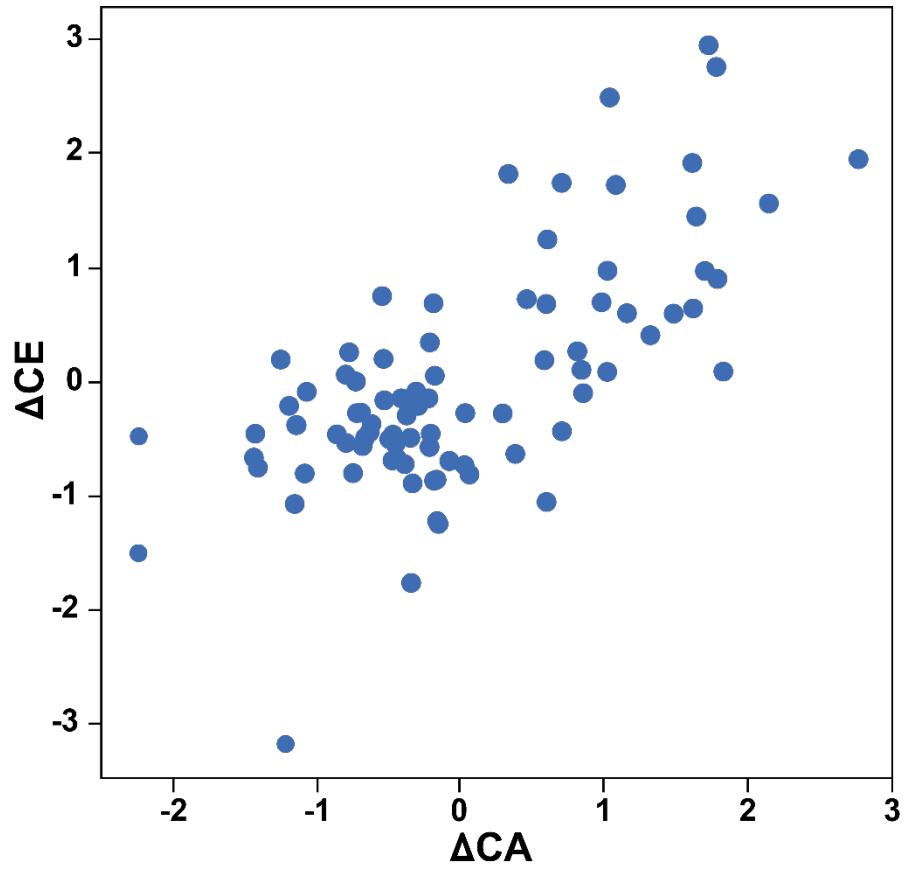


Figure 7. Scatterplot of the ΔCA versus the ΔCE for the spinel samples.

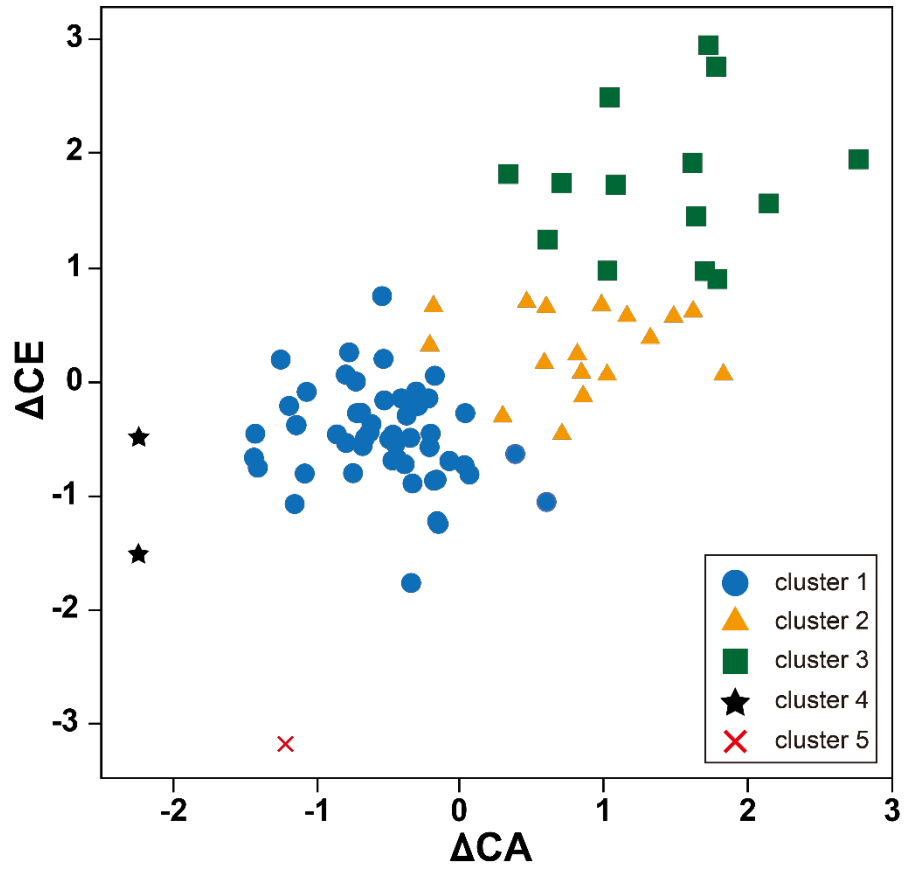


Figure 8. Clustering result for the data points. The data points are clustered as 5 clusters. Marks for each cluster are shown.

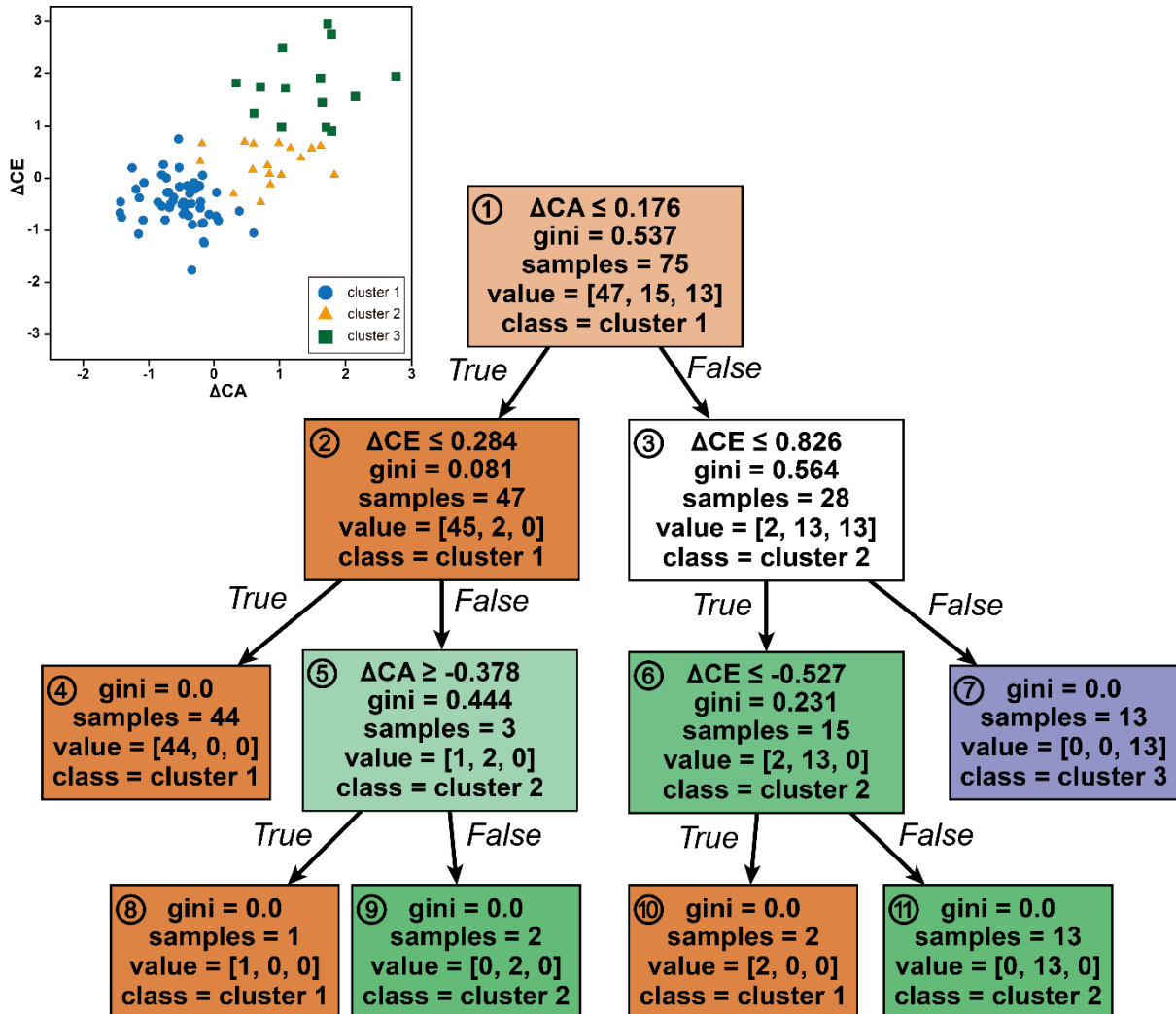


Figure 9. The visualized tree structure classifying the spinel data. Each node numbered from 1 to 11 contains information including gini score (gini), number of data (sample), numbers of data for each label data (value), and type of label data (class). A scatterplot located in upper left side shows region of clusters classified by this tree structure.

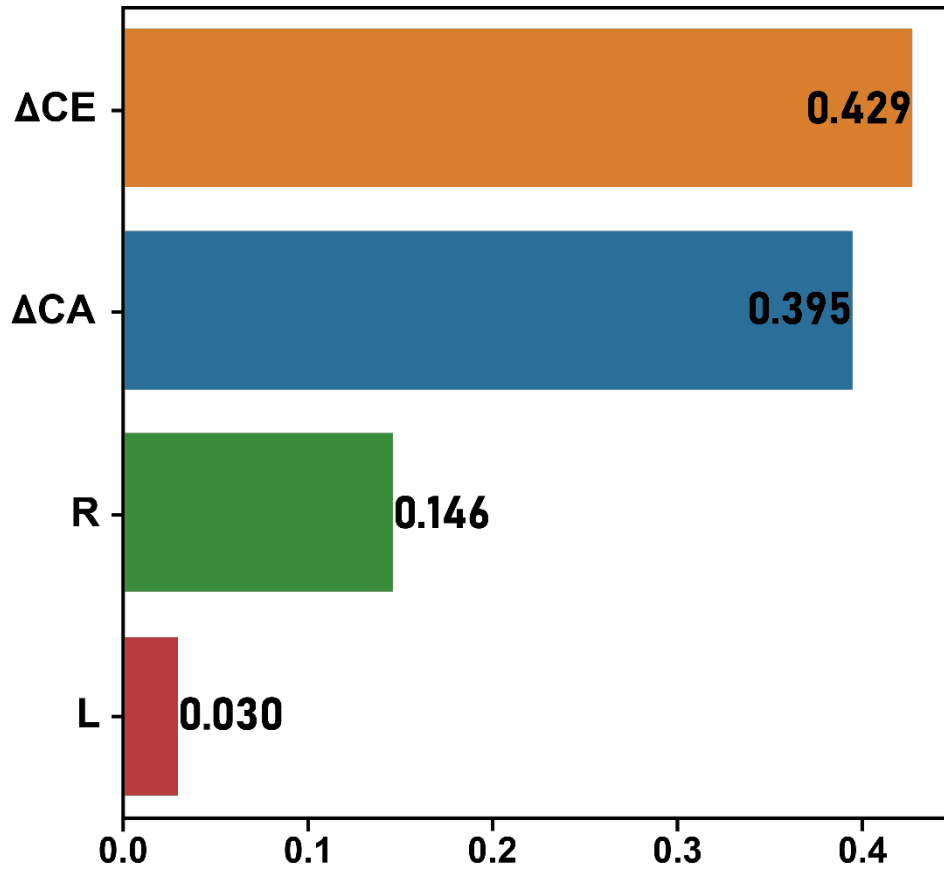


Figure 10. A bar chart describing feature importance of the feature data. Values beside each bar are the scores for feature importance.

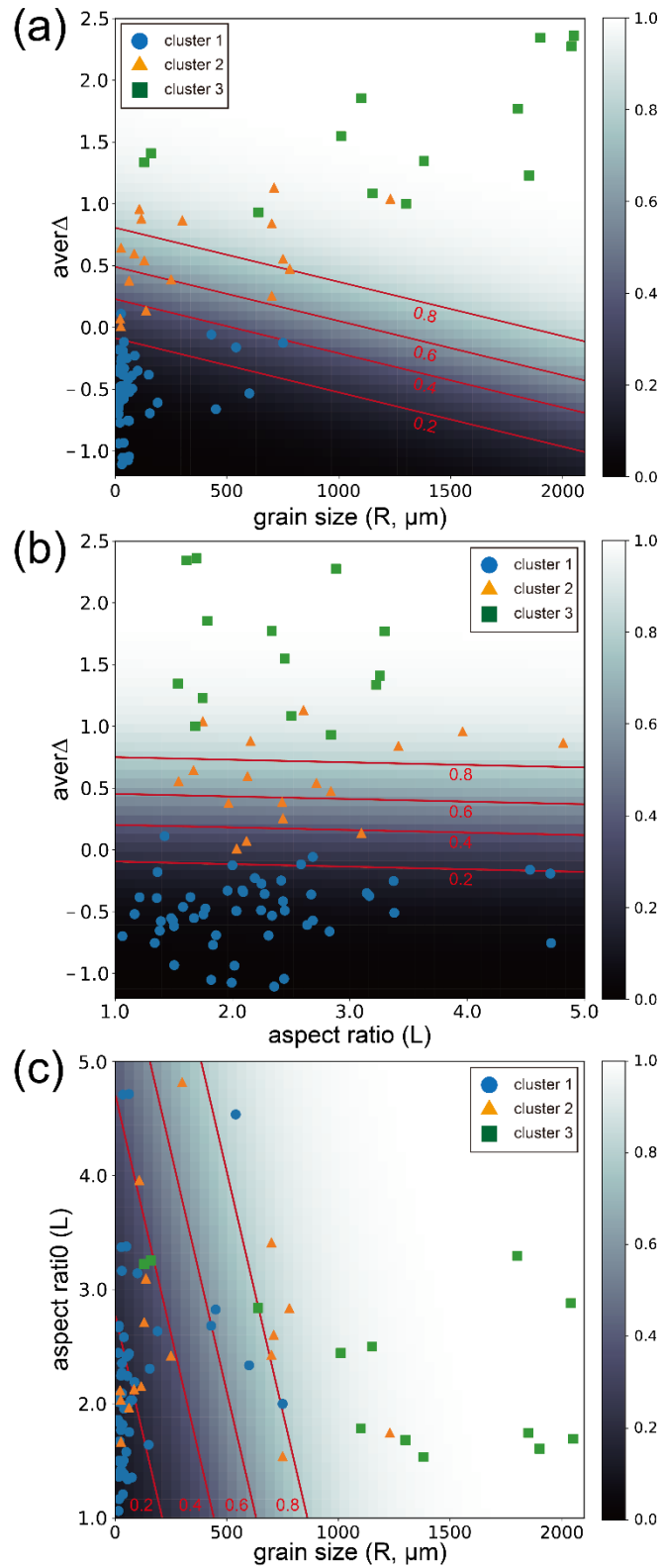


Figure 11. Probability maps for (a) the $aver\Delta$ and grain size, (b) the $aver\Delta$ and aspect ratio, and (c) aspect ratio and grain size. The probability is expressed in brighter color as it increased, and in darker color as it decreased. Red lines are contour lines for 0.8, 0.6, 0.4, 0.2 of probabilities. Clustered spinel data points are overlaid on the probability maps.

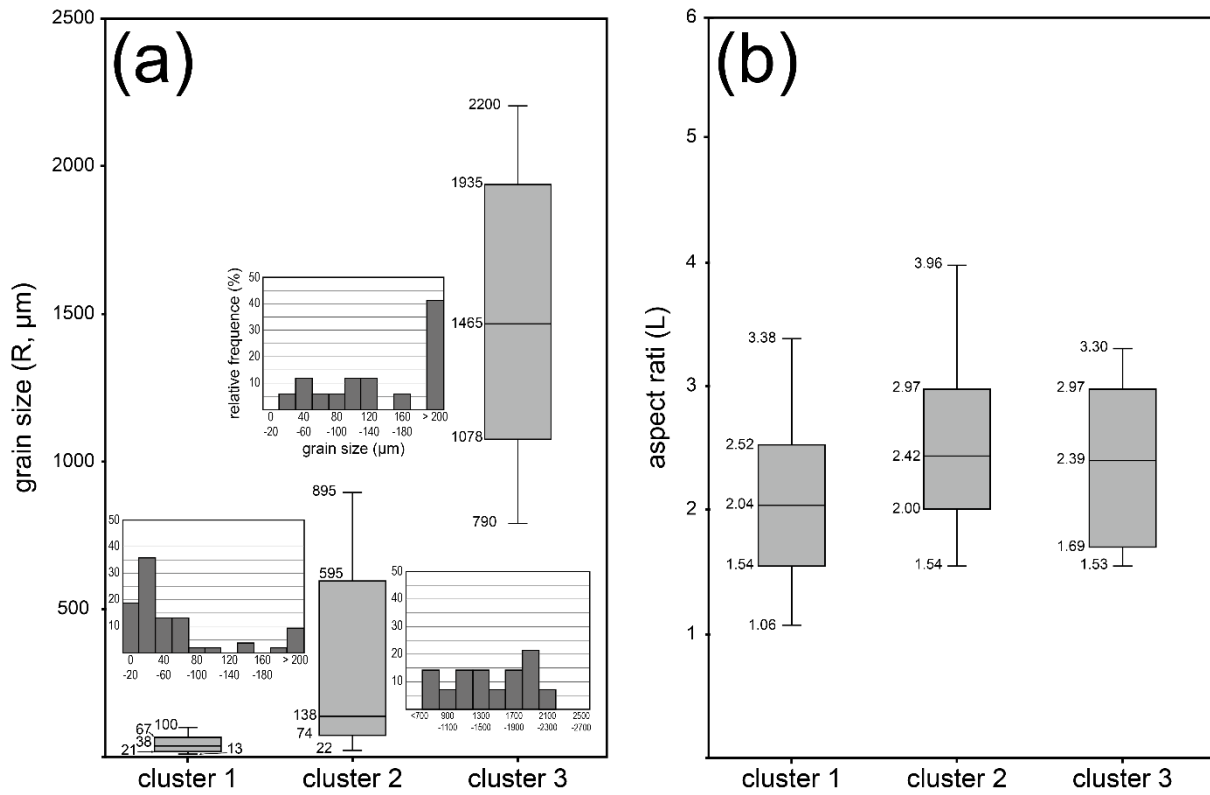


Figure 12. Box plots for (a) grain size and (b) aspect ratio in different types of the clusters. Values in each of box plot are (a) grain size and (b) aspect ratio of maximum, Q3 (75 %), median, Q1 (25 %), minimum. Bar charts within (a) show logarithmic grain-size distributions for each cluster.

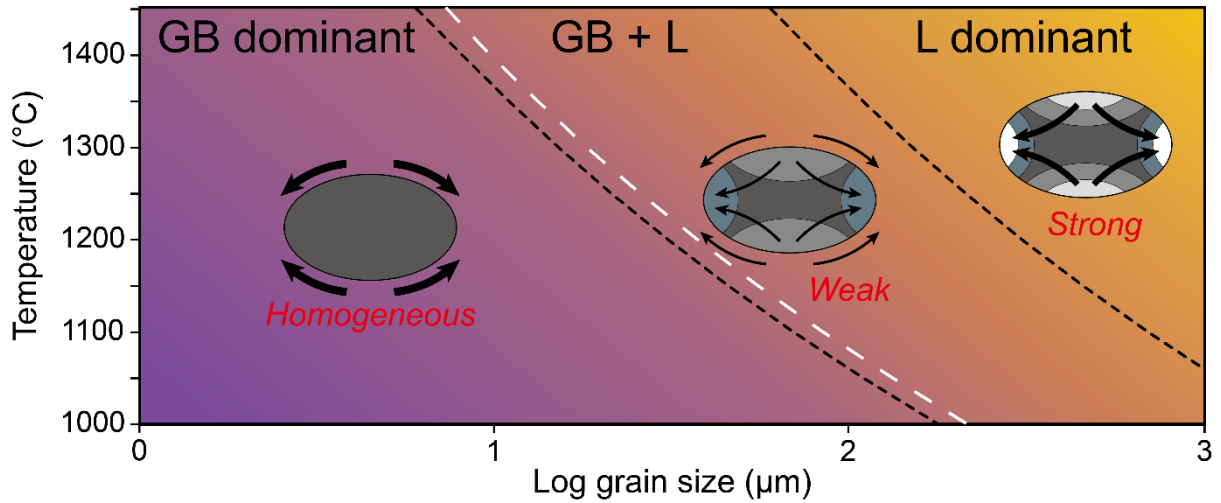


Figure 13. Relative importance of diffusion creep mechanism to total diffusion creep of chromite spinel with various grain size and temperature conditions constructed by considering the model of Shibutani et al. (1998). GB and L are grain boundary and lattice diffusion, respectively. Black dash lines are boundaries changing dominant diffusion mechanisms for the model of Shibutani et al. (1998). A white dash line is a transition boundary of diffusion mechanisms from grain boundary diffusion to lattice diffusion based on the model of Swaroop et al. (2005). Characters colored red represent the intensity of Cr-Al chemical zoning.

Table 1. Chemical compositions of each analysis point measured by EPMA for representative three spinel grains (S1, S2 and S3).

| Point No. | Al ₂ O ₃ | FeO | MnO | MgO | Cr ₂ O ₃ | NiO | TiO ₂ | Total (wt%) |
|-----------|--------------------------------|-------|------|-------|--------------------------------|------|------------------|-------------|
| P1 | 39.00 | 18.47 | 0.21 | 15.45 | 25.86 | 0.21 | 0.25 | 99.44 |
| P2 | 35.23 | 18.90 | 0.20 | 14.73 | 29.90 | 0.20 | 0.25 | 99.39 |
| P3 | 38.62 | 19.63 | 0.19 | 14.65 | 25.85 | 0.21 | 0.26 | 99.41 |
| P4 | 37.99 | 19.63 | 0.19 | 14.65 | 25.85 | 0.21 | 0.26 | 98.78 |
| P5 | 36.68 | 20.34 | 0.21 | 14.45 | 27.01 | 0.17 | 0.27 | 99.12 |
| P6 | 37.96 | 19.17 | 0.17 | 15.40 | 26.25 | 0.23 | 0.23 | 99.41 |
| P7 | 35.96 | 20.53 | 0.22 | 14.58 | 28.12 | 0.23 | 0.28 | 99.93 |
| P8 | 35.90 | 19.53 | 0.20 | 15.28 | 28.39 | 0.21 | 0.23 | 99.73 |
| P9 | 35.87 | 20.03 | 0.24 | 14.71 | 28.21 | 0.24 | 0.28 | 99.57 |

Table 2. Performances for each probability map. Each score is average for cross-validation (cv=10). *aver* Δ is average of the ΔCA and ΔCE . R is grain size. L is aspect ratio.

| | <i>aver</i> Δ and R | <i>aver</i> Δ and L | L and R |
|-----------|----------------------------|----------------------------|---------|
| Accuracy | 0.95 | 0.96 | 0.79 |
| Recall | 0.90 | 0.90 | 0.58 |
| Precision | 0.98 | 1.00 | 0.77 |
| f1 score | 0.92 | 0.93 | 0.63 |
| ROC-AUC | 0.99 | 0.99 | 0.89 |

Table 3. The ratio of diffusion flux (r_{diff}) for various grain size with changing temperature condition.

| T (°C) \ log grain size (μm) | 0 | 0.25 | 0.5 | 0.75 | 1 | 1.25 | 1.5 | 1.75 | 2 | 2.25 | 2.5 | 2.75 | 3 |
|------------------------------|--------|--------|-------|-------|-------|-------|------|------|------|------|------|------|------|
| 1450 | 6.10 | 3.43 | 1.93 | 1.08 | 0.61 | 0.34 | 0.19 | 0.11 | 0.06 | 0.03 | 0.02 | 0.01 | 0.01 |
| 1400 | 8.12 | 4.57 | 2.57 | 1.44 | 0.81 | 0.46 | 0.26 | 0.14 | 0.08 | 0.05 | 0.03 | 0.01 | 0.01 |
| 1350 | 11.01 | 6.19 | 3.48 | 1.96 | 1.10 | 0.62 | 0.35 | 0.20 | 0.11 | 0.06 | 0.03 | 0.02 | 0.01 |
| 1300 | 15.20 | 8.55 | 4.81 | 2.70 | 1.52 | 0.85 | 0.48 | 0.27 | 0.15 | 0.09 | 0.05 | 0.03 | 0.02 |
| 1250 | 21.45 | 12.06 | 6.78 | 3.81 | 2.15 | 1.21 | 0.68 | 0.38 | 0.21 | 0.12 | 0.07 | 0.04 | 0.02 |
| 1200 | 30.98 | 17.42 | 9.80 | 5.51 | 3.10 | 1.74 | 0.98 | 0.55 | 0.31 | 0.17 | 0.10 | 0.06 | 0.03 |
| 1150 | 45.92 | 25.82 | 14.52 | 8.17 | 4.59 | 2.58 | 1.45 | 0.82 | 0.46 | 0.26 | 0.15 | 0.08 | 0.05 |
| 1100 | 70.04 | 39.39 | 22.15 | 12.46 | 7.00 | 3.94 | 2.21 | 1.25 | 0.70 | 0.39 | 0.22 | 0.12 | 0.07 |
| 1050 | 110.29 | 62.02 | 34.88 | 19.61 | 11.03 | 6.20 | 3.49 | 1.96 | 1.10 | 0.62 | 0.35 | 0.20 | 0.11 |
| 1000 | 179.98 | 101.21 | 56.92 | 32.01 | 18.00 | 10.12 | 5.69 | 3.20 | 1.80 | 1.01 | 0.57 | 0.32 | 0.18 |

Table 4. Critical grain sizes (R_c) for various temperature conditions

| T (°C) | ^a R_c | ^b R_c |
|--------|--------------------|--------------------|
| 1450 | 7.32 | 6.10 |
| 1400 | 9.75 | 8.12 |
| 1350 | 13.21 | 11.01 |
| 1300 | 18.24 | 15.20 |
| 1250 | 25.74 | 21.45 |
| 1200 | 37.18 | 30.98 |
| 1150 | 55.11 | 45.92 |
| 1100 | 84.05 | 70.04 |
| 1050 | 132.35 | 110.29 |
| 1000 | 215.98 | 179.98 |

Considering the models of ^aSwaroop et al. (2005) and ^bShibutani et al. (1998)

Epilogue

These studies represent that the computational science is helpful tool to the study for deformation of solid earth. Especially, the applicability of computer simulation and artificial intelligence (AI) are verified from the part I and part II. In the part I, the deformation duration and cooling rate of the Teshima shear zone are estimated by simulating a numerical model representing shape-changes of K-feldspar inclusions as geological time scales. The deformation durations and cooling durations of the shear zone are estimated as 16,500-8400 yr, and 20-70 °C/Myr, respectively. Moreover, the shear strain of the shear zone is also evaluated as 50-260 by multiplying the deformation duration by strain rate of the shear zone. In part II, the relationships between the chemical characteristics and the geometrical properties of spinel grains in the Horoman dunite sample are specified by using unsupervised and supervised machine learning. The unsupervised machine learning is utilized to cluster data for chemical characteristics of spinel grains (MCA). A tree Structure of classification and feature importance for data of spinel grains are identified by using the supervised machine learning (Decision tree and Random Forest). The results represent that grain size is one of factor significantly related with the chemical characteristics of spinel grains, suggesting that relative importance of lattice diffusion to total diffusion creep increase with increasing grain size and deformation temperature of spinel grain. As studies of the part I and part II, the deformation of mineral of the part I are calculated as geological time scale by applying numerical model to computer simulation and deformational characteristics of mineral are defined by using machine learning analysis. The methods of the computational science field can be adapted to studies for the deformation of solid earth regardless of not only variety of mineral species but also temporal and spatial scales and can be used to the studies as a smart supporter. I consider that the collaborative research between the computational science and geoscience has many opportunities to understanding and interpreting the deformation of solid earth.

Acknowledgement

I would like to express my deepest thanks to Prof. Katsuyoshi Michibayashi and Prof. Yui Kouketsu for kind and great advice and guidance given to me during my PhD studies. In particular, many thank you so much to Prof. Katsuyoshi Michibayashi for allowing me not only to have fun and interest in research but also to have a dream again. I would also like to thank to all members of the Research Group of Mineralogy and Petrology at Nagoya University for helping by PhD life. The PhD studies was supported by a student grant awarded to T.U. by the Graduate school of Environmental Studies of Nagoya University, the Fujii International Scholarship, the THERS Interdisciplinary Frontier Next Generation Researcher fund, and a research grant awarded to K.M. by the Japan Society for the Promotion of Science (16H06347). I am thankful for the Japanese Government for supporting me to fund my all of PhD studies by awarding me various scholarships.

References

Part 1

- Brady, J. B., & Cherniak, D. J. (2010). Diffusion in minerals: an overview of published experimental diffusion data. *Reviews in mineralogy and geochemistry*, 72(1), 899-920.
- Brodie, K. H., & Rutter, E. H. (2000). Deformation mechanisms and rheology: why marble is weaker than quartzite. *Journal of the Geological Society*, 157(6), 1093-1096.
- Cherniak, D. J. (2003). Silicon self-diffusion in single-crystal natural quartz and feldspar. *Earth and Planetary Science Letters*, 214(3-4), 655-668.
- Cherniak, D. J. (2010). Cation diffusion in feldspars. *Reviews in Mineralogy and Geochemistry*, 72(1), 691-733.
- Coble, R. L. (1963). A model for boundary diffusion controlled creep in polycrystalline materials. *Journal of applied physics*, 34(6), 1679-1682.
- Cross, A. J., Prior, D. J., Stipp, M., & Kidder, S. (2017). The recrystallized grain size piezometer for quartz: An EBSD-based calibration. *Geophysical Research Letters*, 44(13), 6667-6674.
- Farver, J. R., & Yund, R. A. (1995). Interphase boundary diffusion of oxygen and potassium in K-feldspar/quartz aggregates. *Geochimica et Cosmochimica Acta*, 59(18), 3697-3705.
- Fossen, H., & Tikoff, B. (1993). The deformation matrix for simultaneous simple shearing, pure shearing and volume change, and its application to transpression-transension tectonics. *Journal of Structural Geology*, 15(3-5), 413-422.
- Freeman, J. J., Wang, A., Kuebler, K. E., Jolliff, B. L., & Haskin, L. A. (2008). Characterization of natural feldspars by Raman spectroscopy for future planetary exploration. *The Canadian Mineralogist*, 46(6), 1477-1500.
- Handy, M. R. (1990). The solid-state flow of polymineralic rocks. *Journal of Geophysical Research: Solid Earth*, 95(B6), 8647-8661.
- Hiraga, T., Nishikawa, O., Nagase, T., Akizuki, M., & Kohlstedt, D. L. (2002). Interfacial energies for quartz and albite in pelitic schist. *Contributions to Mineralogy and Petrology*, 143(6), 664-672.

- Hirth, G., & Tullis, J. A. N. (1992). Dislocation creep regimes in quartz aggregates. *Journal of structural geology*, 14(2), 145-159.
- Hirth, G., Teyssier, C., & Dunlap, J. W. (2001). An evaluation of quartzite flow laws based on comparisons between experimentally and naturally deformed rocks. *International Journal of Earth Sciences*, 90(1), 77-87.
- Tokada, T. (1998). Phase relations and P–T conditions of the Ryoke pelitic and psammitic metamorphic rocks in the Ina district, Central Japan. *Island Arc*, 7(4), 609-620.
- Holness, M. B., & Clemens, J. D. (1999). Partial melting of the Appin Quartzite driven by fracture-controlled H₂O infiltration in the aureole of the Ballachulish Igneous Complex, Scottish Highlands. *Contributions to Mineralogy and Petrology*, 136(1-2), 154-168.
- Joesten, R. (1991). Grain-boundary diffusion kinetics in silicate and oxide minerals. In *Diffusion, atomic ordering, and mass transport* (pp. 345-395). Springer, New York, NY.
- Kingery, W. D., Bowen, H. K., & Uhlmann, D. R. (1976). *Introduction to ceramics* (Vol. 17). John Wiley & Sons.
- Lasaga, A. C. (1998). Kinetic theory in the earth science, Princeton Univ.
- Lister, G. S., & Dornsiepen, U. F. (1982). Fabric transitions in the Saxony granulite terrain. *Journal of Structural Geology*, 4(1), 81-92.
- Mainprice, D., Bouchez, J. L., Blumenfeld, P., & Tubià, J. M. (1986). Dominant c slip in naturally deformed quartz: implications for dramatic plastic softening at high temperature. *Geology*, 14(10), 819-822.
- Mancktelow, N. S. (1987). Atypical textures in quartz veins from the Simplon Fault Zone. *Journal of structural geology*, 9(8), 995-1005.
- Mancktelow, N. S., & Pennacchioni, G. (2010). Why calcite can be stronger than quartz. *Journal of Geophysical Research: Solid Earth*, 115(B1).
- Mancktelow, N. S. (2011). Deformation of an elliptical inclusion in two-dimensional incompressible power-law viscous flow. *Journal of Structural Geology*, 33(9), 1378-1393.
- Means, W. D. (1981). The concept of steady-state foliation. *Tectonophysics*, 78(1-4), 179-199.

- Michibayashi, K., & Murakami, M. (2007). Development of a shear band cleavage as a result of strain partitioning. *Journal of structural geology*, 29(6), 1070-1082.
- Okamoto, A., & Michibayashi, K. (2005). Progressive shape evolution of a mineral inclusion under differential stress at high temperature: Example of garnet inclusions within a granulite-facies quartzite from the Lützow-Holm Complex, East Antarctica. *Journal of Geophysical Research: Solid Earth*, 110(B11).
- Okudaira, T., Hayasaka, Y., Himeno, O., Watanabe, K., Sakurai, Y., & Ohtomo, Y. (2001). Cooling and inferred exhumation history of the Ryoke metamorphic belt in the Yanai district, south-west Japan: Constraints from Rb–Sr and fission-track ages of gneissose granitoid and numerical modeling. *Island Arc*, 10(2), 98-115.
- Passchier, C. W., & Trouw, R. A. (2005). *Microtectonics*. Springer Science & Business Media.
- Paterson, M. S., & Olgaard, D. L. (2000). Rock deformation tests to large shear strains in torsion. *Journal of structural Geology*, 22(9), 1341-1358.
- Poirier, J. P. (1985). *Creep of crystals: high-temperature deformation processes in metals, ceramics and minerals*. Cambridge University Press.
- Ramsay, J. G. (1980). Shear zone geometry: a review. *Journal of structural geology*, 2(1-2), 83-99.
- Ramsay, J. G., & Huber, M. I. (1983). *The Techniques of Modern Structural Geology: Strain Analyses* (Vol. 1). Course Technology.
- Ree, J. H. (1991). An experimental steady-state foliation. *Journal of Structural Geology*, 13(9), 1001-1011.
- Rybacki, E., & Dresen, G. (2004). Deformation mechanism maps for feldspar rocks. *Tectonophysics*, 382(3-4), 173-187.
- Schmid, S. M., & Casey, M. (1986). Complete fabric analysis of some commonly observed quartz c-axis patterns. *Geophysical Monograph*, 36(6), 263-286.
- Shewmon, P. G. (1963). Diffusion in solids. *McGrawAHill Book Company*. New York, NY.
- Stipp, M., & Tullis, J. (2003). The recrystallized grain size piezometer for quartz. *Geophysical Research Letters*, 30(21).

- Stipp, M., Stübenitz, H., Heilbronner, R., & Schmid, S. M. (2002). The eastern Tonale fault zone: a 'natural laboratory' for crystal plastic deformation of quartz over a temperature range from 250 to 700 C. *Journal of structural geology*, 24(12), 1861-1884.
- Sugimura, A., & Uyeda, S. (1973). Island Arc, Japan, and Its Environments.
- Toriumi, M. (1981). Rounded mineral inclusions in upper mantle peridotite. *Physics of the Earth and Planetary Interiors*, 27(1), 39-46.
- Toriumi, M. (1987). Progressive deformation and annealing of quartz inclusion in porphyroblastic feldspar during synmetamorphic non-coaxial deformation. *The Journal of the Japanese Association of Mineralogists, Petrologists and Economic Geologists*, 82(4), 123-131.
- Wang, G. F., Banno, S., & Takeuchi, K. (1986). Reactions to define the biotite isograd in the Ryoke metamorphic belt, Kii Peninsula, Japan. *Contributions to Mineralogy and Petrology*, 93(1), 9-17.
- Wightman, R. H., Prior, D. J., & Little, T. A. (2006). Quartz veins deformed by diffusion creep-accommodated grain boundary sliding during a transient, high strain-rate event in the Southern Alps, New Zealand. *Journal of Structural Geology*, 28(5), 902-918.

Part 2

- Allaby, M. (Ed.). (2013). A dictionary of geology and earth sciences. Oxford University Press.
- Ando, K., & Oishi, Y. (1983). Effect of Ratio of Surface Area to Volume on Oxygen Self-Diffusion Coefficients Determined for Crushed MgO-Al₂O₃ Spinels. *Journal of the American Ceramic Society*, 66(8), C-131.
- Chakraborty, S., & Ganguly, J. (1991). Compositional zoning and cation diffusion in garnets. In Diffusion, atomic ordering, and mass transport (pp. 120-175). Springer, New York, NY.
- Cheng, Y. (1995). Mean shift, mode seeking, and clustering. *IEEE transactions on pattern analysis and machine intelligence*, 17(8), 790-799.
- Cho, J. H., & Kurup, P. U. (2011). Decision tree approach for classification and dimensionality reduction of electronic nose data. *Sensors and Actuators B: Chemical*, 160(1), 542-548.
- Hickmott, D. D., Shimizu, N., Spear, F. S., & Selverstone, J. (1987). Trace-element zoning in a

- metamorphic garnet. *Geology*, 15(6), 573-576.
- Hickmott, D. D., & Shimizu, N. (1990). Trace element zoning in garnet from the Kwoiek Area, British Columbia: disequilibrium partitioning during garnet growth?. *Contributions to Mineralogy and Petrology*, 104(6), 619-630.
- Hollister, L. S. (1970). Origin, mechanism, and consequences of compositional sector-zoning in staurolite. *American Mineralogist: Journal of Earth and Planetary Materials*, 55(5-6), 742-766.
- Hoskin, P. W., & Schaltegger, U. (2003). The composition of zircon and igneous and metamorphic petrogenesis. *Reviews in mineralogy and geochemistry*, 53(1), 27-62.
- Hsu, C. W., Chang, C. C., & Lin, C. J. (2003). A practical guide to support vector classification.
- Hu, H. Y., Lee, Y. C., Yen, T. M., & Tsai, C. H. (2009). Using BPNN and DEMATEL to modify importance–performance analysis model—A study of the computer industry. *Expert systems with applications*, 36(6), 9969-9979.
- Joesten, R. (1991). Grain-boundary diffusion kinetics in silicate and oxide minerals. In *Diffusion, atomic ordering, and mass transport* (pp. 345-395). Springer, New York, NY.
- Loomis, T. P. (1976). Irreversible reactions in high-grade metapelitic rocks. *Journal of Petrology*, 17(4), 559-588.
- Loomis, T. P. (1983). Compositional zoning of crystals: a record of growth and reaction history. In *Kinetics and equilibrium in mineral reactions* (pp. 1-60). Springer, New York, NY.
- Malaviarachchi, S. P., Makishima, A., & Nakamura, E. (2010). Melt–peridotite reactions and fluid metasomatism in the upper mantle, revealed from the geochemistry of peridotite and gabbro from the Horoman peridotite massif, Japan. *Journal of Petrology*, 51(7), 1417-1445.
- Malaviarachchi, S. P., Makishima, A., Tanimoto, M., Kuritani, T., & Nakamura, E. (2008). Highly unradiogenic lead isotope ratios from the Horoman peridotite in Japan. *Nature Geoscience*, 1(12), 859-863.
- Myles, A. J., Feudale, R. N., Liu, Y., Woody, N. A., & Brown, S. D. (2004). An introduction to decision tree modeling. *Journal of Chemometrics: A Journal of the Chemometrics Society*, 18(6), 275-285.
- Nakakoji, T., & Hiraga, T. (2018). Diffusion creep and grain growth in forsterite+ 20 vol% enstatite

- aggregates: 2. Their common diffusional mechanism and its consequence for weak-temperature-dependent viscosity. *Journal of Geophysical Research: Solid Earth*, 123(11), 9513-9527.
- Nakamura, Y. (1973). Origin of sector-zoning of igneous clinopyroxenes. *American Mineralogist: Journal of Earth and Planetary Materials*, 58(11-12), 986-990.
- Niida, K. I. Y. O. A. K. I. (1974). Structure of the Horoman ultramafic massif of the Hidaka metamorphic belt in Hokkaido, Japan. *J. Geol. Soc. Japan*, 80, 31-44.
- Okamoto, A., & Michibayashi, K. (2005). Progressive shape evolution of a mineral inclusion under differential stress at high temperature: Example of garnet inclusions within a granulite-facies quartzite from the Lützow-Holm Complex, East Antarctica. *Journal of Geophysical Research: Solid Earth*, 110(B11).
- Ozawa, K. (1989). Stress-induced Al–Cr zoning of spinel in deformed peridotites. *Nature*, 338(6211), 141-144.
- Ozawa, K., & Takahashi, N. (1995). PT history of a mantle diapir: the Horoman peridotite complex, Hokkaido, northern Japan. *Contributions to Mineralogy and Petrology*, 120(3), 223-248.
- Ozawa, K. (2004). Thermal history of the Horoman peridotite complex: a record of thermal perturbation in the lithospheric mantle. *Journal of Petrology*, 45(2), 253-273.
- Park, S., & Kim, J. (2019). Landslide susceptibility mapping based on random forest and boosted regression tree models, and a comparison of their performance. *Applied Sciences*, 9(5), 942.
- Shibutani, T., Kitamura, T., & Ohtani, R. (1998). Creep cavity growth under interaction between lattice diffusion and grain-boundary diffusion. *Metallurgical and Materials Transactions A*, 29(10), 2533-2542.
- Sung, A. H., & Mukkamala, S. (2003). Identifying important features for intrusion detection using support vector machines and neural networks. In *2003 Symposium on Applications and the Internet, 2003. Proceedings.* (pp. 209-216). IEEE.
- Suzuki, A. M., Yasuda, A., & Ozawa, K. (2008). Cr and Al diffusion in chromite spinel: experimental determination and its implication for diffusion creep. *Physics and Chemistry of Minerals*, 35(8), 433-445.

- Swaroop, S., Kilo, M., Argirusis, C., Borchardt, G., & Chokshi, A. H. (2005). Lattice and grain boundary diffusion of cations in 3YTZ analyzed using SIMS. *Acta materialia*, 53(19), 4975-4985.
- Sawaguchi, T. (2004). Deformation history and exhumation process of the Horoman Peridotite Complex, Hokkaido, Japan. *Tectonophysics*, 379(1-4), 109-126.
- Takazawa, E., Frey, F. A., Shimizu, N., Saal, A., & Obata, M. (1999). Polybaric petrogenesis of mafic layers in the Horoman peridotite complex, Japan. *Journal of Petrology*, 40(12), 1827-1851.
- Toriumi, M. (1987). Progressive deformation and annealing of quartz inclusion in porphyroblastic feldspar during synmetamorphic non-coaxial deformation. *The Journal of the Japanese Association of Mineralogists, Petrologists and Economic Geologists*, 82(4), 123-131.
- Tracy, R. J., & McLellan, E. L. (1985). A natural example of the kinetic controls of compositional and textural equilibration. In *Metamorphic reactions* (pp. 118-137). Springer, New York, NY.
- Tuzel, O., Porikli, F., & Meer, P. (2009). Kernel methods for weakly supervised mean shift clustering. In *2009 IEEE 12th International Conference on Computer Vision* (pp. 48-55). IEEE.
- Uhmb, T. H., & Michibayashi, K. (2022). A shape-change model for isolated K-feldspar inclusions within a shear zone developed in the Teshima granite, Ryoke metamorphic belt, Japan: Estimation of the duration of deformation in a natural shear zone. *Tectonophysics*, 229229.
- Vance, J. A. (1965). Zoning in igneous plagioclase: patchy zoning. *The Journal of Geology*, 73(4), 636-651.
- Yang, J., Rahardja, S., & Fränti, P. (2019). Outlier detection: how to threshold outlier scores?. In *Proceedings of the international conference on artificial intelligence, information processing and cloud computing* (pp. 1-6).
- Yoshikawa, M., Niida, K., & Green, D. H. (2019). Dunite channels within a harzburgite layer from the Horoman peridotite complex, Japan: Possible pathway for magmas. *Island Arc*, 28(1), e12279.
- Zhang, P., Du, K., Tannant, D. D., Zhu, H., & Zheng, W. (2018). Automated method for extracting and analysing the rock discontinuities from point clouds based on digital surface model of rock mass. *Engineering Geology*, 239, 109-118.